TECHNISCHE UNIVERSITÄT MÜNCHEN

FAKULTÄT FÜR ELEKTROTECHNIK UND INFORMATIONSTECHNIK

Electronic-Ionic Transport in Organic-Inorganic Hybrid Perovskite Solar Cells: A Combined Theoretical and Experimental Study

Ajay Singh

Vollständiger Abdruck der von der Fakultät für Elektrotechnik und Informationstechnik der Technischen Universität München zur Erlangung des akademischen Grades eines

Doktors der Ingenieurwissenschaften (Dr.-Ing.)

genehmigten Dissertation.

Vorsitzender: Prof. Dr. Marc Tornow

Prüfende der Dissertation:

1. Prof. Dr. Alessio Gagliardi
2. Assoc. Prof. Dr. Alex Redinger

Die Dissertation wurde am 10.02.2021 bei der Technischen Universität München eingereicht und durch die Fakultät für Elektrotechnik und Informationstechnik am 31.08.2021 angenommen.

Dedicated to

my Guru Prof. G.V. Prakash

and

Abstract

Organic-inorganic hybrid perovskite (OIHP) semiconductors offer a wide range of bandgaps, low-cost deposition, high optical absorption, long charge carrier diffusion, and high power conversion efficiency, making them an ideal candidate for a solar cell. The efficiency of OIHP based solar cells has increased from 3.8% in 2009 to 25.2% in 2020, making them the fastest-advancing and most promising solar cell technology. Furthermore, solar spectrum absorption-selectivity and bandgap tunability make OIHPs a potential candidate for building-integrated photovoltaics and tandem cell applications.

Although the perovskite solar cell technology is rapidly developing, several issues even at the device level remain unknown and hamper this technology's improvements. There are several issues of great relevance that need to be addressed by theoretical analysis and simulations in collaboration with experimental studies. In particular, charge transport in OIHPs is a complex phenomenon and still not very well understood. The OIHP films consist of grain boundaries and ionic defects. The perovskite solar cells show hysteresis in the JV characteristics. The JV hysteresis is reported to be related to both the ionic defects and the grain boundaries. However, the charge dynamics leading to the JV hysteresis is still under debate. Furthermore, to fully utilize the potential of OIHPs, it is needed to develop tandem cell technologies that can surpass the efficiency limit of a single junction cell while offering low-cost electricity generation.

This thesis investigates the charge transport in single junction and tandem IOHP solar cells by analyzing various factors affecting the cell performance. A one-dimensional steady-state drift-diffusion (DD) model for a perovskite solar cell is proposed in chapter 2. The model investigates the role of interface traps, charge carrier mobility, transport layer doping, contact workfunctions, and the perovskite interface functionalization. The 3rd chapter focuses on the role of grain boundaries and ionic defect accumulation using a two-dimensional DD model. To study the role of ionic-mediated recombination in the JV hysteresis, a time-dependent DD model is presented in chapter 4. Chapter 5 investigates the potential of high-efficiency fully-perovskite tandem solar cells. Efficiency optimization of a 2-terminal tandem device is done by tuning bandgaps, thickness, and contact workfunctions of the subcells. Finally, chapter 6 is devoted to the fabrication and characterization of semitransparent perovskite solar cells. The charge carrier recombination process is studied by using time-resolved photoluminescence and scanning-electron microscope techniques. Methylamine treatment of $MAPbBr_3$ films is proposed to suppress recombination and to improve the transparency and efficiency of the $MAPbBr_3$ perovskite cells.

The proposed steady-state drift-diffusion simulations give better insight into the charge transport and various loss mechanisms in perovskite solar cells. The time-dependent DD model provides a different perspective on the role of ionic-mediated recombination in the JV hysteresis in perovskite solar cells. The modeling of 2T tandem solar cells helps to understand the role of different material and device parameters such as bandgap, thickness, doping, and mobility. The model also explains the factors limiting tandem

cell efficiency (i.e., interface and bulk traps) and the ways to improve the efficiency (i.e., doping of transport layers and optimizing contact workfunctions). Ultimately, DD models provide experimentalists the optimum designs of single-junction and all-perovskite tandem solar cells. Methylamine treatment will open a new approach for fabricating high efficiency semitransparent solar cells obtained at low-temperature processing. The treatment works well for the device fabrication in ambient conditions; therefore, this is a good move towards commercializing these devices. Ultimately, the research will help to develop low-cost and highly efficient single-junction and tandem perovskite solar cells.

Kurzfassung

Organisch-anorganische Hybrid-Perowskit (OIHP) -Halbleiter bieten eine große Bandbreite an Bandlücken, kostengünstige Herstellung und hohe optische Absorption, lange Ladungsträgerdiffusion und hohe Energieumwandlungseffizienz, was sie zu einem idealen Kandidaten füür eine Solarzelle macht. Der Wirkungsgrad von Solarzellen auf OIHP-Basis stieg von 3,8% im Jahr 2009 auf 25,2% im Jahr 2020 und ist damit die am schnellsten voranschreitende und vielversprechendste Solarzellentechnologie. Darüber hinaus machen die Absorptionsselektivität des Sonnenspektrums und die Abstimmbarkeit der Bandlücke OIHPs zu einem potenziellen Kandidaten für gebäudeintegrierte Photovoltaik- und Tandemzellenanwendungen.

Obwohl sich die Perowskit-Solarzellentechnologie schnell entwickelt, sind einige Probleme Geräteebene unbekannt und behindern die Verbesserung dieser Technologie. Es gibt mehrere Fragen von großer Relevanz, die durch theoretische Analysen und Simulationen in Zusammenarbeit mit experimentellen Studien geklärt werden müssen. Insbesondere der Ladungstransport in OIHPs ist ein komplexes Phänomen und noch nicht sehr gut verstanden. In OIHP-Filmen gibt es viele Korngrenzen und Ionendefekte. Die Perowskit-Solarzellen zeigen eine Hysterese in der JV-Kennlinie. Es wird berichtet, Die JV-Hysterese sowohl mit den Ionendefekten als auch mit den Korngrenzen zusammenhängt. Die Dynamik der Ladungsträger, die zur JV-Hysterese führt, wird jedoch noch diskutiert. Um das Potenzial von OIHPs voll auszuschöpfen, müssen Tandemzellentechnologien entwickelt werden, die Effizienzgrenze einer einzelnen Sperrschichtzelle überschreiten und gleichzeitig eine kostengünstige Stromerzeugung ermöglichen.

Diese Arbeit untersucht den Ladungstransport in Einzel- und Tandem-IOHP-Solarzellen, indem verschiedenen Faktoren untersucht werden, die Leistung der Solarzelle beeinflussen. Ein eindimensionales stationüres Drift-Diffusionsmodell (DD-Modell) für eine Perowskit-Solarzelle wird in Kapitel 2 vorgeschlagen. Das Modell untersucht die Rolle von Grenzflächenfallen, Ladungsträgermobilität, Transportschichtdotierung, Kontaktarbeitsfunktion und Perowskit-Grenzflächenfunktionalisierung. Das dritte Kapitel befasst sich mit der Rolle der Korngrenzen und der Akkumulation von Ionendefekten unter Verwendung eines zweidimensionalen DD-Modells. Um die Rolle der Ionen-vermittelten Rekombination bei der JV-Hysterese zu untersuchen, wird in Kapitel 4 ein zeitabhängiges DD-Modell vorgestellt. Kapitel 5 untersucht das Potenzial hocheffizienter Tandemsolarzellen die vollständig aus Perowskit bestehen. Die Effizienzoptimierung einer Tandemsolarzelle mit zwei Anschlüssen erfolgt durch Einstellen der Bandlücken, der Dicke und der Kontaktarbeitsfunktionen der beiden Unterzellen. Schließlich ist Kapitel 6 der Herstellung und Charakterisierung von semitransparenten Perowskit-Solarzellen gewidmet. Der Ladungsträgerrekombinationsprozess wird unter Verwendung zeitaufgelöster Photolumineszenz- und Oberflächen-Elektronenmikroskopie untersucht. Die Methylamin-Behandlung von $MAPbBr_3$ -Filmen wird vorgeschlagen, um die Rekombination zu unterdrücken und die Transparenz und Effizienz der $MAPbBr_3$ –Perowskit-Solarzellen zu verbessern.

Kurzfassung

Die vorgeschlagenen stationären Drift-Diffusions-Simulationen bieten einen besseren Einblick in den Ladungstransport und verschiedene Verlustmechanismen in Perowskit-Solarzellen. Das zeitabhängige DD-Modell bietet eine andere Perspektive auf die Rolle der Ionen-vermittelten Rekombination bei der JV-Hysterese in Perowskit-Solarzellen. Die Modellierung von 2T-Tandemsolarzellen hilft dabei, die Rolle verschiedener Material- und Bauelementparameter wie Bandlücke, Dicke, Dotierung und Mobilität zu verstehen. Das Modell erklärt auch die Faktoren, die Effizienz von Tandemzellen begrenzen (z.B. Grenzflächen- und Massen-Fallen) und die Möglichkeiten zur Verbesserung der Effizienz (z.B. Dotierung der Transportschichten und Optimierung der Kontaktarbeitsfunktionen). Letztendlich bieten DD-Modelle Experimentatoren das optimale Design von Einzel- und Tandem-Solarzellen. Die Methylamin-Behandlung eröffnet einen neuen Ansatz für die Herstellung hocheffizienter semitransparenter Solarzellen, die bei niedrigen Temperaturen hergestellt werden. Die Behandlung eignet sich gut für die Herstellung von Bauelementen unter Umgebungsbedingungen. Daher ist dies ein guter Schritt in Richtung Kommerzialisierung dieser Bauelemente. Letztendlich wird die Forschung dazu beitragen, kostengünstige und hocheffiziente Einzel- und Tandem-Perowskit-Solarzellen zu entwickeln.

List of Own Publications and Contributions

Peer-reviewed journals

A. Singh, W. Kaiser, and A. Gagliardi. Role of cation-mediated recombination in perovskite solar cells. *Sol. Energy Mater Sol.*, 221:110912, 2021.

A. Singh and A. Gagliardi. Efficiency of all-perovskite two-terminal tandem solar cells: A drift-diffusion study. *Sol. Energy*, 187:39–46, 2019.

A. Singh, F. Matteocci, H. Zhu, D. Rossi, S. Mejaouri, S. Cacovich, M. A. D. Maur, F. Sauvage, A. Gagliardi, M. Grätzel and A. D. Carlo. Methylamine gas treatment affords improving semitransparency, efficiency, and stability of $CH_3NH_3PbBr_3$-based perovskite solar cells. *Sol. RRL*, 5(9): 21002776, 2021.

L. Canil, T. Cramer, B. Fraboni, D. Ricciarelli, D. Meggiolaro, A. Singh, M. Liu, M. Rusu, C. M. Wolff, N. Phung, Q. Wang, D. Neher, T. Unold, P. Vivo, A. Gagliardi, F. De Angelis, and A. Abate. Tuning halide perovskite energy levels. *Energy Environ. Sci.*, 14: 1429-1438, 2021.

A. Singh and A. Gagliardi. Device simulation of all-perovskite four-terminal tandem solar cells: Towards 33% efficiency. *EPJ Photovolt.*, 12:4, 2021.

A. Singh, E. Radicchi, S. Fantacci, F. Nunzi, F. De Angelis and A. Gagliardi, "Interface electrostatics of solid-state dye-sensitized solar cells: A joint drift-diffusion and density functional theory study" *J. Phys. Chem. C*, 123(24):14955–14963, 2019.

Conference proceedings

A. Singh and A. Gagliardi. Role of ion-assisted recombination and grain boundaries in perovskite solar cell hysteresis and efficiency. In *IEEE 20th International Conference on Nanotechnology (IEEE-NANO: Virtual)*, pages 227–232. IEEE, 2020.

Conference presentations

A. Singh, and A. Gagliardi. Role of ionic-assisted recombination and grain boundaries in perovskite solar cell hysteresis and efficiency. In *IEEE 20th International Conference on Nanotechnology (IEEE-NANO: Virtual)*, Oral presentation, Montreal, Canada, Jul. 2020.

A. Singh, and A. Gagliardi. Drift-diffusion and machine learning for high efficiency perovskite-perovskite based tandem solar cells. In *International Conference on Hybrid and Organic Photovoltaics (HOPV)*, Poster Presentation, Rome, Italy, May 2019.

A. Singh, Eros Radicchi, Simona Fantacci, Filippo De Angelis, and A. Gagliardi. Investigation of interface electrostatics of solid-state dye sensitized solar cells. In *The Second Dyenamo DSSC Conference*, Oral Presentation, Uppsala, Sweden, Oct. 2019.

A. Gagliardi, A Singh, W Kaiser. Simulation of ion migration in perovskite solar cells using a kinetic Monte Carlo/drift diffusion numerical model and analysis of the impact on device performance. In *International Conference on Hybrid and Organic Photovoltaics (HOPV)*, Oral Presentation, Benidorm, Spain , May 2018.

Contents

List of Figures

List of Tables

1 Introduction

1.1 Motivation

The increasing demand for energy resources by human society and the depletion of conventional energy sources have made researchers think of alternative energy resources. The world energy consumption in the year 2019 was about 583.9×10^{18} J [1] which is expected to grow in the coming years. Currently, fossil fuels share more than 80% of total energy consumption globally. Widely used fossil fuels pollute the environment and will be exhausted soon. In 2019, about 34169.0 million tonnes of carbon dioxide (CO_2) was emitted [1]. To reduce the CO_2 footprint and the dependency on fossil fuels, it has become a need of the hour to look for renewable and green energy alternatives.

Solar energy is one of the vast sources of renewable energy that is freely available. The earth's surface receives approximately 340×10^{22} J of energy per year from the sun [2], thousand times higher than the energy demand by the human society. The solar energy can be utilized mainly in three ways: photovoltaics, solar heating & cooling, and concentrating solar power. Photovoltaics, also known as solar cell, is one of the most promising solar energy technology to convert solar energy into electricity that can be used for various applications. In the last few decades, solar cell research and development have accelerated due to the aforementioned needs [3].

Solar cells work on the principle of photovoltaic effect [4], which is a physical and chemical phenomenon. A semiconductor absorber leads to electron and hole generation upon sunlight exposure. Those charge carriers are collected in an external circuit in terms of electricity. Based on the timeline, the materials used and the fabrication process, solar cells are generally classified into three generations. The first-generation cells, also known as the conventional solar cells, are monocrystalline or polycrystalline silicon wafer-based cells. Currently, the market is dominated by silicon solar cells. Since a thick absorber is needed for conventional cells, second-generation solar cells were introduced based on a few nanometers to tens of micrometers of thin films absorbers. These include amorphous silicon, cadmium telluride (CdTe) and copper indium gallium selenide (CIGS) based solar cell cells. Solar cells based on GaAs, silicon, CIGS and cadmium telluride (CdTe), have achieved power conversion efficiencies up to 29% and 30% without and with concentrator, respectively [5]. However, both of the first and second-generation solar cells need a controlled environment and a high thermal budget in their fabrication processes. Furthermore, apart from silicon, most of these materials are expensive. Silicon offers high charge carrier mobility, rigidity, and good stability against environmental conditions. But, silicon-based solar cells are heavyweight, and the fabrication is not cost-effective. Several attempts have been made to push the silicon cell efficiency; such as texturing, polishing, doping, defect passivation, using nanostructures and quantum confinements, adopting a multijunction approach, and implementing multiple reflection mechanisms [6, 7, 8, 9]. But, it has been challenging to achieve affordable price for the per-unit kWh electricity generation from the silicon photovoltaics. Therefore, for a cost-effective photovoltaic

technology, it is needed to adopt low-temperature and solution-processable materials and fabrication techniques.

The cost-effectiveness could be achieved either by increasing the efficiency (i.e., multijunction cells, nanostructuring, quantum dots), or by reducing the fabrication cost. These technologies have been adopted in the third-generation of solar cells. Reducing the fabrication cost by using solution processability has gained significant attention in recent years. Dye-sensitized solar cells (DSSCs), polymer and organic solar cells can be made cheaper because they can be processed at low temperature and do not need an extensively controlled environment. Moreover, they can offer flexibility and transparency [10, 11]. However, organic solar cell efficiency is limited by the highly disordered nature of organic materials and low light-absorption [12, 13]. DSSCs' efficiency is limited by the limited number of available dye-sensitizers and their low light-absorption. Furthermore, conventional DSSCs suffer device instability because of the liquid nature of electrolyte used for the dye-regeneration.

A material that can combine the merits of both the organic materials (i.e., solution processability, flexibility) and inorganic materials (high absorption, high optical to electrical power conversion, high charge carrier mobility, and stability) is an obvious choice to obtain high-efficiency and low-cost solar cells.

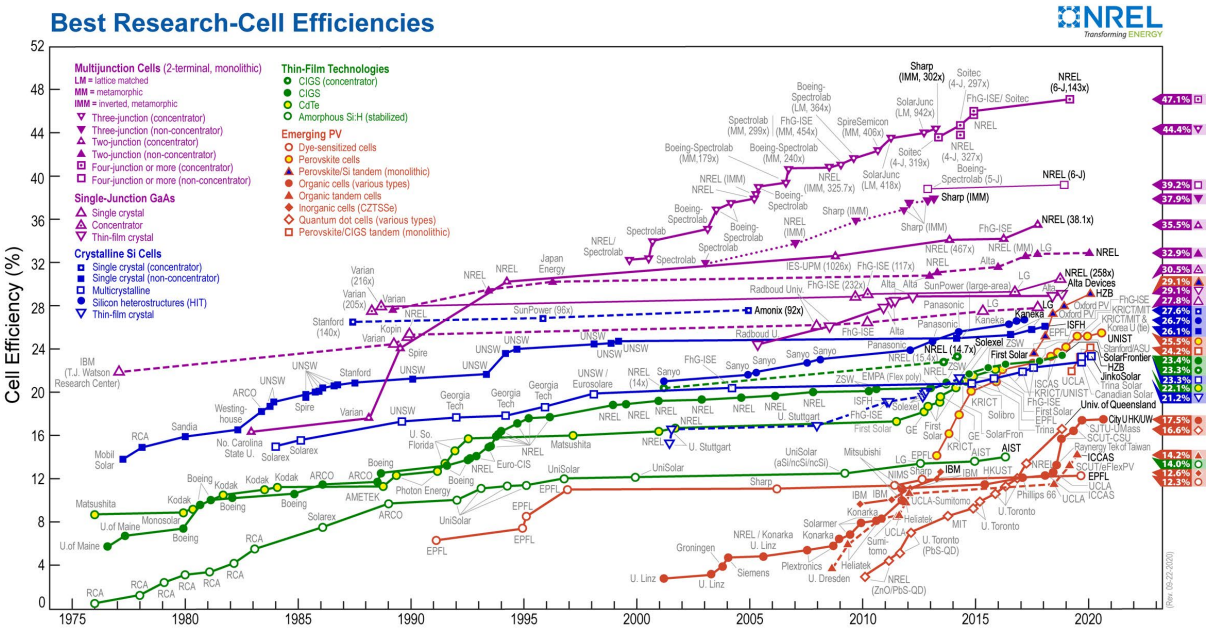

Figure 1.1: The best solar cell efficiency chart, NREL [5].

Organic-inorganic hybrid perovskite (OIHP) materials have emerged as potential photovoltaic materials because of their broad optical absorption, high power conversion, high carrier mobility, defect-tolerance, and longer diffusion lengths [14, 15]. Moreover, the availability of a wide range of OIHPs, and cost-effective fabrication processes makes them a potential alternative over the conventional solar cell technologies [16, 17, 18, 19]. Perovskite solar cell efficiencies have exceeded 25% [5], making this one of the fastest-growing solar cell technology (see Figure 1.1). With the potential to achieve higher efficiencies at low production-costs, perovskite solar cells (PSCs) have become commercially attractive, and many companies are promising modules on the market soon [20].

1.2 Organic-inorganic hybrid perovskites

Organic-inorganic hybrid perovskites (OIHPs) are materials with crystal structure similar to the mineral called perovskite, i.e., calcium titanium oxide ($CaTiO_3$). Based on their general chemical formula, these are also known as ABX_3 type of crystals, where 'A' and 'B' are two cations, and 'X' is an anion that bonds to both the cations. In OIHPs, 'A' is an organic cation such as $CH_3NH_3^+$ (methylammonium) or $HC(NH_2)_2^+$ (formamidinium). 'B' is an inorganic cation, usually lead (Pb^{2+}) or tin (Sn^{2+}). And, 'X' is halogen anion, such as I^-, Cl^-, Br^-, or a combination of these. In a three-dimensional cubic crystal structure, cation 'A' resides in the face-centered cubic lattice's vertex. The halogen anion resides at the apex of octahedra. The metal cation B (usually smaller in size than A) occupies the octahedral void, as shown in Figure 1.2a. The formation of an ABX_3 perovskite structure is limited by the Goldschmidt tolerance factor [21]:

$$t = \frac{r_A + r_X}{\sqrt{2}\,(r_B + r_X)} \tag{1.1}$$

where r_A, r_B and r_X are the ionic radii of 'A', 'B' and 'X' ions, respectively. In general, $0.8 < t \leq 0.9$ corresponds to tetragonal or orthorhombic perovskites, and $0.9 < t \leq 1$ corresponds to a cubic perovskite structure [22]. A tolerance factor of too low (< 0.85) or two high (> 1.11) can never form a perovskite structure [21, 22]. Furthermore, the ratio of the ionic radii of 'B' and 'X' ions should satisfy octahedral factor, defined as:

$$\mu = \frac{r_A}{r_X} \tag{1.2}$$

where, $0.44 < \mu < 0.9$ [22, 21]. Thankfully, several combinations of organic 'A', inorganic 'B' and halide 'X' qualify the criteria of tolerance factor and octahedral factor to form ABX_3 type OIHP structure. Figure 1.2b shows the crystal structure of formamidinium lead iodide $HC(NH_2)_2PbI_3$ ($FAPbI_3$) perovskite at 300 K. $FAPbI_3$ has a cubic phase at 300 K. Six iodine atoms surround a lead atom to form an octahedra. Eight of such units make a lattice. The formamidinium cation resides in the void of this lattice structure. Repetition of this whole unit leads to a three-dimensional $FAPbI_3$ crystal.

With a change in temperature, a perovskite can change its phase and/or crystal structure [23, 24]. Methylammonium lead iodide ($CH_3NH_3PbI_3$) perovskite is a well-studied OIHP that undergoes structural phase transitions from orthorhombic to tetragonal at 170 K and then to cubic phase at 330 K [24, 25]. In a $CH_3NH_3PbX_3$ crystal, the 'X' ions are not fixed and can migrate through the crystal. The $CH_3NH_3^+$ cations can rotate within their cages. This free movement of the ionic defects affects the device performance. The implication of ionic defects will be discussed in detail in chapters 3 and 4.

Most of the OIHPs have a direct bandgap, therefore they show a strong light absorption with a sharp edge and steep onset [27, 14, 28]. A high absorption coefficient of around $1 \times 10^5\,cm^{-1}$ indicates a very small number of optically detectable deep traps [29, 14]. This enables a thin layer (a few 100 nm) of perovskite to absorb a sufficient amount of sunlight. At the same time, OIHPs have a high dielectric constant, which results in low binding-energy of excitons generated upon light exposure.

Charge carrier diffusion lengths in OIHPs have been shown to be in the range of micrometers, which also indicates low trap density with shallow defect states [30, 14]. Longer diffusion length helps the photogenerated charge carrier to travel to the contacts

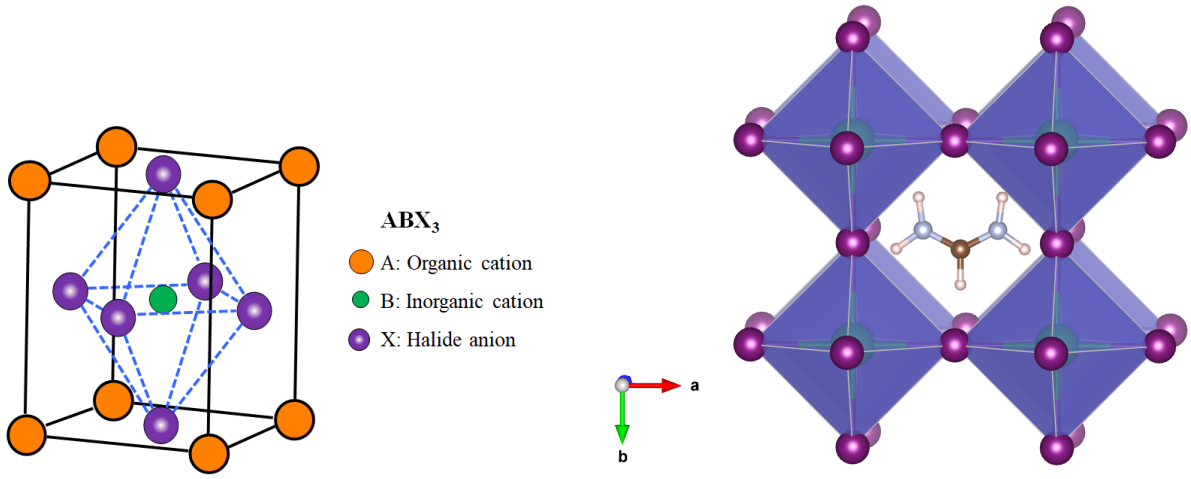

Figure 1.2: $FAPbI_3$ perovskite cubic phase structure at 300 K. Six iodine atoms (violet spheres) surround a lead atom (green spheres). Eight of such units make a net structure. Formamidinium cation resides in the void of this net. Repetition of this whole unit leads to a three-dimensional $FAPbI_3$ crystal. The structure is drawn with VESTA, following Weller *et al.* [26].

before they are recombined within the absorber. Moreover, ambipolar charge carrier transport and high mobility make OIHPs a suitable choice for photovoltaic applications.

The bandgap of a OIHP materials can be tuned by changing 'A' cation/ 'B' cation and/or 'X' anion [31, 32, 33, 34]. Figure 1.3a shows bandgaps and phases of various ABX_3 perovskites. Moreover, multiple cations and multiple anions compositions can be used to realize OIHP materials [32]. This makes the availability of a wide range of perovskites with the desired bandgap range. Figure 1.3b shows a change in the bandgap of methylamine lead iodide (bromide) perovskite with changing the bromine content. Increasing bromine content leads to an increase in the bandgap, and hence the perovskite film color changes. Wide bandgap materials offer semitransparency, which is needed for tandem cells and building-integrated photovoltaic applications. Chapter 6 investigates more on the semitransparent $MAPbBr_3$ perovskite solar cells. Now onward in this thesis, OIHP(s) will be referred to as perovskite(s).

1.3 Perovskite solar cell

For the first time, in 2009, Miyasaka *et al.* [35] reported the use of $CH_3NH_3PbI_3$ and $CH_3NH_3PbBr_3$ perovskite as sensitizer in dye-sensitized solar cells (DSC). The perovskite was deposited on a mesoporous TiO_2 layer, and a liquid electrolyte I^-/I_3^- was used to regenerate the perovskite sensitizer. In 2011, Im *et al.* [36] found that the efficiency can be pushed higher by simply increasing the perovskite loading. In 2012, Kim *et al.* [37] used perovskite nanoparticles as light harvester while replacing the liquid electrolyte with a solid-state hole-transporting material (HTM). They obtained a solid-state mesoscopic heterojunction solar cell with an efficiency exceeding 9%. This study was a breakthrough in the era of perovskite based solid-state solar cells. So far, the assumption was that the perovskite acts as a sensitizer, and therefore thick

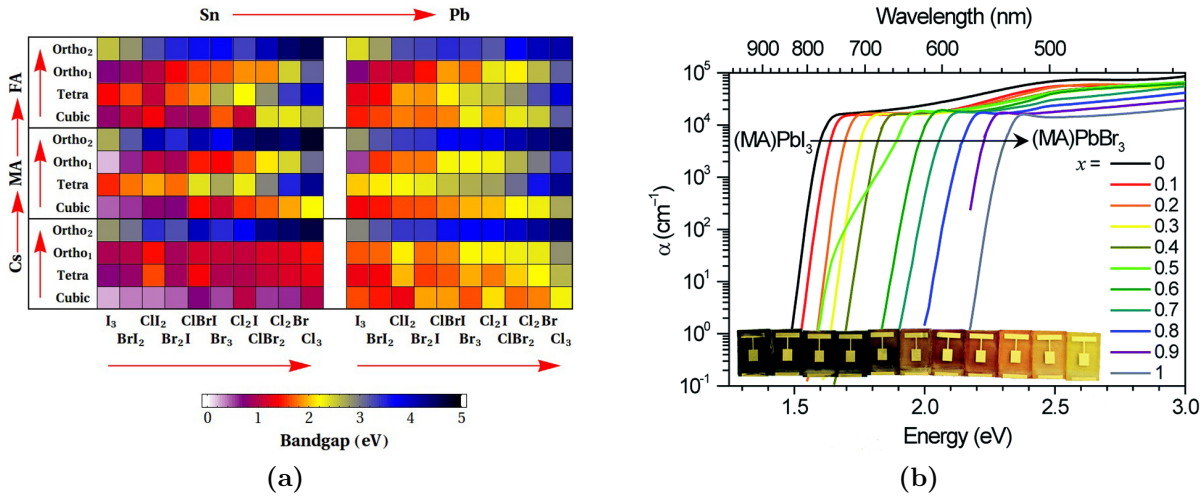

Figure 1.3: (a) Calculated bandgaps of ABX_3 perovskites by tuning A, B, and X sites. Figure reproduced by permission of ref. [32], © 2014 Castelli1 *et al.* and AIP Publishing; licensed under a Creative Commons Attribution (CC BY) license. (b) Bandgap tuning of methylammonium lead halide perovskite. The bandgap increases with increasing the bromine content replacing the iodide anion. Figure reproduced by permission of ref. [31], © The Royal Society of Chemistry 2015.

TiO_2 mesoporous layers (∼10 µm) were used. In another study, Lee *et al.* [38] observed that methylammonium lead halide perovskite-based solar cells can exhibit an open-circuit photovoltage of 1.1 V. Furthermore, they observed the semiconducting nature of the perovskite by employing a planar-junction diode with the structure FTO/-compact−TiO_2/$CH_3NH_3PbI_2Cl$/Spiro−OMeTAD/Ag. Thereafter, several configurations were studied to use perovskites both as an absorber and bipolar charge carrier transporter. Nowadays, a solid-state solar cell configuration in which a thick perovskite absorber is used as an absorber as well charge transporter, is commonly known as a "perovskite solar cell".

A typical perovskite solar cell consists of a glass substrate with transparent conductive contact, an electron transport layer (ETL), a perovskite layer, a hole transport layer (HTL), and a conductive contact. Based on the order in which different layers are arranged, the perovskite cell structure is categorized as standard or inverted, as shown in Figure 1.4. In a standard structure, transparent ETL is deposited on the conductive glass, followed by the perovskite layer, HTL, and the metal contact. In an inverted structure, first, the HTL is deposited on the conductive glass substrate, followed by perovskite, ETL, and the contact metal. The charge transport layer deposited on the transparent contact is chosen with a bandgap higher than that of the perovskite absorber. The light enters from the transparent contact and passes through ETL/HTL to the perovskite layer. The perovskite absorbs the light and generates electron-hole pairs. These electron-hole pairs (also known as exciton) have binding energy less than the thermal energy (25 meV), therefore quickly break down in electrons and holes [14]. The electrons (holes) start moving under the influence of a built-in electric field and are collected at the ETL (HTL).

The ETL material is chosen such that it has a conduction band lower than the perovskite conduction band level. The HTL has a valence band higher than that of the perovskite valence band. This energy alignment is required to collect electrons (hole)

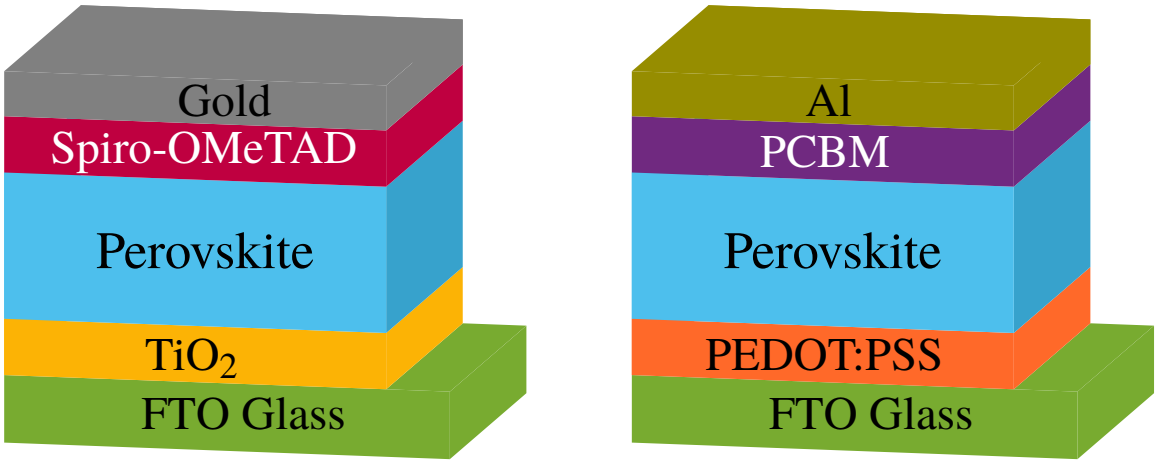

(a) **(b)**

Figure 1.4: Generic structures of standard (a), and inverted (b) planar perovskite solar cells.

at the ETL (HTL). Similarly, to extract the charges in the external circuit, the contact materials are chosen such that the electron (hole) collecting contact has an energy level below (up) the ETL (HTL) conduction (valence) level. Each layer's electrical and optical properties play an important role in charge transport, hence the perovskite solar cell's final performance.

The solar cell architectures shown in Figure 1.4 are also known as planar structures. A mesoporous charge transport layer can be adopted to increase the contact area between the charge transport layer and perovskite. Figure 1.5a shows a standard mesoporous perovskite solar cell architecture. Figure 1.5b represents an energy-level diagram of a typical perovskite solar cell. The increased contact area with the mesoporous TiO_2/perovskite leads to a better change injection from perovskite into TiO_2 layer [39, 40]. On the other hand, a large surface can present more surface traps at the TiO_2/perovskite interface.

1.4 Fabrication of perovskite solar cells

Both mesoporous and planar architectures have been reported in literature [41, 42]. To fabricate a perovskite solar cell, a transparent conducting oxide (TCO) deposited on glass is used as a substrate to grow a perovskite solar cell structure. Standard mesoporous cell typically consists of a mesoporous TiO_2 layer on top of a thin (20-30 nm) layer of compact TiO_2. The compact TiO_2 layer serves as the hole-blocking layer to reduce recombination at the anode due to perovskite being in contact with TCO. Spray pyrolysis, physical vapor deposition, spin-coating, or sputtering can be used to deposit a compact TiO_2 layer. However, spray pyrolysis is a commonly used method.

The mesoporous TiO_2 layer serves as an ETL. The TiO_2 scaffold also supports the formation of the perovskite layer. Furthermore, increased area between scaffold and perovskite improves electron injection from perovskite into ETL [39, 40]. Typically a spin-coated TiO_2 nanoparticles followed by sintering is used to obtain a TiO_2 scaffold of $\sim$ 200 nm. TiO_2 deposition is explained in detail in chapter 6. Apart from the TiO_2

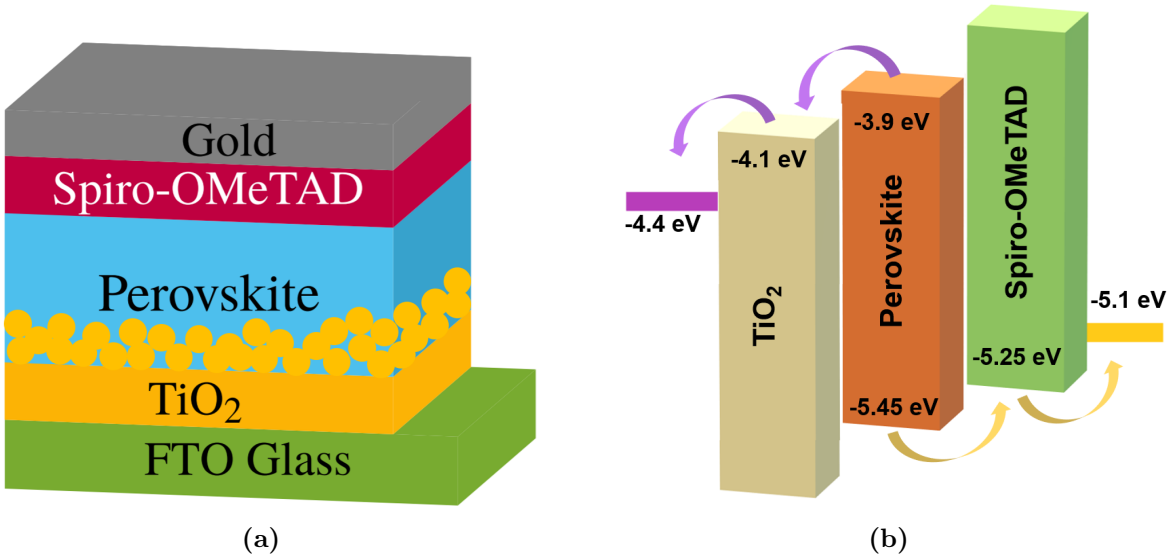

(a) (b)

Figure 1.5: (a) Standard mesoporous perovskite solar cell. (b) Typical energy band diagram of $CH_3NH_3PbI_3$ perovskite solar cell with TiO_2 and Spiro-OMeTAD as ETL and HTL, respectively.

nanoparticles, several other nanostructures such as, nanorods, nanowires, and nanofibers have been used in mesoporous PSCs [42, 43]. Other than TiO_2, materials such as ZnO, SnO_2, Al_2O_3, ZrO_2, and SiO_2 have been investigated to form a mesoporous scaffold [44, 45, 46]. Inverted (p-i-n) structures commonly employ NIO to obtain HTL scaffold [47]. Numerous other materials and deposition methods have been proposed to obtain a p-type mesoporous scaffold [47, 48].

Planar ETL and HTL layers can be deposited by using spin coating, chemical vapour deposition, spray pyrolysis, electro-deposition, sputtering, atomic layer deposition, pulsed laser deposition, and sol–gel processes and several other methods [43, 45, 48, 49, 50].

Perovskite absorber layers can be deposited by several single-step and sequential deposition techniques. In a single-step deposition, perovskite precursors are mixed in an organic solvent (typically dimethylformamide(DMF), dimethylsulphoxide (DMSO) and γ-butyrolactone(GBL)) and are deposited on the substrate. Commonly used single-step perovskite deposition methods include spin coating and chemical vapor deposition. Also, die coating, laser evaporation, dual-source evaporation, screen printing, and spray-assisted deposition have been reported to deposit perovskite films [42]. During the initial development of PSCs, Snaith *et al.* spin coated $PbCl_2$ and MAI precursors to get $MAPbI_{3-X}Cl_x$ perovskite film [38]. They reported a solar cell with an efficiency of 10.9%. After that, several techniques were proposed to utilize precursor, solvents, anti-solvents, and additives to obtain the single-step deposition of perovskite films [51]. Jeon *et al.* [52] used GBL and DMSO to mix perovskite precursors, followed by toluene drop-casting to obtain uniform and dense $CH_3NH_3PbI_3$ perovskite films via a CH_3NH_3I–PbI_2–DMSO intermediate phase. They fabricated PSCs with efficiency exceeding 16%. Miyadera *et al.* [53] reported a laser evaporation method, and obtained 16% efficient $CH_3NH_3PbI_3$ perovskite solar cells. Giuri *et al.* [54] used starch-DMSO assisted spin-coated $MAPbI_3$ films resulting in solar cell efficiency of 17.2%. Thermally stable vaccuum deposited 18.8% efficient $FA_{1-x}MA_xPbI_3$ PSCs were reported by Escrig *et al.* [55]. Wang *et al.* deposited $MAPbI_3$

films by a vacuum-assisted blade coating method, and obtained 19.41% efficient flexible PSCs [56].

Yi *et al.* [57] reported solvent vapor annealing (SVA) assisted fabrication of co-SVA $CH_3NH_3PbI_3$ devices with a power conversion efficiency (PCE) of 19.52%. Ahn *et al.* [58] used Lewis adduct of lead iodide to obtain $CH_3NH_3PbI_3$ PSCs with a maximum efficiency of 19.7%. Ross *et al.* [59] employed co-evaporation of MAI and PbI_2 to fabricate $MAPbI_3$ PSC. By combining vapor-deposited perovskites and a self-assembled monolayer, they achieve a record stabilized PCE of 20.6% for p-i-n configuration.

A single-step deposition gives a possibility to adopt die coating and role-to role processing; those are helpful towards commercialization [60]. However, the record efficiencies have been obtained by methods that include multiple steps in perovskite deposition [19]. Moreover, in many cases in single-deposition, anti-solvents are used to remove the used solvent. The choice of solvent and anti-solvent significantly affects the film morphology and hence the device performance.

In a sequential deposition (also known as two-step deposition), the lead halide precursor is first deposited on the substrate and is later converted into perovskite. For the irst time, Burschka *et al.* proposed $CH_3NH_3PbI_3$ deposition by a two-step deposition for PSCs [61]. They spin-coated PbI_2 on a TiO_2 scaffold, and then dipped into CH_3NH_3I solution. They obtained uniform coverage on the scaffold, resulting in $> 15\%$ efficient perovskite solar cells. Patel *et al.* presented a two-step thermal evaporation method to obtain $CH_3NH_3PbI_3$ perovskite [62]. This process takes several hours in full conversion of precursors into perovskite phase. Yuan *et al.* reported a solvent-assisted molecule inserting technique to grow perovskite film [63]. They achieved a solar cell efficiency and fill-factor exceeding 18% and 80%, respectively. Chen *et al.* [18] presented a scalable electrodeposition route to obtain $CH_3NH_3PbI_3$ films. They first deposited a PbO_2 layer on TiO_2 scaffold, followed by chemical bath to convert PbO_2 into PbI_2 and, subsequently into $CH_3NH_3PbI_3$ perovskite. Wang *et al.* synthesized [64] $(CH_3NH_3)_3Bi_2I_9$ films via a two-stage electric-field-assisted reactive deposition. This method could be adopted to deposit perovskite films for photovoltaic applications.

Sutter *et al.* [65] presented a low-pressure vapor-assisted solution process to obtain high quality $CH_3NH_3PbI_{3-x}Br_x$ perovskite films. Cui *et al.* used PbI_2, $PbBr_2$ and PbI_2/Br_2 mixtures dissolved in DMF to deposit lead halide films. These films were then brought in contact with heated methylamine powder. Upon intercalation, they obtained $MAPbBr_XI_{3-X}$ (X= 0, 1, 2, 3) perovskite films. Jiang *et al.* spin-coated FAI:MABr:MACl solution onto PbI_2 to obtain $FA_{1-x}MA_xPbI_3$ perovskite films [44]. The perovskite films were then passivated, and certified PCE of 23.32% was reported.

Numerous other methods have been proposed for sequential deposition of perovskite films [66]. Furthermore, methods have been reported to utilize solvent engineering, compositional engineering, morphology control and defect passivation to obtain high efficiency perovskite solar cells [67, 68, 69, 19, 70, 71]. Chapter 6 focuses more on defect passivation in perovskite films.

1.5 Photovoltaic performance of perovskite solar cells

Despite the intriguing properties of OIHPs and rapid advances in the perovskite solar cell fabrication technology, the reported power conversion efficiencies are far from the theo-

retical limit [72]. Several issues at the material and the device level remain unknown and hamper the cell performance. Solution-processed perovskite films consist of grain boundaries (GBs) and interface defects. Non-radiative recombinations at the grain boundaries have been reported to limit solar cell efficiency [73, 74, 75]. Further research is needed to understand the role of interfaces and GBs, and to develop ways to minimize them.

The movement of ionic-defects has also been reported in perovskite films [76, 77, 78]. Steady-state accumulation of ionic defects at the GBs and interfaces drastically affects the maximum power point of the cell, reducing the device reliability. Several recombination processes at the ionic defects are still unknown. This is well known that the perovskite solar cells exhibit hysteresis behavior in JV characteristics. Ionic defect migration has been postulated as the underlying mechanism responsible for the hysteresis [79, 78, 80]. Furthermore, studies have found that the combined effect of grain boundaries, interface recombination, and ionic migration results in the hysteresis nature [81, 82, 83, 84, 80]. However, the link between the ionic migration and the recombination mechanism is still unclear. Combined experimental and theoretical studies can draw a clearer picture of the origin and evolution of the JV hysteresis. Developing new methods for obtaining GBs-free perovskite films can help to develop highly efficient and hysteresis-free PSCs.

It has been speculated that the energy alignment between the charge transport layers and perovskite is a crucial parameter in determining the solar cell performance. Doping in charge transport layers and perovskite interface functionalization can improve the charge collection and the cell performance [85, 86, 87]. Theoretical studies and simulations can help optimize transport layer doping and perovskite interface functionalization to obtain maximum efficiency of a perovskite solar cell.

PSCs are potential candidate for tandem photovoltaic technologies [88, 89, 90]. To fully utilize the potential of a tandem cell technology, material and device parameters for each subcell and the tandem device must be optimized. Simulation studies can help optimize various material and device parameters and propose experimentalists the best design and material parameters to develop highly efficient tandem solar cells.

The stability of perovskite device is another concern that hampers the commercialization of this technology. The instability comes from the perovskite's intrinsic instabilities, device fabrication scheme, device architecture, and the choice of materials for various layers [91, 92, 93]. Furthermore, ionic defect migration has been speculated to affect the device performanc over time [94, 95, 96]. The origin of various photophysical instabilities and their relation to the defect-migration is not very well understood. Further research is needed to understand the instabilities and to develop stable-device fabrication. A brief discussion on the fabrication of stable devices is presented in chapter 6.

1.6 Drift-Diffusion model

Using Poisson's law, charges with a charge density, ρ lead to an electrostatic potential, governed by:

$$\nabla^2 \Phi = -\frac{\rho}{\epsilon_0} \tag{1.3}$$

For a material with dielectric constant ϵ, using the divergence operator, equation 1.3 can be rewritten as

$$\nabla \cdot (\epsilon \nabla \Phi) = -\rho \tag{1.4}$$

A bipolar semiconductor material can consist of electrons, holes, charge carrier traps, doping and other neutral and charged impurities. For such a semiconductor, the total charge density ρ can be represented in terms of electron density n, hole density p, acceptor doping density N_a^-, donor doping density N_d^+, electron trap density n_t^+, hole trap density n_t^-, positive charged impurity density n_c^+, and negative charged impurity density n_c^-. And, equation1.4 can be expressed as:

$$\nabla \cdot (\epsilon \nabla \Phi) = e\left(n - p - N_d^+ + N_a^- - n_t^+ + n_t^- - n_c^+ + n_c^-\right) \tag{1.5}$$

where, e is charge of an electron. A free moving charged particle under an electric field $\vec{E}$ can be characterized by the electric field induced velocity $\vec{\nu}$, and the current density $\vec{j}$, governed by:

$$\vec{j} = e\vec{\nu} \tag{1.6}$$

For an electron density n, equation 1.6 becomes:

$$\vec{j_n} = ne\vec{\nu_n} \tag{1.7}$$

The velocity vector $\vec{\nu}$ depends on the mobility of the electrons and the applied electric field $\vec{E}$, as

$$\vec{\nu_n} = \mu_n \vec{E}. \tag{1.8}$$

An electric field, $\vec{E}$ can be mathematically expressed as:

$$\vec{E} = -\nabla \phi \tag{1.9}$$

The electric field points from a high potential region to a low potential region. Rewriting equation 1.7 in terms of ϕ,

$$\vec{j_n} = -ne\mu_n \nabla \phi_n \tag{1.10}$$

By the divergence theorem, current density continuity equation can be written as:

$$\nabla . j_n = -\frac{\partial \rho_n}{\partial t} \tag{1.11}$$

Combining equations 1.10 and 1.11,

$$\nabla . \{e\mu_n n \left(\nabla \phi_n\right)\} = \frac{\partial \rho_n}{\partial t} \tag{1.12}$$

Similarly, for holes,

$$\nabla . \{e\mu_p p \left(\nabla \phi_p\right)\} = -\frac{\partial \rho_p}{\partial t} \tag{1.13}$$

Equations 1.12 and 1.13 are also known as continuity equations for electrons and holes, respectively. Because of the concentration gradient, particles start diffusing from a high concentration region to a low concentration region. Using the Einstein relation, a relation between charge carrier mobility and their diffusion coefficient, D is given by

$$D = \mu k_B T/q \tag{1.14}$$

where, k_B is the Boltzmann's constant, T is temperature, and q is the elementary charge. In a semiconductor material, the charge transport is governed by an electrically induced drift and a concentration gradient induced diffusion. Following the Einstein relation, combined equations 1.5, 1.12, and 1.13 are known as the Drift-Diffusion (DD) model for charge transport.

Following the Boltzmann statistics approximation for an intrinsic semiconductor, the electron and hole densities are given by [97]:

$$n = N_C \exp\left(\frac{E_{fn} - E_c}{k_B T}\right) \tag{1.15}$$

and

$$p = N_V \exp\left(\frac{E_v - E_{fp}}{k_B T}\right) \tag{1.16}$$

where, N_C and N_V are effective density of states (DOS) of conduction and valence bands, which have energies E_c and E_v, respectively. E_{fn}, and E_{fp} are the quasi Fermi energies of electron and holes, respectively. To calculate the DOS of conduction and valence bands, bulk density of state model has been used in this thesis. The model considers parabolic band approximation and Boltzmann's approximation for the perovskite semiconductors. The effective density of state in conduction and valence bands are given as [97]:

$$N_C = 2\left(\frac{2\pi(2m_{de}k_B T}{h^2}\right)^{3/2} \tag{1.17}$$

and

$$N_V = 2\left(\frac{2\pi(2m_{dh}k_B T}{h^2}\right)^{3/2} \tag{1.18}$$

where, m_{de} and m_{dh} are the density of state effective masses for the conduction and valence bands, respectively. In this study, the bulk density of states are considered. However, in general, the generalized density of state distribution can be adopted in a DD model. Furthermore, to include the quantum effects, quantum density of states, Kronig-Penney Model, Schrödinger/Poisson, electron-hole coupling, and other quantum mechanical and atomistic models can be combined with the DD model.

In a bulk DOS model, using equations 1.15 and 1.16, the intrinsic carrier concentration in equilibrium is given as:

$$n_i = p_i = N_0 \exp\left(\frac{-E_g}{2k_B T}\right) \tag{1.19}$$

where, $N_0 = \sqrt{N_c N_v}$. $E_g = (E_c - E_v)$ represents the material bandgap.

A semiconductor material can consist of charged and/or neutral traps that can trap the charge carriers. In case of neutral electron and hole traps, the trapped electron n_t and trapped hole p_t densities are given by:

$$n_t = \frac{N_t}{1 + \exp\left(\frac{E_{trap-E_{fn}}}{k_B T}\right)} \tag{1.20}$$

$$p_t = \frac{N_t}{1 + \exp\left(-\frac{E_{trap-E_{fp}}}{k_B T}\right)} \tag{1.21}$$

Where $E_{trap} = E_c - E_t$ or $E_{trap} = E_t - E_v$ is the trap density w.r.t. conduction and valence bands, respectively. E_t represents the absolute energy level of the trap with density of state (DOS) N_t. In case of donor and acceptor type of traps, the ionized trap densities are given as:

$$n_t^+ = N_t - \frac{N_t}{1 + \exp\left(\frac{E_{trap-E_{fn}}}{k_B T}\right)} \tag{1.22}$$

and

$$p_t^- = N_t - \frac{N_t}{1 + \exp\left(-\frac{E_{trap-E_{fp}}}{k_B T}\right)} \tag{1.23}$$

The Poisson's equation (1.5) can be modified based on the number and type of traps present in a material. The traps can lead to trap-assisted recombinations, and can change the charge densities ρ_n and ρ_p. If the net recombination rate of charge carriers is given by R, the electron and hole continuity equations, 1.12 and 1.13 can be rewritten as:

$$\nabla.\{\mu_n n\,(\nabla\phi_n)\} = -R \tag{1.24}$$

and

$$\nabla.\{\mu_p p\,(\nabla\phi_p)\} = R. \tag{1.25}$$

Upon light exposure, the electron-hole pairs are generated in a semiconductor material. These electron-hole pairs result in free electrons and holes within the semiconductor. If the net generation rate is given by G, equations 1.24 and 1.25 become:

$$\nabla.\{\mu_n n\,(\nabla\phi_n)\} = G - R \tag{1.26}$$

and

$$\nabla.\{\mu_p p\,(\nabla\phi_p)\} = -(G - R), \tag{1.27}$$

respectively.

Various trapping and recombination models can be implemented within DD, to model the role of traps and defects. Standard recombination models are bimolecular recombination, Shockley–Read–Hall (SRH) recombination, Langevin recombination, and Auger recombination. In this thesis, various recombination models are explained in different chapters where the role of the defects is studied. For light absorption and photogeneration, optical models such as constant generation, Lambert-Beer model, and Transfer-Matrix-Method (TMM) can be used.

To include the effect of charge carrier mobility, constant mobility, field-dependent mobility, and doping-dependent mobility models can be adopted based on the materials used.

In this thesis, a constant mobility model is used to consider μ_n and μ_p in the continuity equations.

Depending on the used materials and the device architecture, different submodels are adopted within the DD model. Furthermore, thermoelectricity, piezoelectricity, and elasticity models can be combined with DD, making this a versatile, flexible, fast, and reliable computational model to simulate semiconductor devices. The versatility of the DD model makes it a useful tool to simulate the charge carrier behavior in various electronic devices such as *pn* junction diodes, light-emitting-diodes (LEDs), solar cells, field-effect transistors, bipolar junction transistors, and photodetectors [98, 99, 100, 101, 102, 87, 82].

1.7 Outline and context of the work

The thesis investigates charge transport in perovskite solar cells. The roles of various trapping mechanisms are studied as performance-limiting factors in perovskite solar cells. Ways to improve charge transport, charge collection, and the cell performance are investigated using simulations and experimental methods.

Chapter 2 presents a one-dimensional steady-state drift-diffusion (DD) model for simulating a perovskite solar cell. A mathematical implementation of a coupled drift-diffusion equation in TiberCAD multiscale simulation tool is presented. Then, the transport and collection of the charge carriers is studied by simulating the role of the interface traps, contact workfunction, charge transport layer doping, and charge carrier mobility. Furthermore, perovskite interface functionalization is presented to improve the charge collection and the performance of PSCs.

Chapter 3 presents a DD study to investigate the role of grain boundaries in PSCs. A two-dimensional drift-diffusion is implemented in TiberCAD. The roles of defect states at the grain boundaries are simulated as centers for non-radiative recombination. Furthermore, the effect of ionic-defect accumulation is studied in different regions in the perovskite film, i.e., grain boundaries, the bulk of the grains, and the perovskite interfaces near the charge transport layers.

Chapter 4 investigates charge carriers and ionic-defect dynamics in PSCs. A time-dependent DD model is developed to study the well known JV hysteresis phenomenon in the PSCs. In contrast to existing literature, a new reason, "cation-mediated electron-hole recombination" is presented to contribute to the JV hysteresis. A detailed study is presented on the role of cation energy, ionic mobility, capture coefficient, and voltage scan rate on the JV hysteresis and the final efficiency of a PSC.

Chapter 5 focuses on the potential of OIHPs in a two-terminal (2T) all perovskite tandem solar cells. A drift-diffusion study is presented to optimize various material parameters (i.e., bandgap, mobility, workfunction, traps) and device parameters (i.e., subcell thickness, doping, interfaces regions) in a 2T all-perovskite tandem solar cell. Also, the impact of interface and bulk traps is studies on the tandem cell's final performance. The method presents experimentalists with an optimized design to obtain maximum efficiency of a tandem cell.

In Chapter 6, fabrication and characterization of semitransparent $CH_3NH_3PbBr_3$ PSCs is presented. A new chemical route using methylamine (MA) gas treatment is developed to obtain GBs-passivated perovskite films. The MA treated films result in improved optical transparency and charge transport. The improved charge transport in the

perovskite films translates into increased voltage, current, and the output efficiency of $CH_3NH_3PbBr_3$ PSCs. A proof of concept is presented by using opaque gold contacts. Finally, the gold contacts are replaced by transparent indium-doped tin oxide (ITO) contacts to realize efficient and semitransparent solar cell devices. The film characterization is done by transmittance, scanning electron microscopy, X-ray diffraction, and photoluminescence measurements. The solar cell devices are characterized by measuring current-voltage characteristics, internal photon-to-electron conversion efficiency, external power-conversion efficiency, maximum power point tracking, and optical transparency.

In the end, Chapter 7 summarized the outcomes of the work presented in this thesis.

2 1D steady-state simulations of perovskite solar cells

2.1 Background

Organic-inorganic hybrid perovskites (OIHPs) have gained extraordinary attention as an emerging material for photovoltaic applications. Low-temperature processable OIHPs show high optical absorption, long carrier diffusion lengths, and surprisingly low recombination rates [15, 14, 103]. Moreover, tunability of bandgap by compositional engineering [31, 104, 32] and solution processability [105] make perovskite-based solar cells potential alternatives to conventional solar cell technologies based on silicon. These favorable properties, in combination with great scientific effort have enabled high power conversion efficiencies beyond 25 % in single-junction perovskite solar cells (PSCs), and 29 % in silicon/perovskite tandem cells [5]. However, the reported efficiencies are still far from the theoretical limits of 31% for a single-junction and 42% for a 2-terminal tandem device [106]. Trap-assisted recombinations have been considered to be the main reason hampering the performance of PSCs [107, 103]. Several other loss mechanisms in PSCs are still unknown. Furthermore, the role of various material properties (i.e., mobility, defects) and device parameters (i.e., contacts, doping, interfaces) is not very well understood. By using time-resolved photoluminescence methods, the role of recombination processes can be understood as a whole device [103, 107, 108]. However, it is difficult to pinpoint which loss component originates from which layer/interface/contacts/grain boundaries.

Charge carrier mobility in various layers is one of the important factors determining the photovoltaic performance of PSCs. Carrier mobility depends on the choice of material and the fabrication scheme. In a full device, it is difficult to experimentally analyze the role of mobilities in individual layers. Theoretical studies on the other hand, can resolve the role of different mobilities, recombination components, and their impact on the final device performance. Similarly, theoretical and simulation studies can help to understand the individual roles of doping, material thickness, and contact workfunctions.

There have been several efforts to analyze perovskite solar cells by using theoretical models. A simple perovskite cell consisting of an electron transport layer (ETL), perovskite absorber, hole transport layer (HTL), and contacts can be simulated by using a drift-diffusion (DD) model. Transport of photogenerated (or injected) charge carriers in a semiconductor device is governed by the electric field and the concentration gradient induced diffusion of the carriers. Sherkar *et al.* [87] presented a DD model to analyze ITO(PEDOT:PSS)/PolyTPD/$CH_3NH_3PbI_3$/PCBM/Au device stack. They found that p-type doping in the PolyTPD layer can significantly improve the device performance in the given architecture. Minemoto *et al.* [86] presented a theoretical study to investigate the impact of conduction and valence band offsets of perovskite and blocking layers. However, Minemoto *et al.* used a 10nm artificial defect layer with a reduced bandgap to model the recombination, which limits the robustness of the results. Xu *et al.* used

drift-diffusion simulation to study interfacial recombination and charge transport layers (CTL) energy level positions [85]. Also, there have been studies to model the ionic migration in perovskite solar cells [82, 75, 109, 110, 111]. (Ionic modeling is discussed in more detail in chapter 4). Zhou *et al.* presented a coupled optical and electrical study to analyze the effect of the charge carrier diffusion length and the dielectric constant of absorber [112]. Most of the aforementioned studies focus on specific aspects of the device performance.

This chapter presents a broad drift-diffusion study to analyze the role of interface traps, contact workfunction, buffer thickness, mobility, CTL doping, and perovskite interface functionalization. The model is based on mapping a perovskite solar cell structure into a one-dimensional DD simulation model. The material and device properties are chosen from the literature. All the simulations are done for a steady-state device, and hence no transient phenomena are captured. The role of one parameter is studied at a time, to decouple the role of other parameters. The impact of material and device parameters on the open-circuit voltage, short-circuit current, fill-factor, and power conversion efficiency is investigated in detail. Optical generation profile, charge carrier distribution, and JV characteristics are calculated for a $CH_3NH_3PbI_3$ perovskite solar cell. Finally, the role of change in the interface workfunction near the perovskite/HTL interface is studied to improve the photovoltaic performance.

2.2 Simulation method

A one-dimensional finite element drift-diffusion model is implemented in the TiberCAD simulation tool [113, 114]. In the model, drift-diffusion and Poisson's equations are solved simultaneously for electrons, holes, and traps, accounting for light-absorption and electron-hole pair generation. Two buffers of 2 nm to 5 nm are defined on each side of the perovskite layer, as shown in Figure 2.1. These buffer layers have the material properties same as the perovskite layer. Interface traps are considered to be accumulated within these buffers.

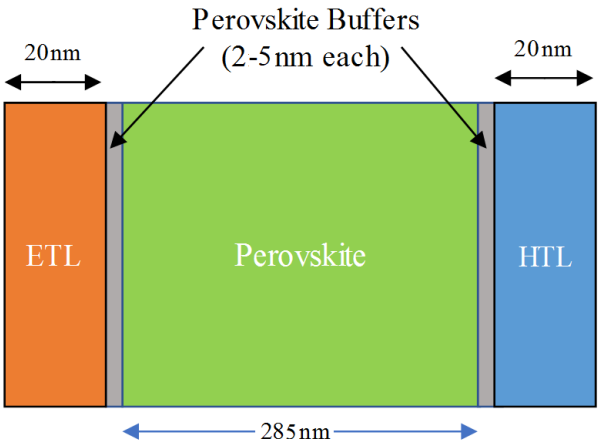

Figure 2.1: 1D simulation model of perovskite solar cell. Perovskite buffer regions consist of perovskite material with defect states.

Photogenerated electrons and holes in the bulk perovskite are transferred to the ETL and the HTL, respectively. Transport of these charges is governed by diffusion and electrically induced drift. Electrochemical potential and the electrostatic potential are used as variables dependent on the charge carrier distribution. The following is the complete set of drift-diffusion equations:

$$\begin{cases} \nabla \cdot (\epsilon \nabla \Phi) = e\left(n - p - N_d^+ + N_a^- - n_t^+ + n_t^-\right) \\ \nabla \cdot \{\mu_n n \left(\nabla \Phi_n\right)\} = G - R \\ \nabla \cdot \{\mu_p p \left(\nabla \Phi_p\right)\} = R - G \end{cases} \tag{2.1}$$

Where ϵ is the material dielectric permittivity and Φ the electrostatic potential. n, p, N_d^+ and N_a^- represent densities of electron, hole, ionized donor impurity and ionized acceptor impurity, respectively. Donor and acceptor trap densities are represented by n_t^- and n_t^+, respectively. μ_n and μ_p are the electron and hole mobility, respectively. Constant mobility is used in each layer. Φ_n and Φ_p are the electrochemical potentials of electrons and holes, respectively. Here, the first equation is Poisson's equation, and the last two equations are the continuity equations for the electrons and holes, respectively. G and R represent the net generation and recombination rates for the charge carriers, respectively. Photogeneration is governed by the Lambert-Beer model for absorption, given as:

$$G\left(x\right) = \int_{\lambda_{min}}^{\lambda_{max}} \varphi\left(\lambda\right) \alpha\left(\lambda\right) e^{-\alpha(\lambda)x} \, d\lambda \tag{2.2}$$

Here $G\left(x\right)$ is the generation rate at position x, $\varphi\left(\lambda\right)$ the solar light intensity, and $\alpha\left(\lambda\right)$ is the absorption coefficient at wavelength λ. The AM 1.5 standard spectrum between 350 nm and 2500 nm is used to calculate the optical generation. For the simplicity, constant $\alpha = 10\,\mu\mathrm{m}^{-1}$ is considered, which results in an exponential generation profile in the perovskite film with a maximum charge generation rate of $1.5 \times 10^{22}\,\mathrm{cm}^{-3}\,\mathrm{s}^{-1}$. Optical generation is considered within the perovskite and the buffers regions. No charge carriers are generated in the transport layers. Direct recombination is considered in all the perovskite layers. The direct or bimolecular recombination is radiative recombination of electron and hole, given by:

$$R_{\mathrm{direct}} = C\left(np - n_i^2\right) \tag{2.3}$$

Where C is bimolecular recombination rate constant and n_i is the equilibrium carrier density. The trap-assisted non-radiative recombination is considered in the buffer regions, defined by a Shockley-Read-Hall recombination rate, as follows [115, 116, 117]:

$$R_{\mathrm{SRH}} = N_t \frac{\upsilon_{th}^n \sigma^n \upsilon_{th}^p \sigma^p (np - n_i^2)}{\upsilon_{th}^n \sigma^n \left(n + n_1\right) + \upsilon_{th}^p \sigma^p \left(p + p_1\right)} \tag{2.4}$$

where N_t is the trap density, $\sigma^{n,p}$ are the capture cross sections, and $\upsilon_{th}^{n,p}$ are the thermal velocities of the electron and the hole. n_1 and p_1 are defined as:

$$n_1 = N_c \; exp\left(\frac{-E_c + E_T}{k_B T}\right) \quad \text{and} \quad p_1 = N_v \; exp\left(\frac{-E_T + E_v}{k_B T}\right), \tag{2.5}$$

where N_c the N_v are the effective density of state of the conduction and the valence bands, respectively. E_c, E_v and E_T are the conduction band, valence band and trap

energy levels, respectively. k_B is the Boltzmann coefficient, and T represents the absolute temperature. Trap-assisted recombination is most effective for the traps located at midgap [118]. Therefore, midgap donor and acceptor traps are considered in this study. It has been proved that recombination in bulk must be small due to the long diffusion length of charge carriers. Thus recombination must concentrate at the interface where defects and trap states concentrate too. For this reason, in this study, the traps are considered within the interface buffer regions only. Initially, both the buffers are considered to be 5 nm thick. The parameters used for the drift-diffusion simulations are summarized in Table 2.1.

Table 2.1: List of parameters used in the drift-diffusion simulation. Values of the parameters marked with asterisks(*) are varied during the simulation.

Parameter	Value	Units	Ref.
Perovskite thickness	285	nm	[87]
Perovskite bandgap	1.55	eV	[119]
Perovskite valence band maximum	-5.45	eV	[119]
Electron and hole mobility in Perovskite	8	$\mathrm{cm^2\,V^{-1}\,s^{-1}}$	[15]*
Electron mobility in PCBM	5×10^{-3}	$\mathrm{cm^2\,V^{-1}\,s^{-1}}$	[120]
Hole mobility in PCBM	1×10^{-10}	$\mathrm{cm^2\,V^{-1}\,s^{-1}}$	fit
Hole mobility in PolyTPD	1×10^{-3}	$\mathrm{cm^2\,V^{-1}\,s^{-1}}$	[121]
Electron mobility in PolyTPD	1×10^{-10}	$\mathrm{cm^2\,V^{-1}\,s^{-1}}$	fit
Perovskite relative permittivity	24.1	—	[122]
PCBM relative permittivity	3.9	—	[123]
Ionized doping in PCBM	1×10^{14}	$\mathrm{cm^{-3}}$	[87]
PCBM LUMO	-5.9	eV	[124]
PCBM bandgap	1.8	eV	[125]
PolyTPD LUMO	-5.4	eV	[126]
PolyTPD bandgap	2.5	eV	[126]
PolyTPD permittivity	3	—	[87]
Ionized doping in PolyTPD	1×10^{15}	$\mathrm{cm^{-3}}$	[87]*
Electron and hole capture cross sections	2×10^{-14}	$\mathrm{cm^2}$	fit
Cathode Fermi level	-5.2	eV	*
Anode Fermi level	-4.05	eV	fit
Bimolecular recombination constant	1×10^{-10}	$\mathrm{cm^{-3}\,s^{-1}}$	[103]
Maximum charge carrier generation rate	1.5×10^{22}	$\mathrm{cm^{-3}\,s^{-1}}$	fit

The JV characteristics are calculated to study the effect of trap density, HTL doping, contact workfunction, buffer layers thickness, and perovskite mobility. Also, charge carrier generation rate and their distribution profiles are calculated in short-circuit (SC) and maximum-power-point (MPP) conditions. The photogeneration of the charge carrier is considered in the perovskite absorber (including the buffers). The generation rate is determined by the optics of the device, i.e., thickness, and absorption, and reflection spectrum of each layer and the device as a whole. The generation rate does not depend on the operating conditions such as open-circuit, short-circuit, and/or maximum-power-point (MPP). On the other hand, the JV characteristics depend on the optical and electrical properties of each layer and the energy alignment throughout the device. Fill-factor is

calculated by using the maximum power point current (J_{mpp}) and the voltage (V_{mpp}), open-circuit voltage (V_{oc}) and the short-circuit current density (J_{sc}):

$$\text{Fill-factor (FF)} = \frac{J_{\mathrm{mpp}} V_{\mathrm{mpp}}}{J_{\mathrm{sc}} V_{\mathrm{oc}}} \,. \tag{2.6}$$

2.3 Results and discussion

Using the parameters from table 2.1, steady-state current-voltage (JV) characteristics is calculated. Initially, an ideal device is considered without trap-assisted losses. Then, the traps are considered within the interface buffers as non-radiative recombination centers. Figure 2.2a shows the calculated JV characteristics for a $CH_3NH_3PbI_3$ perovskite solar cell with different trap densities at the interfaces (buffers). When there are no interface traps ($N_t = 0$), the cell gives an open-circuit voltage (V_{oc}) $\simeq 1.2\,\mathrm{V}$, and a short circuit current density (J_{sc}) of $22.60\,\mathrm{mA/cm^2}$. When the traps are introduced in the buffer regions, the V_{oc} starts decreasing. For $N_t = 1 \times 10^{16}\,\mathrm{cm^{-3}}$, the V_{oc} decreases to $1.07\,\mathrm{V}$, while the J_{sc} remains unchanged. This might be due to the fact that the charge carriers lose their energy in trapping process. More trap-centers lead to more losses and hence lower output voltage. At the maximum power point, both the current (J_{mpp}) and the voltage (V_{mpp}) decrease with increasing the trap density. Overall it can be inferred that the solar cell maximum power output decreases with the increasing trap density at the interfaces.

This power loss can be recovered (up to a certain extent) by improving the Fermi-levels matching at the interfaces. One way to achieve this is to dope the charge transport layers [87]. In this chapter, doping in the HTL is studied. The HTL doping changes the energy alignment at the perovskite/HTL interface. An improved energy alignment helps charge carriers to be collected at the contacts before they are trapped by the trap centers and the defects present at the interface. Figure 2.2b shows calculated JV profiles for various HTL doping levels while fixing the buffer trap density to be $5 \times 10^{15}\,\mathrm{cm^{-3}}$. It is observed that the V_{oc}, V_{mpp} and J_{mpp} increase with the doping in the HTL. The (V_{oc}) increases from $1.04\,\mathrm{V}$ to $1.09\,\mathrm{V}$ when the acceptor doping in PolyTPD (HTL) increases from $1 \times 10^{16}\,\mathrm{cm^{-3}}$ to $1 \times 10^{18}\,\mathrm{cm^{-3}}$.

As mentioned earlier, only the interface traps are considered here, and the bulk perovskite film is considered to be free of defects. In practical, the perovskite film (bulk) can consist of grain boundaries and other defects as trapping/recombination centers [127, 75, 73]. The role of grain boundaries-assisted traps is studied in chapter 3.

Apart from the transport layers doping, the contact workfunctions must be optimized to obtain a good energy alignment. Workfunctions of the contacts play an important role in determining the energy alignment within the device. Changing the contact workfunction changes the energy alignment and hence the charge extraction from the cell. For the simulations, Schottky type contacts are employed for the charge collection to the external circuit. So far, the cathode and anode workfunctions were fixed to $-5.2\,\mathrm{eV}$ and $-4.05\,\mathrm{eV}$, respectively. In the next analysis, the JV characteristics are calculated by varying cathode workfunction (Φ_{c}), while keeping anode workfunction (Φ_{a}) fixed at $-4.05\,\mathrm{eV}$. The trap density and the HTL doping are fixed at $5 \times 10^{16}\,\mathrm{cm^{-3}}$ and $1 \times 10^{15}\,\mathrm{cm^{-3}}$, respectively. Simulated JV profiles are shown in Figure 2.3a. This is observed that the V_{oc} does not change much as it remains $\simeq 1.05\,\mathrm{V} - 1.08\,\mathrm{V}$ while varying the cathode workfunction

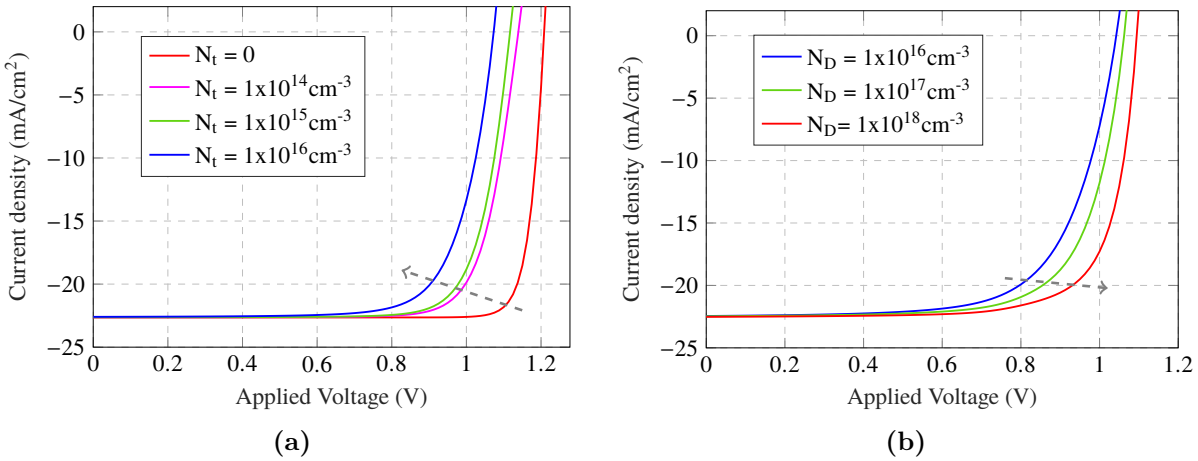

Figure 2.2: JV characteristics of perovskite solar cell: (a) For different trap densities in the buffers at a fixed HTL doping density of $1 \times 10^{15}\,\mathrm{cm}^{-3}$, and (b) For different HTL doping densities at fixed $N_t = 5 \times 10^{16}\,\mathrm{cm}^{-3}$. Dashed arrows show how the maximum power point changes with an increase in the trap or the doping density. Poor performance of a solar cell is obtained in the presence of trap centers. The performance improves with the HTL doping density.

between $-5.35\,\mathrm{eV}$ and $-5.15\,\mathrm{eV}$. The maximum-power-point voltage and the current vary significantly with the change in Φ_c. This leads to change the fill-factor and the output efficiency of the cell. For $\Phi_c < -5.35\,\mathrm{eV}$, the V_{oc} and fill factor don't change much. It means that for $\Phi_c < -5.35\,\mathrm{eV}$, the V_{oc} is not limited by the difference in the cathode and anode workfunctions. On the other hand, for $\Phi_c > -5.35\,\mathrm{eV}$, the V_{oc} and hence the solar cell performance is limited by the difference in the cathode and anode workfunctions.

Figure 2.3b shows the charge carrier (electron-hole pair) generation rate when the cell is exposed to the sunlight. The generation rate does not depend on the device's energy alignment but the optical properties of the individual layers and the device as a whole. In this study, the photogeneration is considered only in the active region (the perovskite film). Optical reflections from various layers are ignored, and hence an exponential charge carrier generation profile is obtained.

Though the charge carrier generation is not determined by the electrical properties of the layers (and hence the energetics throughout the device), the charge carrier transport and collection strongly depend on the energy alignment within the device. Along with the equilibrium energy alignment, the charge carrier distribution strongly depends on the operating conditions. Here, the charge carrier distribution profiles are calculated in two operating conditions; short-circuit and the maximum-power-point operation. Considering $N_t = 1 \times 10^{16}\,\mathrm{cm}^{-3}$, $N_d = 1 \times 10^{15}\,\mathrm{cm}^{-3}$, $\Phi_a = -4.05\,\mathrm{eV}$ and $\Phi_c = -5.2\,\mathrm{eV}$, the calculated charge carrier profiles are shown in Figure 2.4.

In the short-circuit condition, since there is no voltage applied (or supplied to a load), the charge carriers' distribution is determined by the optical generation rate, energy alignment, recombination profile, and mobility in each layer. Initially, in the dark condition, the intrinsic charge carriers distribute such that they obtain equilibrium with a built-in electric field developed between the contacts. When the cell is illuminated, the photogenerated electrons and holes start diffusing due to the concentration gradient. This movement of charges leads to develop a local electric field, and after that, the charge

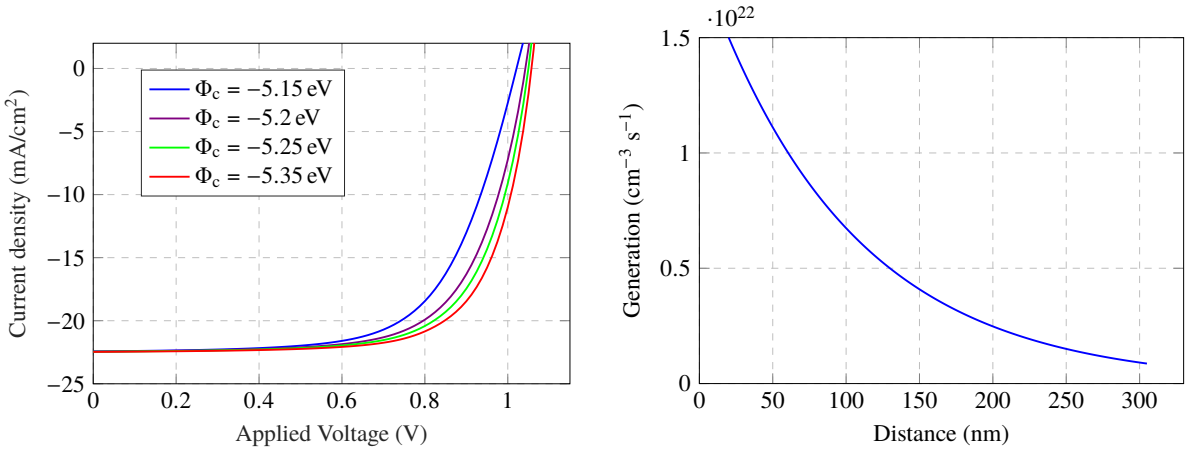

Figure 2.3: (a) JV characteristics of perovskite solar cell for different cathode workfunctions. The maximum-power point significantly changes with the change in the cathode workfunction. (b) Electron-hole pair generation profile in the perovskite absorber. The light absorption decreases with the distance (x) within the perovskite film, following the Lambert-Beer model for light absorption. The absorbed light then results into electron-hole pair generation. The electron-hole pairs quickly dissociate (due to the thermal energy) into electrons and holes.

transport is controlled by both the diffusion and the developed electric field. Because of the favorable energy alignment (led by the built-in electric field), the electrons travel towards the ETL, and the holes travel towards the HTL. Therefore, the electron (hole) density decreases (increases) from the ETL $\longrightarrow$ perovskite absorber $\longrightarrow$ HTL as shown in figure 2.4a.

When an external voltage is applied (or a load is connected), the electric field distribution and hence the charge-carrier drift changes. The applied electric field (due to the applied voltage) opposes the electrons (holes) to be collected at the ETL (HTL). This leads to flattening the electron and hole density curves in the perovskite region, as shown in Figure 2.4b. The electron density in the ETL is determined by Φ_a and the electron density at the perovskite/ETL interface. Similarly, the hole density in HTL is determined by the Φ_c and the hole density at the perovskite/HTL interface. Moreover, doping in the charge transport layers changes the charge carrier distribution in the transport layers and the device as a whole.

2.3.1 Impact of buffer layer thickness

The abrupt ending of a crystal (i.e., perovskite film) leads to dangling bonds and surface defects. The interface defect region's depth depends on the fabrication scheme and the lattice constant matching between the two materials interfacing with each other. So far, the simulations were done considering 5 nm buffer regions on each side of the perovskite absorber. The material properties for the buffer regions are considered to be the same as the perovskite absorber. Change in the perovskite buffers thickness while keeping a constant trap density leads to a change in the number of traps near the interfaces. Figure 2.5a shows JV characteristics for two different buffer thicknesses. All other parameters except the buffer thickness are kept unchanged. When a thicker buffer layer is considered,

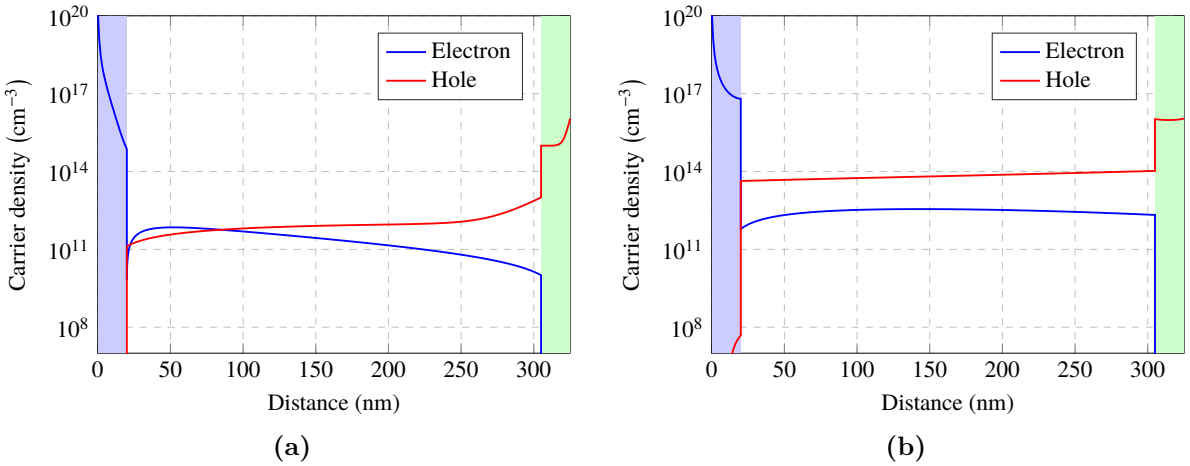

Figure 2.4: Electron and hole density profiles in (a) short circuit condition, and (b) at the maximum power point operation of the solar cell. At an applied bias (or a load voltage), the electrons and holes are redistributed to obtain a new equilibrium. Shaded light blue and light green regions represent ETL and HTL, respectively. Non-shaded white background region represent the perovskite region.

the V_{oc}, V_{mpp} and J_{mpp} deteriorate. This infers that if the defects are present deep in the perovskite films, poor performance is obtained for the cell. The effect of the grain boundaries as defect centers is discussed in chapter 3. For further analysis in this chapter, the thickness of the buffer is fixed to 2 nm.

2.3.2 Impact of perovskite mobility

The mobility of each layer plays a significant role in the charge extraction in a solar cell. Mobility determines the mean free path, the length at which the charge carriers travel before they recombine. A bulk perovskite film might consist of traps and defects. Hence, less mobility gives more time for the traps to trap the charge carriers. On the other hand, higher mobility helps charge carriers to escape before they are trapped (or recombined). The JV characteristics is very sensitive to the charge carrier mobility in the perovskite film. Within the perovskite films, both electrons and holes are in the majority; there is a fair chance of trap-assisted recombination. On the other hand, the transport layers (ELT and HTL) are more of monopolar charge carriers and hence less prone to trap-assisted recombination. In the presence of traps located in 2 nm buffer regions, the JV characteristics is calculated for a cell with different mobilities in the perovskite layer. As shown in Figure 2.5b, the JV characteristics varies significantly while varying mobility in the perovskite film. Calculated photovoltaic parameters are summarized in table 2.2. The short-circuit current remains almost unchanged. The V_{oc} decreases from 1.13 V to 1.09 V while increasing the mobility from 1 cm^2 V^{-1} s^{-1} to 10 cm^2 V^{-1} s^{-1}. However, there is a significant increase in Fill-factor with an increase in the mobility. Due to the improved Fill-factor, the efficiency increases from 17.40 % (for 1 cm^2 V^{-1} s^{-1}) to 19.54 % (for 10 cm^2 V^{-1} s^{-1}). The change in V_{oc} depends on the energetics throughout the device. A different trend can be observed for a different set of parameters (materials, device architecture).

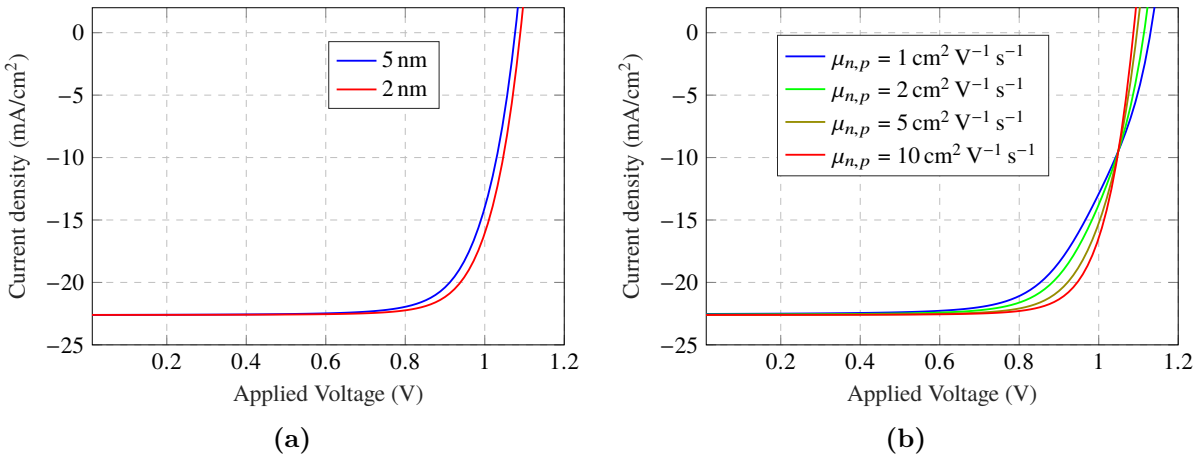

Figure 2.5: (a) JV characteristics of a cell with two different buffer layer thicknesses. (b) JV characteristics of a cell for different charge carrier mobility in the perovskite layer. Equal mobility for both the electrons and holes is considered in the perovskite.

Table 2.2: Photovoltaic performance parameters for different charge-carrier mobility $\mu_n = \mu_p$ (in units $cm^2\,V^{-1}\,s^{-1}$) in the perovskite layer.

μ_n, μ_p	V_{oc}(V)	J_{sc}(mA/cm^2)	FF (-)	PCE (%)
1	1.1302	22.5522	0.6839	17.3964
2	1.1161	22.5965	0.7167	18.0728
5	1.101	22.6236	0.7587	18.9497
10	1.094	22.6328	0.7906	19.5394

2.3.3 Impact of interface functionalization

As discussed earlier, energy alignment throughout the solar cell device plays a crucial role in charge transport and collection. Due to the limited number of available charge transport materials and transparent conductive oxides, it is not always possible to obtain the right energy alignment for all perovskite bandgaps. Also, doping of organic charge transport materials is not always easy and is an expensive procedure. Another possible way to overcome the aforementioned problem and to improve energy alignment is to use cascaded perovskite layers near the charge transport layers and/or contacts. Figure 2.6a represents a solar cell architecture with cascaded perovskite layers. Similarly, cascading by using multiple charge transport layers can be obtained. Although the cascading mechanism can improve the charge collection significantly, the fabrication process becomes very complex. Usually, perovskite layers deposited by using chemical methods employ perovskite precursors, solvent, and anti-solvent chemicals. Using of anti-solvents can harm the pre-deposited perovskite layers. Also, depositing multilayers of different materials can introduce interface defects due to the lattice constant mismatch between different layers. Therefore, interface modifications with fewer layers and minimal additional steps in fabrication are desired. Changing the perovskite energy levels near the perovskite/HTL and/or perovskite/ETL interfaces provides a path to improve the energy alignment without employing multilayers of perovskite [128, 129, 130]. Modifying the interface workfunction of the charge transport layers has been demonstrated to improve

the performance of perovskite solar cells [131, 85, 86]. Tuning the interface workfunctions accelerates the charge injection into the transport layers. In the aforementioned studies, ETL/HTL workfunction tuning has been achieved by introducing functionalizing molecules at the interface to create dipoles. A similar idea can be applied to tune the interface workfunction of the perovskite layer [132].

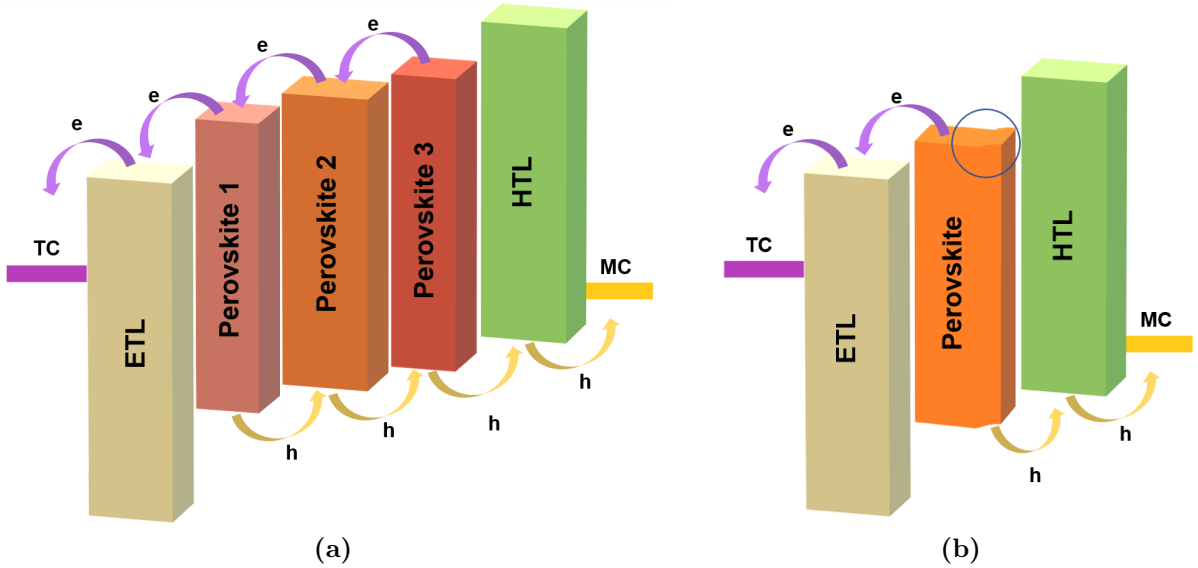

Figure 2.6: Two possible schemes to improve charge collection in a perovskite solar cell: (a) Perovskite solar cell with cascaded perovskite layers. TC and MC represent transparent contact and metal contact, respectively. (b) Perovskite solar cell with perovskite surface functionalized at the perovskite/HTL interface. The region in the blue circle shows upshifted conduction band of the perovskite. Similarly, perovskite valence band is up-shifted as the perovskite bandgap remains unchanged.

Lewis base and/or Lewis acids are proven to be the functionalizing reagents for perovskites/HTL interface by creating local dipole moments [70, 71, 133]. The direction of dipoles depends on the perovskite and the functionalizing reagent. Based on the direction of the dipoles, the perovskite workfunction increases or decreases near the surface. The workfunction change results in gradually varied valence and conduction band position of perovskite near the functionalized surface [134]. In this section, a drift-diffusion analysis is done to study the impact of the perovskite bandedge shift. The bandedge shift is modeled as a fixed 2 nm buffer layer (similar to buffers in Figure 2.1) with shifted bandedges. The upshift in the bandedge is considered as a positive shift, and vice-versa. Mobility in perovskite layer is considered to be $5\,\mathrm{cm^2\,V^{-1}\,s^{-1}}$. All other parameters are fixed as the subsection 2.3.2. Perovskite conduction and valence bands are shifted simultaneously. Figure 2.7a shows JV characteristics for different workfunction shifts in the perovskite at the perovskite/HTL interface. It is found that for the given device architecture, a workfunction shift of -25 meV to 100 meV, does not lead to change in the short circuit current. But, there is a significant change in the V_{oc} and the maximum power point voltage and current. Both the maximum power point current and voltage increase while increasing the workfunction shift. Because of the change in the maximum power point, the fill-factor of the cell changes. The fill factor of the cell increases from 0.6576 to 0.8408 while shifting the interface workfunction from -25 meV to 100 meV. Figure 2.7b shows

the change in the fill-factor with respect to the change in the perovskite surface workfunction. Although, the PolyTPD valence band (−5.4 eV) is very close to the perovskite valence band (−5.45 eV), there is a significant difference in the hole Fermi-levels. Downshifting the perovskite bandedge brings the hole Fermi-levels closer; therefore, the cell performance improves. Efficiency of the cell changes from 18.14 % (−25 meV) to 22.37 % (100 meV). For a shift of higher than 100 meV, hole injection from the perovskite to HTL becomes difficult; hence, there is no further improvement in the FF and the efficiency is observed. Similarly, for the negative bandshift, the perovskite conduction band becomes far apart from the HTL Fermi level (and conduction band), resulting in the cell's poor performance. Photovoltaic performance parameters for various band shifts are summarized in table 2.3.

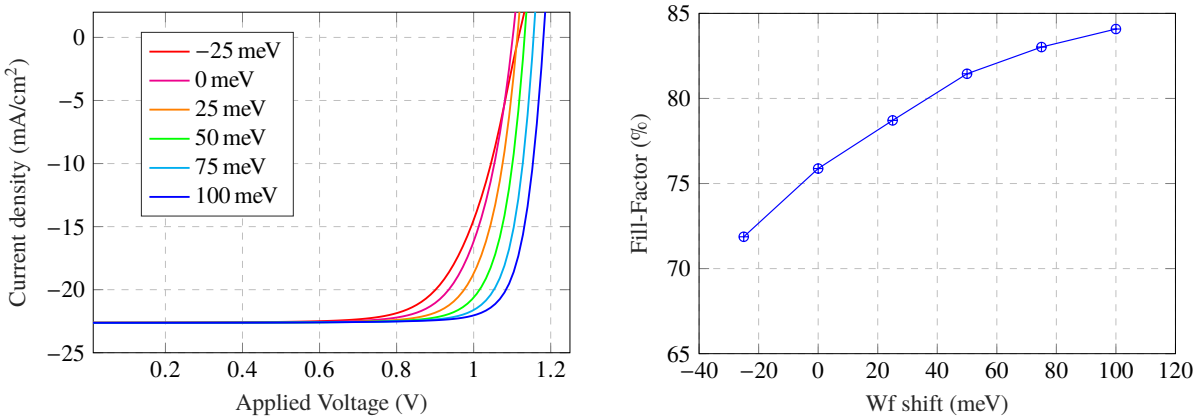

Figure 2.7: Impact of surface bandedge shift of perovskite: (a) JV characteristics for different bandedge shifts, and (b) Fill factor versus perovskite bandedge shift. The upward shift is considered as a positive shift. Both conduction and valence bands are shifted simultaneously.

Table 2.3: Photovoltaic performance parameters for different workfunction shift at the perovskite/HTL interface. Conduction and valence bands shift with the same amount as the workfunction. The upward shift has been considered to be a positive shift and vice-verse.

Shift (eV)	V_{oc}(V)	J_{sc}(mA/cm^2)	FF (-)	PCE (%)
−50	1.1960	22.6045	0.6576	17.8370
−25	1.1165	22.6176	0.7187	18.1420
0	1.1015	22.6236	0.7588	18.9525
25	1.1132	22.6260	0.7871	19.8756
50	1.132	22.6269	0.8145	20.7878
75	1.1551	22.6273	0.8302	21.6397
100	1.1812	22.6274	0.8408	22.3723

Similar behavior is obtained experimentally for triple cation perovskite solar cells when dipoles are created on the perovskite surface attached to Spiro-OMeTAD HTL [134]. These surface dipoles change the workfunction at the perovskite interface and hence change the photovoltaic parameters.

2.4 Conclusion

In conclusion, a one-dimensional drift-diffusion model is presented to simulate the steady-state operation of a $CH_3NH_3PbI_3$ perovskite solar cell. The role of material and device parameters are calculated in terms of photovoltaic performance parameters, i.e., V_{oc}, J_{sc}, P_{max}, and FF. For simplicity, a constant absorption coefficient, α is considered for the perovskite layer. The simulation results show that the V_{oc} and P_{max} deteriorate when the traps are introduced at the perovskite/HTL and perovskite/ETL interfaces. The interface traps lead to trap-assisted non-radiative recombination losses. Doping in the hole transport layer helps to improve the interface energetics and hence the solar cell performance. Choosing proper contact workfunctions is needed to optimize the cell performance. The charge carrier mobility in various layers determines the charge carrier transport within the layers and the device as a whole. The perovskite layer mobility is an important parameter to determine the output power of the solar cell. Increasing the mobility in the perovskite layer leads to decreased V_{oc}, but increased FF. An increase in FF ultimately results in increased output power of the cell. Furthermore, it is found that changing the perovskite workfunction near the perovskite/HTL interface changes the cell performance significantly. The cell efficiency changes from 17.84 % to 22.37 % while shifting the workfunction from -50 eV to 100 eV. Tuning the perovskite workfunction is a very useful technique to improve the interface energetics and hence the hole injection from perovskite to the HTL.

3 Role of grain boundaries in ion accumulation in perovskite solar cells

3.1 Background

Organic-inorganic hybrid perovskite (OIHP) materials offer solution processability and low-cost fabrication of perovskite solar cells (PSCs). However, very often, the solution process techniques end up with polycrystalline perovskite films [135, 91, 19, 127]. Breaks in the perovskite crystal structure lead to the formation of grain boundaries (GBs) at the breakpoints. Neighboring crystals with different orientations give rise to interstitials, dislocations, vacancies, dangling bonds, and distorted bond angles & bond distances at the boundaries. These defects can act as trapping centers for the charge carriers during the cell operation. Figure 3.1 represents a SEM image of a typical $CH_3NH_3PbI_3$ perovskite film obtained by using spin-coating. Due to the presence of defects (as trapping centers) at the GBs, they are regarded to be the main non-radiative recombination centers in a perovskite cell [127, 73, 75]. Despite other loss mechanisms, the non-radiative recombination losses have been considered to be the main factors limiting the perovskite solar cell performance [74, 136, 108, 87].

On the other hand, in OIHP films, organic cations, halide ions, and inorganic cations can come out of their original position in the crystal and move within the perovskite film. Similarly, the ionic vacancies can move within the perovskite film. There have been several studies claiming anions (I^- ions), cations (MA^+, Pb_2^+), vacancies and interstitial to move within the perovskite film [76, 77, 78]. It has also been reported that the ions prefer to move via the grain boundaries (GBs) rather than the bulk due to the low activation energies at the boundaries of the grains [137, 138, 139]. Overall, the GBs hamper the perovskite solar cell performance in two ways: (1) by hosting defects/trapping centers for the charge carries, and (2) by providing a channel for the ionic defect migration. A reduction in the number of GBs suppresses both the non-radiative recombination and the ionic migration. It has been proven that the perovskite films with larger grains and hence fewer GBs result in better performing solar cells [137, 139, 138, 140, 19].

There have been efforts to develop drift-diffusion methods (DD) to study the role of GBs in perovskite solar cells. Sherkar *et al.* [87] presented a one-dimensional model to define traps at the HTL/perovskite and ETL/perovskite interfaces to account for the open grain boundary traps. Ameri *et al.* [142] studied electronic activity of the grain boundaries in perovskite solar cells. Olyaeefar *et al.* [143] modeled grain size and boundary effects in polycrystalline perovskite solar cells. In another study, Sherkar *et al.* [75] investigated the role of the nature (positively/negatively charged or neutral) of interface and grain boundary traps. All these studies consider one-dimensional DD models, where a point or a small region of a line (i.e., 1 nm) defines a GB. However, in a real perovskite film (see Figure 3.1), the GBs are distributed within the perovskite film in a complex shape rather than just a point or a line.

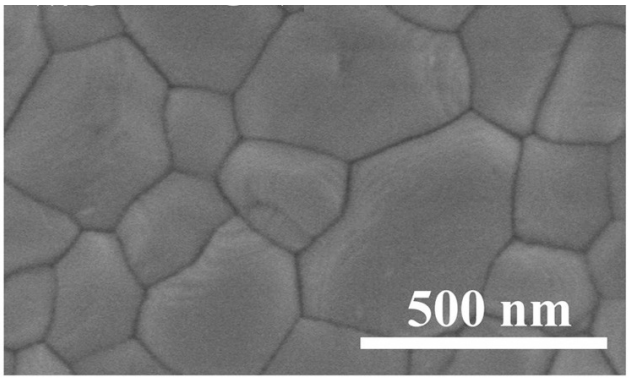

Figure 3.1: Top-view scanning electron microscopy (SEM) image of $CH_3NH_3PbI_3$ perovskite film deposited on ITO/NiO [141]. Reproduced with permission of American Chemical Society (Copyright © 2018, American Chemical Society).

This chapter presents a more accurate way to map GBs in a two-dimensional (2D) plane. The 2D model represents a cross-section of a three-dimensional perovskite film. The role of GBs is studied as a host for the traps and a channel for the ionic movements. Two-dimensional drift-diffusion simulation model of a $CH_3NH_3PbI_3$ perovskite solar cell is used to analyze the steady-state performance of the cell consisting of GBs and interfaces. The impact of the traps and ionic accumulation at the GBs and interfaces is studied on the photovoltaic performance of the cell.

3.2 Simulation method

A finite element two-dimensional drift-diffusion (DD) simulation model is implemented within TiberCAD. The model is similar to the one explained in chapter 2 except for solving the coupled DD equation in a two-dimensional domain. In a 2D domain, it is easy to define the grain boundaries in the perovskite layer. A two-dimensional simulation block with perovskite film consisting of grain boundaries, an electron transport layer (ETL), and a hole transport layer (HTL) is shown in Figure 3.2a. The finite element input mesh file is generated by using Gmsh software, is shown in Figure 3.2b. To simulate the solar cell device, a block of 300 nm x 500 nm is considered. The block is large enough to properly include photogeneration, charge transport, surface phenomena, and the effect of the grain boundaries. The model is based on solving drift-diffusion and Poisson equations simultaneously for electrons, holes, fixed charges, and traps. The electron-hole pair generation by absorbing sunlight in the perovskite film and the charge transport are solved simultaneously. Interface traps are considered within the perovskite buffer regions. All the simulations have been done for a steady-state device. Various distributions of ionic defects are considered. At a given time, in the steady-state, a fixed ionic distribution is considered. When the ions are distributed at the fixed positions, they can be considered as fixed charges. Therefore, in this chapter, the ions have been modeled as fixed charges distributed within the perovskite film.

The charge transport is governed by coupled drift-diffusion equation as follows:

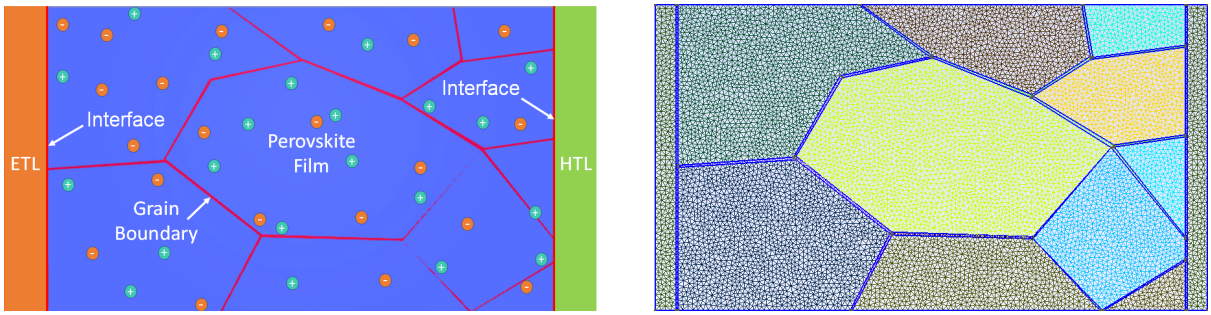

(a) (b)

Figure 3.2: (a) 2-dimensional drift-diffusion simulation block. The blue region represents the perovskite film, and the grain boundaries are denoted by the red lines. The size of negative (orange circle) and positive ions (green circle) is just representative. Reproduced with permission from ref [144], Copyright © 2020, IEEE. (b) A finite element input mesh generated by using the Gmsh tool.

$$\begin{cases} \nabla \cdot (\epsilon \nabla \Phi) = -q \left(n - p + N_a^- - N_d^+ + n_t^- - n_t^+ - n_f^+ + n_f^- \right) \\ \nabla \cdot \{ \mu_n n \left(\nabla \Phi_n \right) \} = -R + G \\ \nabla \cdot \{ \mu_p p \left(\nabla \Phi_p \right) \} = R - G \end{cases} \tag{3.1}$$

n_f^- and n_f^+ represent negatively (anions) and positively (cations) charged ionic defects, respectively. All other parameters have their usual meaning as described in equation 2.1. Photogeneration profile is calculated by using Lambert-Beer model for absorption, governed by equation 2.2. The absorption coefficient $\alpha\left(\lambda\right)$ is determined by the imaginary part of refractive index κ [145, 146]:

$$\alpha = \frac{4\pi\kappa}{\lambda} \tag{3.2}$$

κ values are chosen following Ball *et al.* [146]. The AM 1.5 standard spectrum between 300 nm and 900 nm is used to calculate the optical generation. Two type of recombination processes, radiative (direct) and non-radiative (trap-assisted) recombination are considered in the perovskite film. The radiative recombination is defined by equation 2.3. To include the effect of trapping of charge carriers, Shockley-Read-Hall recombination rate is given by [115, 116, 117]:

$$R_{SRH} = \frac{np - n_i^2}{\left(n + n_i e^{E_t/k_B T}\right) \tau_p + \left(p + p_i e^{-Et/k_B T}\right) \tau_n} \quad , \tag{3.3}$$

where $E_t = E_{trap} - \left(E_c + E_v\right)/2$ is the trap energy level with respect to the midband energy, and τ_n and τ_p are the trapping times of electrons and the holes, respectively. The trapping time is defined in terms of trap capturing coefficient $C_{p,n}$ and the trap density as follows:

$$\tau_{n,p} = \frac{1}{N_t C_{n,p}} \quad , \tag{3.4}$$

where $C_{n,p}$ represents the probability of the charge carriers to be trapped. Higher trap density N_t implies more trapping and a smaller trapping time, and vice-versa. Recombination has been shown to be most effective when the traps are located in the midgap

[118]. For this reason, both the donor and acceptor traps are considered to be located in the middle of the bandgap. The parameters used for the drift-diffusion simulations are shown in table 3.1.

Table 3.1: List of parameters used in 2-dimensional drift-diffusion calculations. Reproduced with permission from ref [144], Copyright © 2020, IEEE.

Parameter	Value	Units	Ref.
Electron mobility in perovskite	5	$cm^2\,V^{-1}\,s^{-1}$	[15]
Hole mobility in perovskite	5	$cm^2\,V^{-1}\,s^{-1}$	[15]
Perovskite valence band	-5.43	eV	[147]
Perovskite conduction band	-3.88	eV	[147]
Perovskite relative permittivity	24.1	—	[122]
TiO_2 bandgap	3.2	eV	[148]
TiO_2 conduction band	-4.0	eV	[148]
Electron mobility in TiO_2	0.02	$cm^2\,V^{-1}\,s^{-1}$	[148]
Hole mobility in TiO_2	1×10^{-7}	$cm^2\,V^{-1}\,s^{-1}$	fit
TiO_2 relative permittivity	85	—	[149]
Spiro-OMeTAD bandgap	3.17	eV	[150]
Spiro-OMeTAD LUMO	-5.22	eV	[150]
Spiro-OMeTAD relative permittivitty	3	—	[151]
Acceptor doping in Spiro-OMeTAD	1×10^{17}	cm^{-3}	fit
Electron mobility in Spiro-OMeTAD	1×10^{-7}	$cm^2\,V^{-1}\,s^{-1}$	fit
Hole mobility in Spiro-OMeTAD	0.01	$cm^2\,V^{-1}\,s^{-1}$	[152]
Anode Fermi level	-4.3	eV	[153]
Cathode Fermi level	-5.1	eV	[153]
Bimoleular recombination rate	1×10^{-10}	$cm^{-3}\,s^{-1}$	[103]
Maximum optical generation rate	1.4×10^{22}	$cm^{-3}\,s^{-1}$	fit

3.3 Results and discussion

Initially, the impact of interface traps is studied without considering ions in the perovskite film. Interface traps are modeled by the buffer layers defined near the perovskite/HTL and perovskite/ETL interfaces. Similar to interface traps, traps are considered to be present within the grain boundaries. These traps act as recombination centers for the charge carriers. Equal trapping time $\tau_p = \tau_n$ is considered for both the electrons and the holes. After investigating the role of traps, negatively charged ions are introduced in various regions of the perovskite film. Finally, both positive and negative ions are introduced in the film. The photovoltaic performance is calculated in terms of short-circuit-current, open-circuit-voltage, fill-factor, and the maximum-power-point efficiency of the cell. All the aforementioned photovoltaic parameters are calculated for the cell in steady-state for different ionic distributions. Fill-factor is calculated by equation 2.6 as described in chapter 2. Detailed analysis is given in the following subsections.

3.3.1 Impact of interface and grain boundary traps

In this section, the role of grain boundaries and interface traps is investigated without considering the ionic defects. Initially, JV characteristics of $CH_3NH_3PbI_3$ perovskite

solar cells are calculated without traps (without non-radiative recombination losses). In this case, an open-circuit voltage (V_{oc}) of 1.19 V and short-circuit-current (J_{sc}) of 21.74 mA/cm^2 are obtained from the cell. The cell shows very good fill-factor of 0.87, and output power density of 22.67 mW/cm^2. In the next step, traps are introduced at the interfaces and the GBs. Equal trapping time $\tau_p = \tau_n$ is considered for both the acceptor (hole) and donor (electron) traps. Calculated steady-state JV-characteristics for different recombination times are shown in figure 3.3. It is observed that the V_{oc} decreases with decreasing the trapping time. Also, V_{mpp}, J_{mpp} and the fill-factor decrease in the presence of traps as recombination centers. Photovoltaic parameters for the cell with different trapping time summarized in table 3.2.

Table 3.2: Calculated photovoltaic performance parameters for $CH_3NH_3PbI_3$ perovskite solar cell considering grain boundaries and interface traps. The role of ionic defects has been ignored in this section.

$\tau_n = \tau_p$ (s)	J_{sc} (mA/cm^2)	V_{oc} (V)	J_{mpp} mA/cm^2	V_{mpp} (V)	FF (-)	Max Power (mW/cm^2)
No Traps	21.7443	1.191	20.9873	1.080	0.8753	22.6684
5×10^{-8}	21.7235	1.154	19.7917	0.9842	0.7770	19.4786
5×10^{-9}	21.7162	1.143	19.6522	0.9602	0.7609	18.8701
1×10^{-9}	21.6841	1.111	19.5601	0.8883	0.7212	17.3745
5×10^{-10}	21.6442	1.087	19.5974	0.8403	0.6999	16.4677
1×10^{-10}	21.3358	1.013	0.7684	17.9666	0.6387	13.8048
5×10^{-11}	18.8056	0.884	13.6786	0.6005	0.4941	8.2140

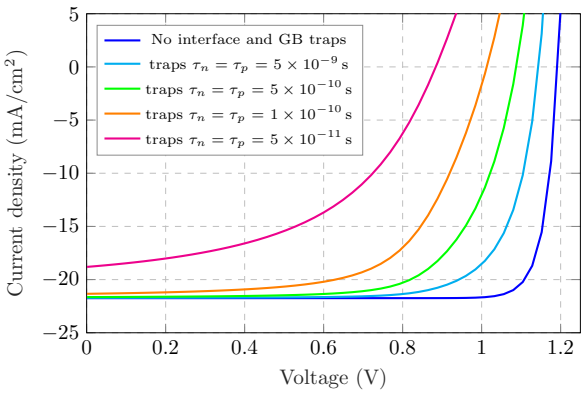

Figure 3.3: JV characteristics of $CH_3NH_3PbI_3$ perovskite solar cell without ionic defects. τ_n, τ_p represent electron and hole trapping times at the interfaces and grain boundaries. Reproduced with permission from ref [144], Copyright © 2020, IEEE.

While decreasing $\tau_p = \tau_n$ up to 5×10^{-11} s, the J_{sc} does not change much. However, significant change in other photovoltaic performance parameters is observed. For shorter $\tau_p = \tau_n$, (i.e. 5×10^{-11} s), J_{sc} decreases significantly along with other parameters. For this trapping time, the output power density goes down to 8.21 mW/cm^2. This output power does not justify high efficiencies obtained experimentally for perovskite solar cells [5]. Therefore, $\tau_n = \tau_p < 5 \times 10^{-10}$ s are not practical values for the perovskite cells. For further analysis, $\tau_n = \tau_p = 5 \times 10^{-10}$ s is considered to account for the effect of interface and grain boundary traps [103].

3.3.2 Only negative ions

To study the impact of ion distribution, initially, the negative ions (anions) are considered in the active layer. Steady-state JV analysis shows that, when the anions are uniformly distributed in the perovskite film, they do not affect the JV unless they exceed a very high density, such as $5 \times 10^{18}\,\mathrm{cm}^{-3}$. The presence of such high bulk ion densities is not practical in OIHPs. In the presence of a photocurrent generated electric field, the anions start moving towards the ETL. When the ions start accumulating in different regions, they affect the transport of electrons and holes. Previous studies have suggested that the ions move faster within the grain boundaries than the bulk of the grain [137, 138, 154, 139]. Here, three different anion distribution profiles are considered within the grain boundaries and at the interfaces, as shown in Figure 3.4.

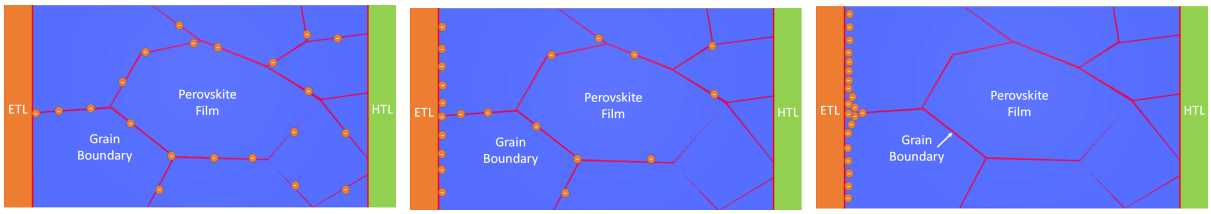

(a) **(b)** **(c)**

Figure 3.4: Distribution of anions: (a) at the grain boundaries (GBs), (b) at the GBs and perovskite/ETL interface, and (c) at perovskite/ETL Interface.

Initially, a case is considered when all the anions from the bulk of grains come to the grain boundaries, as shown in Figure 3.4a. Calculated short circuit current (J_{sc}) for this case is shown by the red curve in Figure 3.5. X-axis in the figure represents the initial anion density present at the grain boundaries (GBs). The J_{sc} start decreasing when the anion density at the GBs exceeds $1 \times 10^{17}\,\mathrm{cm}^{-3}$. The J_{sc} further decreases with an increase in the anion density. Calculated photovoltaic parameters are summarized in table 3.3. The fill-factor and the output power density decrease with increasing the anion density within the grain boundaries.

Table 3.3: Calculated photovoltaic parameters for $CH_3NH_3PbI_3$ perovskite solar cell considering anions within the grain boundaries.

Anion density (cm^{-3})	J_{sc} ($\mathrm{mA/cm}^2$)	V_{oc} (V)	FF (-)	Max Power ($\mathrm{mW/cm}^2$)
1×10^{16}	21.6634	1.095	0.6977	16.6865
5×10^{16}	21.6602	1.096	0.6880	16.4521
1×10^{17}	21.6549	1.101	0.6761	16.1656
5×10^{17}	21.4658	1.142	0.5781	14.2965
1×10^{18}	19.5105	1.159	0.6005	13.4968
5×10^{18}	13.6595	1.177	0.6323	10.1579
1×10^{19}	10.0408	1.176	0.6313	7.4548

In the next analysis, the anion movement is considered such that some of the anions reach the ETL/perovskite interface, and the remaining anions remain in the GBs (see Figure 3.4b). In this case, as the anions are distributed within the GBs and the interface,

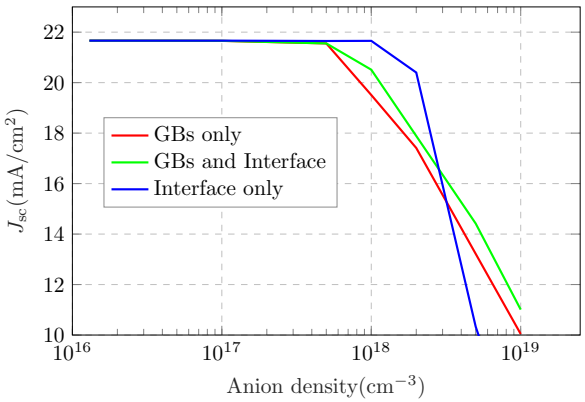

Figure 3.5: Calculated short-circuit current density (J_{sc}) for the cell with anions in various regions of the perovskite layer. Initially, the anions are distributed within grain boundaries (GBs). Then, the anions start moving towards the perovskite/ETL interface. Finally, all the anions accumulate near the perovskite/ETL interface (Interface only). The anion density corresponds to the initial anion density within the GBs. Reproduced with permission from ref [144], Copyright © 2020, IEEE.

the anion density becomes smaller compared to the case when all the ions were distributed within the GBs. Therefore, a higher J_{sc} is obtained compared to the earlier case. The J_{sc} for this case is represented by the green curve in Figure 3.5. Calculated photovoltaic parameters for this distribution are summarized in table 3.4. The FF and the output power decrease with an increase in the anion density, similar to the previous case.

Table 3.4: Calculated photovoltaic parameters considering anions distributed within the grain boundaries and near the perovskite/ETL interface. Anion density corresponds to the initial ion density within the grain boundaries.

Anion density (cm^{-3})	J_{sc} (mA/cm^2)	V_{oc} (V)	FF (-)	Max Power (mW/cm^2)
1×10^{16}	21.6635	1.095	0.6981	16.6980
5×10^{16}	21.6609	1.096	0.6989	16.5085
1×10^{17}	21.6570	1.099	0.6812	16.2587
5×10^{17}	21.5542	1.138	0.5931	14.5746
1×10^{18}	20.5122	1.156	0.5795	13.6932
5×10^{18}	14.4165	1.177	0.6239	10.5782
1×10^{19}	11.0078	1.178	0.6067	7.8543

Finally, a case is considered when all the anions reach and accumulate at the ETL/perovskite interface, as shown in Figure 3.4c. Accumulation of anions forms an electronic barrier for the electrons near the interface. The barrier slows down the electron transport; therefore, it gives more time for the interface traps to trap the electrons. This leads to an abrupt drop in the J_{sc} for an anion density exceeding $5 \times 10^{18}\,cm^{-3}$, as shown by the blue curve in Figure 3.5. Photovoltaic parameters for various anion distributions are summarized in table 3.5. For anion density exceeding $5 \times 10^{18}\,cm^{-3}$, due to poor output current, the FF and the output power also drop rapidly compared to the cases when the anions were distributed within the GBs, and the GBs and interface. From here, it can

be inferred that the anions make a maximum impact when they accumulate near the perovskite/ETL interface.

Table 3.5: Calculated photovoltaic parameters considering all the anions accumulated near the perovskite/ETL interface. Anion density corresponds to the initial anion density within the grain boundaries.

Anion density (cm^{-3})	J_{sc} (mA/cm^2)	V_{oc} (V)	FF (-)	Max Power (mW/cm^2)
1×10^{16}	21.6640	1.096	0.7001	16.7467
5×10^{16}	21.6638	1.096	0.6993	16.7267
1×10^{17}	21.6636	1.097	0.6983	16.7019
5×10^{17}	21.6619	1.099	0.6898	16.4979
1×10^{18}	21.6556	1.101	0.6787	16.2307
5×10^{18}	10.3276	1.115	0.5491	6.3334
1×10^{19}	5.0078	1.150	0.3851	2.2183

3.3.3 Both positive and negative ions

In the previous section, only the anions were considered in the perovskite film. A real perovskite cell can consist of both positive (cations) and negative (anions) ionic defects within the perovskite film. This section investigates solar cell performance considering both types of ions. When both the anions and cations are uniformly distributed within the perovskite film, they do not affect the solar cell performance for the given practical ionic densities ($<1 \times 10^{19}\,cm^{-3}$). In the presence of a photogenerated electric field, the anions (cations) move towards the perovskite/ETL (perovskite/HTL) interface. Previous studies have suggested that positive ions (iodine vacancies V_I, lead interstitial I_{Pb}, and and methylammonium interstitial I_{MA}) have higher activation energies and lower diffusion coefficients compared to the negative ionic defects (iodine interstitial I_I, methylammonium vacancies V_{MA}) [155, 77, 156, 76]. Since the negative ions have higher mobility, they accumulate much faster than the positive ions at the GB and interfaces. Three possible ionic distributions are shown in Figure 3.6. Here, the impact of two ionic distribution profiles is studied during the cell operation. The first distribution corresponds to a case when the anions have reached the interface while the cations are still within the GBs, as shown in Figure 3.6b. The second distribution is considered such that all the ions accumulate near the respective interfaces, as shown in Figure 3.6c.

Calculated short-circuit current density for the first case (Figure 3.6b) is shown by green curve in Figure 3.7. The J_{sc} decreases with the ion density. For an ion density of $1 \times 10^{19}\,cm^{-3}$, the J_{sc} reduces to $\simeq 11\,mA/cm^2$. The solar cell performance parameters for this case are summarized in table 3.6. When both the anions and the cations accumulate at the respective interfaces, the J_{sc} drops rapidly for ion density exceeding $1 \times 10^{18}\,cm^{-3}$. The solar cell performance parameters for this case are summarized in table 3.7.

Figure 3.8 compares maximum output power (P_{max}) for the cases when only the anions, and both the anions and cations are considered. P_{max} is calculated for the steady-state operation of the cell. When only anions are present in the perovskite film, the cell gives good output power for ions density up to $\simeq 2 \times 10^{18}\,cm^{-3}$.

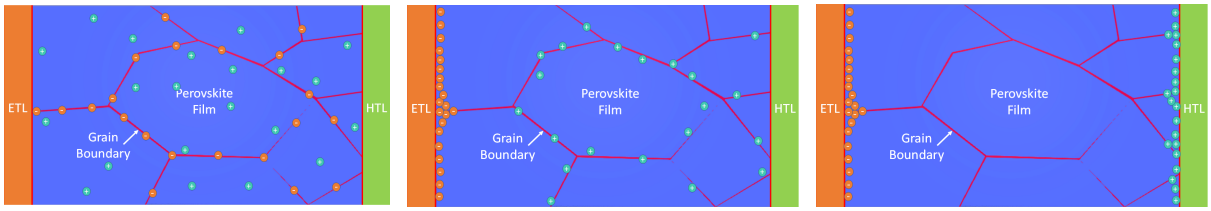

Figure 3.6: Distribution of ions: (a) Cations distributed within the bulk of the perovskite film, while the anions accumulated within the grain boundaries (GBs). (b) Anions have reached the perovskite/ETL interface, and cations are distributed within the GBs. (c) The anions reach the perovskite/ETL interface, and the cations reach the perovskite/HTL interface.

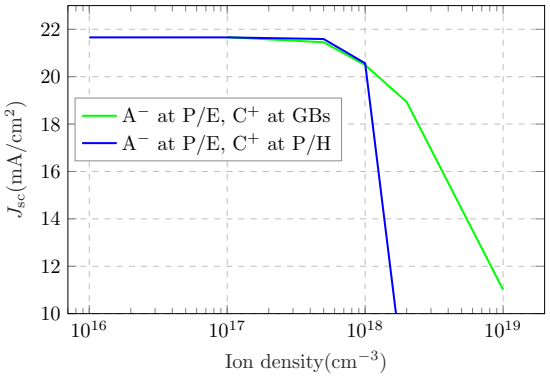

Figure 3.7: Calculated short-circuit current density for the cell with different distributions of anions (A^-) and cations (C^+). GBs stands for the grain boundaries. P/E and P/H represent the perovskite/ETL and perovskite/HTL interfaces, respectively. Reproduced with permission from ref [144], Copyright © 2020, IEEE.

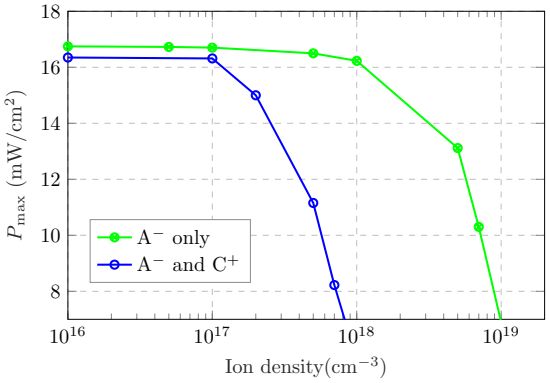

Figure 3.8: Maximum out power density (P_{max}) for the cell with equal ionic densities at the interfaces. The ions move through the grain boundaries to the interfaces. Anions (A^-) accumulate within the perovskite buffer near the perovskite/ETL interface. Cations (C^+) accumulate within the perovskite buffer near the perovskite/HTL interface. Ion density at the X-axis represents the initial ion density within the grain boundaries. Reproduced with permission from ref [144], Copyright © 2020, IEEE.

For anion density of $1 \times 10^{18}\,\mathrm{cm}^{-3}$, a power density of $16.23\,\mathrm{mW/cm}^2$ is obtained. When both the positive and negative ions are considered, the power density drops to

Table 3.6: Calculated photovoltaic parameters considering anions accumulated near the Perovskite/ETL interface, and cations accumulated within the grain boundaries. Ion density corresponds to the initial ion density within the grain boundaries.

Anion density (cm^{-3})	J_{sc} (mA/cm^2)	V_{oc} (V)	FF (-)	Max Power (mW/cm^2)
1×10^{16}	21.6681	1.102	0.7105	16.9654
5×10^{16}	21.6681	1.102	0.7100	16.9535
1×10^{17}	21.6681	1.107	0.7008	16.8097
5×10^{17}	21.4527	1.141	0.6900	16.8895
1×10^{18}	20.4924	1.160	0.7000	16.6398
2×10^{18}	18.9345	1.175	0.7104	15.8050
5×10^{18}	14.5606	1.128	0.6000	09.8546
1×10^{19}	11.0078	1.150	0.3851	04.8749

Table 3.7: Calculated photovoltaic parameters considering anions accumulated in the buffer near the Perovskite/ETL interface, and cations accumulated in the buffer near the Perovskite/HTL interface. Ion density corresponds to the initial ion density within the grain boundaries.

Anion density (cm^{-3})	J_{sc} (mA/cm^2)	V_{oc} (V)	FF (-)	Max Power (mW/cm^2)
1×10^{16}	21.6583	1.102	0.6850	16.3484
5×10^{16}	21.6579	1.1031	0.6798	16.3150
1×10^{17}	21.6579	1.1041	0.6823	16.3157
5×10^{17}	21.5897	1.151	0.4489	11.1549
1×10^{18}	20.5654	1.123	0.2407	5.5587
2×10^{18}	6.3333	1.132	0.4448	3.1889
5×10^{18}	1.7308	1.150	0.5756	1.1456

$5.56\,mW/cm^2$ for ion density (initial ion density at the grain boundaries) of $1 \times 10^{18}\,cm^{-3}$. In both of the cases, the P_{max} drops with an increase in the ion density. From here, this can be concluded that, the cell performance is most affected when both the ions accumulate near the interfaces.

3.4 Conclusion

In conclusion, the grain boundary traps along with the interface traps deteriorate the perovskite solar cell performance. Shorter trapping time leads to more non-radiative recombination and hence results in poor photovoltaic performance. Open-circuit voltage is more sensitive to the trapping time as compared to the short-circuit current. With an increase in the number of traps (shortening the trapping time), the photovoltage decreases. For trapping time $\tau_p = \tau_n < 1 \times 10^{-10}\,s$, the photocurrent also decreases significantly. The solar cell performance is also affected by the presence and distribution of ionic defects within the perovskite film. When the ions are distributed uniformly within the perovskite film, the cell performance is not affected much. In the presence of built-in and photogenerated electric fields, the ions start moving towards the charge transport layers. A drop in the J_{sc} and the output power is observed when the ions

start accumulating in various regions in the perovskite film. The solar cell performance is most affected when all the ions accumulate near the perovskite/ETL and perovskite/HTL interfaces. The ionic distribution and the photovoltaic performance can vary for different material parameters (choosing different material layers) and the solar cell architecture.

4 Role of cation-mediated recombination in JV hysteresis in perovskite solar cells

4.1 Background

Despite interface and grain boundary traps, the perovskite solar cells (PSCs) have achieved high power-conversion efficiency. However, efficiency is not the only measure in commercializing a solar cell technology. In PSCs, severe short- and long-term instabilities [91, 93] limit the long-term performance of PSCs. Moreover, the PSCs exhibit significant hysteresis in the current-voltage (JV) characteristics, which is strongly connected with device stability [94, 79, 95, 96]. Thus, a detailed understanding of charge carrier dynamics and the JV hysteresis is needed to make OIHPs truly exploitable in photovoltaic applications.

Charge transport and recombination processes in organic-inorganic hybrid perovskite (OIHP) devices are very complex. The physical mechanism behind the JV hysteresis of perovskite solar cells is still under debate. Several phenomena have been proposed as the physical origin of the hysteresis, including ferroelectric behavior of the perovskite on the nanoscale [157, 158], interfacial charge accumulation [159, 160], polarization at the perovskite/transport layer interface [161], very slow charge trapping and de-trapping [81, 162, 163], and slow ion/defect migration [77, 78, 96, 84, 80].

Ferroelectric contributions due to the arrangement of the dipolar organic CH_3NH_3 (MA) cations have been reported to contribute to the JV hysteresis in methylammonium lead iodide ($MAPbI_3$) perovskites [158]. However, frequency-dependent polarization [164], polarization and piezoresponse microscopy [165], and quasielastic neutron scattering measurements [166] have suggested that the ferroelectricity is unlikely to dominate the JV hysteresis behavior. Fan *et al.* showed that $MAPbI_3$ is not ferroelectric at room temperature due to the dynamic orientational disorder of the MA cations [165]. The hypothesis is supported by Meloni *et al.* [167] and Tress *et al.* [96], suggesting the JV hysteresis to originate due to thermally activated and slow field-induced process most likely related to ionic defects.

Within the scientific community, ion migration is widely accepted as the main reason for the JV hysteretic behavior of PSCs. The ionic migration has been visualized through wide-field photoluminescence imaging microscopy [168] and impedance spectroscopy [169]. Meloni *et al.* measured the activation energy for the hysteretic process and found a strong connection with activation energies for halide ion (vacancy) migration [167]. The ionic migration under the influence of the built-in and applied potential causes a slow redistribution of ions within the perovskite layer [96, 168, 170]. Furthermore, Xia *et al.* [171] demonstrated that in triple cation mixed-halide perovskite, strong photoinduced polarization can not lead to photovoltaic hysteresis, supporting ion migration to be the primary mechanism responsible for the JV hysteresis. Several other studies indicate

that halide ions lead to the JV hysteresis as they migrate through the perovskite layer and finally accumulate within narrow Debye layers near the perovskite/transport layer interfaces [84, 172, 80].

Moreover, several studies have found that the presence of trapping centers (recombination process) is needed to obtain a hysteretic behavior in JV characteristics [83, 82, 81, 75, 80]. Hysteresis-free JV profiles can be obtained by modeling without trap centers [87], suggesting that the trapping might play an important role in the JV hysteresis. The mechanism linking the ionic movements, the role of trapping mechanisms and the JV hysteresis is still unclear.

$MAPbI_3$ perovskite suffers thermal instabilities because of weak metal-halide (Pb-I) bonds [92, 173]. Furthermore, The $CH_3NH_3^+$ cations can rotate within their cages, as explained in chapter 1. These dynamic structural disorders lead to defect formation in the crystal structure [174]. The most commonly known defects are the ionic interstitial and vacancies. Buin *et al.* [175] and Yin *et al.* [174] reported the *n*-type iodine interstitials, I_i, *p*-type lead vacancies, V_{Pb}, and *n*-type methylammonium (MA) interstitial, MA_i to be the dominant defects in $MAPbI_3$. Another studies by Walsh *et al.* [176] and Eames *et al.* [77] found iodine vacancies to be the dominant ionic defects. First principle study by Azpiroz *et al.* [76] predicted that the iodine vacancies and interstitials can diffuse within the perovskite film. Azpiroz *et al.* [76] and Xiao *et al.* [177] demonstrated that, MA and Pb vacancies have lower activation energies and therefore lead to JV hysteresis. In $MAPbI_3$, space charge-limited current studies suggested shallow defects with low densities of $10^{11}\,cm^{-3}$ [178], while deep level spectroscopy predicted mid-gap defects of 10^{15}-$10^{16}\,cm^{-3}$ [179]. Mosconi *et al.* suggested the defect-migration in $MAPbI_3$ with a reorientation of nearby MA cations [180]. Furthermore, some studies suggested that point-like defects can trap the photogenerated charge carriers [181, 174, 182] probing performance losses due to trap-assisted recombination of the charge carriers.

Existing drift-diffusion (DD) studies do not capture the trapping nature of the mobile ions within PSCs. Sherkar *et al.* investigated the nature of ionic traps within grain boundaries [75]. They used a fixed trap density within one-dimensional simulations. Neukom *et al.* [111] and Courtier *et al.* [110] also modeled ion migration in presence of traps at fixed positions. Gagliardi *et al.* used fixed electrostatic potential to model ionic-distribution a within mesoporous TiO_2 transport layers [183]. Canil *et al.* [134] simulated the impact of ions defects by considering ionic accumulation near the perovskite/transport layer interfaces. Calado *et al.* developed a time-dependent DD model to study the role of migrating ions on the JV hysteresis [82]. In the latter model, trapping of charge carriers is neglected, and the ions are considered only to screen the built-in potential. To the best knowledge, for the first time, Domanski *et al.* presented DD calculations including the recombination of electrons at mobile anions to explain the transient behavior of the photocurrent [94].

This chapter investigates the connection between charge trapping and recombination at cations, in $MAPbI_3$ perovskite solar cells. The objective is to understand if the cation-assisted recombination of electrons-holes contributes to the JV hysteresis of the cell. The **Driftfusion** model by Calado *et al.* [184] is extended by implementing trap-assisted recombination of photogenerated charge carriers using cations as recombination/trap centers. Mobile cations are considered to act as mobile trap centers for the photoengrated electrons. The trapped electrons can then recombine non-radiatively with holes in the valence band. Herein, the JV hysteresis is calculated for different JV scan rates,

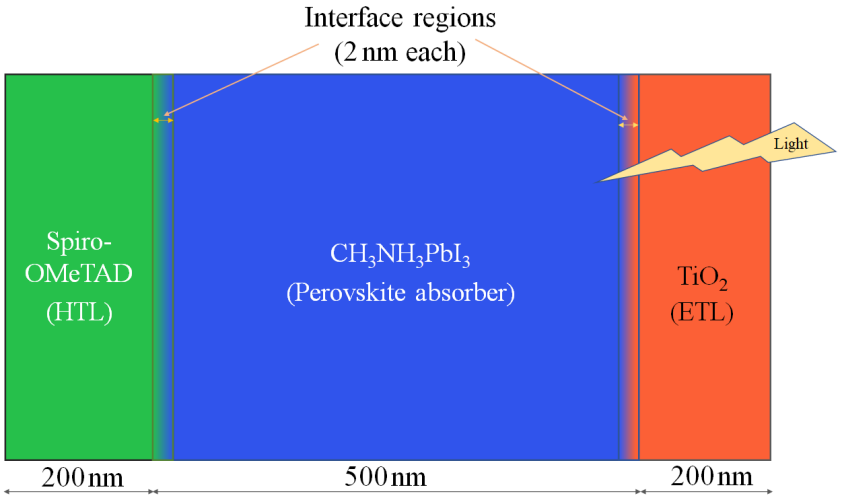

Figure 4.1: Perovskite solar cell device structure: A perovskite layer (blue region) is stacked between TiO_2 ETL and Spiro-OMeTAD HTL. 2 nm interface regions account for the interface properties within the drift-diffusion simulations.

cation-electron trapping constants, and cation energies. Including the cation-mediated recombination, increased performance losses, and a significant enhancement in the JV-hysteresis is observed. Even for shallow cations, additional losses in the open-circuit voltage and increased hysteresis arise. Furthermore, the impact of ionic mobilities on the JV hysteresis is studied. The JV hysteresis appears for a particular mobility range and disappears for very high and very low ionic mobilities. The presented study can stimulate a novel perspective on the role of ionic defects on lead-halide hybrid PSCs' performance.

4.2 Simulation model

A one-dimensional drift-diffusion model is developed by modifying **Driftfusion** model of Calado *et al.* [184] to simulate cation-mediated recombination. The model considers a perovskite solar cell with a 500 nm $MAPbI_3$ photoactive layer, a 200 nm TiO_2 electron transport layer (ETL) and a 200 nm Spiro-OMeTAD hole transport layer. Two buffers regions, each of 2 nm are defined at the ETL/perovskite and HTL/perovskite interfaces as shown in Figure 4.1. In the buffers, material properties such as the valence and conduction bands as well as the dielectric constant are gradually varied using an effective medium approach.

Transport of the charge carriers and the ions is governed by electrically induced drift and concentration-gradient induced diffusion. The full set of equations is given as follows:

$$\begin{cases} \nabla \cdot (\epsilon \nabla \Phi) = -q \left(n - p + N_{\mathrm{a}}^{-} - N_{\mathrm{d}}^{+} - N_{\mathrm{ct}} + N_{\mathrm{an}} + n_{\mathrm{t}}^{-} - n_{\mathrm{t}}^{+} \right) \\ \nabla \cdot \{ \mu_{\mathrm{n}} n \left(\nabla \Phi_{\mathrm{n}} \right) \} = G - R_{\mathrm{dir}} - R_{\mathrm{SRH}} - R_{\mathrm{c\text{-}e}} \\ \nabla \cdot \{ \mu_{\mathrm{p}} p \left(\nabla \Phi_{\mathrm{p}} \right) \} = G - R_{\mathrm{dir}} - R_{\mathrm{SRH}} - R_{\mathrm{c\text{-}e}} \\ \nabla \cdot \left\{ \mu_{\mathrm{ct}} N_{\mathrm{ct}} \left(k_{\mathrm{B}} T \frac{\partial N_{\mathrm{ct}}}{\partial x} \right) \right\} = 0 \\ \nabla \cdot \left\{ \mu_{\mathrm{an}} N_{\mathrm{an}} \left(k_{\mathrm{B}} T \frac{\partial N_{\mathrm{an}}}{\partial x} \right) \right\} = 0 \end{cases} \tag{4.1}$$

The first equation is the Poisson equation consisting of all possible charges. The last four equations are the continuity equations for the electrons, holes, cations and anions, respectively. n and p, N_{ct} and N_{an} represent the electron, hole, cation and anion densities, respectively. ϵ, Φ, and q represent the material permittivity, electrostatic potential and the elementary charge, respectively. N_a^- and N_d^+ are the ionized acceptor and ionized donor densities, respectively. μ_{n}, μ_{p}, μ_{ct} and μ_{an} represent the electron, hole, cation and anion mobilities, respectively. n_{t}^- and n_{t}^+ are electron and hole trap densities, respectively. The electrochemical potentials of electrons and the holes are represente by Φ_{n} and Φ_{p}, respectively. Direct (bimolecular) recombination of electrons and holes is governed by equation 2.3. Non-radiative trap-assisted recombination of the electrons and holes is governed by Shockley-Read-Hall (SRH) recombination rate defined in equation 3.3.

In contrast to the previous works [82, 75, 109, 87], this study includes the recombination of photogenerated charge carriers mediated by the moving cations. This process is defined as similar to the SRH recombination, considering the cations as trapping centers for electrons. In contrast to the standard trap states, these cations can migrate within the perovskite layer layer. The cation-mediated recombination rate, $R_{\text{c-e}}$ is defined as:

$$R_{\text{c-e}} = \frac{np - n_i^2}{\left(n + N_{\mathrm{c}} \exp\left(\frac{E_{\mathrm{ct}} - E_{\mathrm{c}}}{k_{\mathrm{B}} T}\right)\right) \frac{1}{N_{\mathrm{ct}} C_{\mathrm{cn}}}} \quad , \tag{4.2}$$

where E_{ct} is the cation energy level mediating the recombination process. E_{c} is the conduction band energy. C_{cn} represents the electron-capturing constant by a cation.

The photogeneration (G) of charge carriers is governed by a Lambert-Beer model defined in equation 2.2. The absorption coefficient $\alpha(\lambda)$ at wavelength λ is calculated by using the imaginary part of refractive index, κ as defined in equation 3.2. κ value are taken from ref. [146]. The AM 1.5 standard spectrum between 300 nm and 800 nm is used to calculate the optical generation of charge carriers.

A JV scan is applied as follows: First, an equilibrated solution at short-circuit condition is obtained for the dark condition. Then, light is switched on, and the steady-state equilibrium is calculated. At this steady-state, the voltage is applied with a constant scan rate until reaching the open-circuit voltage. Then, the voltage sweep direction is reversed (the voltage decreases with the same scan rate), and the simulation is done to obtain a short-circuit condition. For each voltage point, the net current is calculated. By using the JV sweeps, the photovoltaic performance parameters are compared for the different cases where ions lead to the electrostatic screening only (do not act as trap centers), and when the ions act as trap centers to mediate the recombination process. The parameters used for the drift-diffusion simulations are summarized in table 4.1.

4.3 Results and discussion

4.3.1 Cation-mediated recombination

To study the impact of ion mediated recombination, the JV characteristics of a 'neat' device without any ions, is compared with two devices with an ion density of $10^{18}\,\mathrm{cm}^{-3}$ [186]. To maintain the charge neutrality, equal densities are considered for both the cations and anions. The voltage sweep rate is fixed at $250\,\mathrm{mV\,s}^{-1}$. For the devices with ions, the JV characteristics are calculated without and with cation-mediated recombination. Futscher

Table 4.1: List of parameters used in drift-diffusion simulations. The parameters marked with the asterisks(*) are varied during the simulations. Reproduced with permission from ref [185].

Perovskite parameters	Value	Units	Ref.
Valence band maximum	-5.43	eV	[147]
Conduction band minimum	-3.88	eV	[147]
Electron and hole mobility	5	$\mathrm{cm^2/(V\,s)}$	[15]
Relative permittivity ϵ_r	24.1	-	[122]
Cation and anion density	10^{18}	$\mathrm{cm^{-3}}$	*
Cation mobility	10^{-12}	$\mathrm{cm^2/(V\,s)}$	*
Anion mobility	10^{-9}	$\mathrm{cm^2/(V\,s)}$	*
Bimolecular recombination rate	1×10^{-12}	$\mathrm{cm^{-3}\,s^{-1}}$	[103]
τ_n and τ_p at interfaces	5×10^{-10}	s	[103]
τ_n and τ_p in bulk perovskite	1×10^{-7}	s	[103]
Spiro-OMeTAD parameters	Value	Units	Ref.
HOMO energy	-5.22	eV	[150]
LUMO energy	-2.05	eV	[150]
Relative permittivity ϵ_r	3	-	[151]
p-type doping	1×10^{18}	$\mathrm{cm^{-3}}$	[183]
Hole mobility in Spiro-OMeTAD	0.01	$\mathrm{cm^2/(V\,s)}$	[152]
TiO_2 parameters	Value	Units	Ref.
Bandgap	3.2	eV	[148]
Conduction band minimum	-4	eV	[148]
Relative permittivity ϵ_r	85	-	[149]
Electron mobility	0.02	$\mathrm{cm^2/(V\,s)}$	[148]
Contact parameters	Value	Units	Ref.
Anode Fermi level	-4.2	eV	fit
Cathode Fermi level	-5.1	eV	[153]

et al. observed three orders of magnitude difference in the diffusion coefficient between I^- and MA^+ ions [155]. Calado *et al.* [82] used an ionic mobility of $10^{-12}\,\mathrm{cm^2\,V^{-1}\,s^{-1}}$ in their DD analysis. Combining the mentioned references [82, 155], ion mobilities of $\mu_\mathrm{an} = 10^{-9}\,\mathrm{cm^2\,V^{-1}\,s^{-1}}$ and $\mu_\mathrm{ct} = 10^{-12}\,\mathrm{cm^2\,V^{-1}\,s^{-1}}$ are used in this study. All other parameters are taken from Table 4.1. The hysteresis index (HI) is calculated from the power conversion efficiency (PCE) during forward and reverse sweep [187], as following:

$$\text{Hysteresis Index (HI)} = \frac{\text{PCE(reverse)} - \text{PCE(forward)}}{\text{PCE(reverse)}}\,. \tag{4.3}$$

Figure 4.2 shows the calculated JV characteristics in the forward (dashed line) and backward (solid line) direction. For the neat device (without ionic defects), a short-circuit current density (J_sc) of $21.1\,\mathrm{mA\,cm^{-2}}$ and an open-circuit voltage (V_oc) of $1.05\,\mathrm{V}$ are obtained. With a fill-factor (FF) of 0.79 the device shows a power conversion efficiency (PCE) of 17.5 %. It is observed that the JV-curves in forward and backward directions for the neat device overlap and no hysteresis is observed. Introducing an ion density of $10^{18}\,\mathrm{cm^{-3}}$ leads to hysteresis in the JV characteristics with an HI value of 0.009. The V_oc remains unchanged, while the J_sc slightly decreases to $20.7\,\mathrm{mA\,cm^{-2}}$. A small decrease in fill-factor to 0.76 is observed. As a result, the PCE drops to 16.5 %. Despite the large

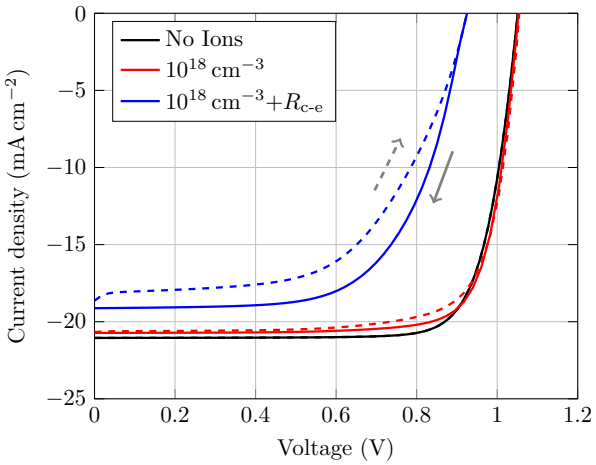

Figure 4.2: Current-voltage (JV) characteristics of $MAPbI_3$ devices with different ionic properties. The black curve shows the JV without ions. Red and blue curves show simulated JV profiles with an ion density of $10^{18}\,\mathrm{cm}^{-3}$ for both the anions and cations. The blue curve shows JV-characteristics after including cation mediated recombination of charge carriers. Dashed and solid lines show the current density in forward and backward sweep direction, respectively. The arrows denote the sweep direction. Reproduced with permission from ref [185]. Copyright © 2020 Elsevier B.V.

ionic densities, this change in the device performance is rather small. Usually, much lower ionic densities ($2.5 \times 10^{16}\,\mathrm{cm}^{-3}$ to $1 \times 10^{17}\,\mathrm{cm}^{-3}$) are predicted by experimental techniques [188, 155]. Theoretical studies however propose high ionic densities (up to $10^{19}\,\mathrm{cm}^{-3}$) at grain boundaries or near the perovskite surface [75, 189, 190, 109, 84, 191]. To note that, so far, the ions were doing electrostatic screening only, and not trapping the charge carriers.

Now, the role of the cation mediated recombination is studied. In addition to the screening of the electric field, the ionic defects can localize and trap the charge carriers. This trapping of charge carriers will enhance the probability of non-radiative recombination. The simulations include this effect via a Shockley-Read-Hall type mechanism (equation 4.2) to mimics the electrons-trapping via cations and their subsequent recombination with holes. Note that only the cations lead to trap electrons, while the anions move freely without contributing to the trapping. The trap energy level of the cations (E_{ct}) is considered to be 0.2 eV below the perovskite conduction band. The capture coefficient is fixed at $10^{-8}\,\mathrm{cm}^3\,\mathrm{s}^{-1}$.

The blue lines in Fig. 4.2 show the JV characteristics with the cation mediated recombination for the ion densities of $10^{18}\,\mathrm{cm}^{-3}$. Clearly, a strong decrease in all the device parameters is observed. A J_{sc} of $19.1\,\mathrm{mA\,cm}^{-2}$ and a V_{oc} 0.93 V are obtained. Furthermore, a significant decrease in the FF (to 0.64) leads to a tremendous drop in the PCE to 11.3 %. Also, HI increases by one order of magnitude, from 0.009 to 0.095.

Conduction and valence band and Fermi energy levels are calculated to gain further insight into the recombination processes. Figure 4.3(a) shows the simulated energy levels. In the perovskite (white background) and the ETL (blue background) regions, the quasi-Fermi levels of both the electron and hole shift to lower values in the short-circuit compared to the open-circuit case. This represents the depletion of charge carrier in short-circuit operation. Interestingly, the quasi-Fermi level in the HTL region (green

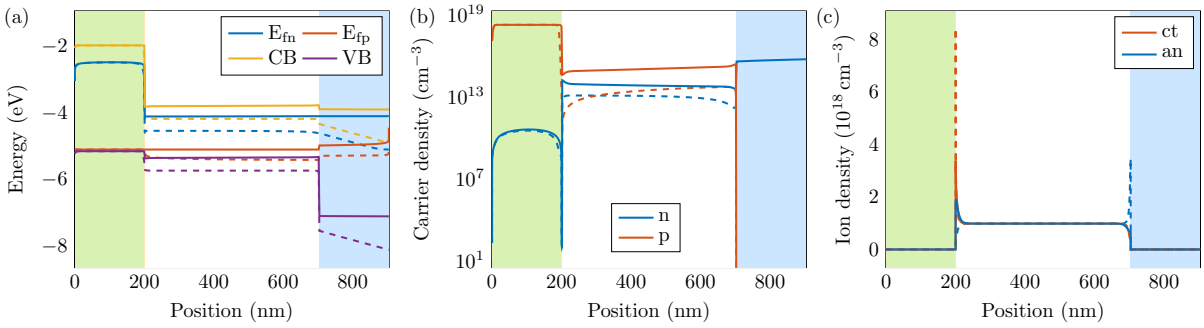

Figure 4.3: Simulated energy levels and charge and ion density profiles. (a) Conduction band energy (CB), valence band energy (VB), electron quasi-Fermi level (E_{fn}) and hole quasi-Fermi level (E_{fp}) energies. (b) Electron (n) and hole (p) densities. (c) Cation (ct) and anion (an) densities. Dashed lines represent the properties at short-circuit conduction, solid lines correspond to open-circuit voltage case after the forward sweep. Light green, white and light blue regions represent HTL, perovskite and ETL, respectively. Reproduced with permission from ref [185]. Copyright © 2020 Elsevier B.V.

background) remains the same for short-circuit and open-circuit conditions. This suggests that, at the short circuit, depletion of charges near the perovskite/HTL interface is compensated by the electrostatic potential developed due to the cation accumulation. Figure 4.3(b) and Figure 4.3(c) show the charge and ionic density profiles. The simulation results are roughly identical for the simulations without and with cation-mediated recombination. At short-circuit condition (dashed lines), the ions accumulate at opposite interfaces between the perovskite and the transport layers, leading to a strong electric field. In bulk perovskite, both the cations and anions densities remain roughly similar and constant at $10^{18}\,cm^{-3}$. During the forward sweep, anions move through the perovskite layer and accumulate near the perovskite/HTL interface. In contrast, the change in the distribution of the cations is less significant due to their lower mobility. The voltage sweep is too fast for a redistribution of cations. The magnitude of the cations at the HTL interface is reduced by roughly a factor of 2. This leads to a broadening of the accumulation layer of the cations near the HTL. At the ETL, no significant cation density is observed.

4.3.2 Cation energy

The energy level of trap states plays an important role in the trapping, de-trapping, and recombination of charge carriers. If the energy level of trap states reside within the bandgap, trapping results in efficient trap-assisted recombination. However, if traps reside above the conduction band (CB) or below the valence band (VB) edges, trapped charge carriers can easily escape to become free carriers. Iodine vacancies (V_I), methylammonium interstitial (MA_i), and lead interstitial (Pb_i) have been reported to be the possible cations with energy levels within the bandgap of $MAPbI_3$ perovskite [182, 192, 181, 174]. However, the energy alignment of the cations may change depending on the environment of the defect, e.g., iodine-poor or iodine-rich [182].

Here, the role of the cation energy on the device performance is investigated. The capture coefficient and the ion density are fixed to $10^{-8}\,cm^3\,s^{-1}$ and $10^{18}\,cm^{-3}$, respectively. A fixed voltage scan (sweep) rate of $250\,mV\,s^{-1}$ is employed to calculate the JV charac-

teristics. Figure 4.4 shows the JV characteristics for cation energies varying from 0 eV to 0.3 eV (below the perovskite conduction band edge). The black curves show the JV curves without cation-mediated recombination as a reference. The device performance parameters are summarized in Table 4.2, including $E_{ct} = 0.4$ eV and 0.5 eV (not shown in Fig. 4.4). For $E_{ct} = 0$ eV, a slight reduction in the V_{oc} by 10 meV is observed due to enhanced recombination. The HI and the other photovoltaic parameters do not change. For the cation energies 0.1 eV below the perovskite conduction band, significant changes in the JV-characteristics are observed. The main change is observed in the open-circuit voltage which decreases from 1.05 V to 0.99 V. In addition, the FF is reduced to 0.73(0.78) in forward(backward) direction. The HI doubles to 0.02. For deeper cation energies, the device performance is heavily deteriorated. For $E_{ct} \geq 0.3$ eV, the short-circuit current densities drop below 10 mA cm^{-2}. The open-circuit voltage is continuously shifted towards lower values due to the enhanced recombination losses mediated by the cations. Also, the HI increases to a very high value of 0.26 at $E_{ct} = 0.5$ eV.

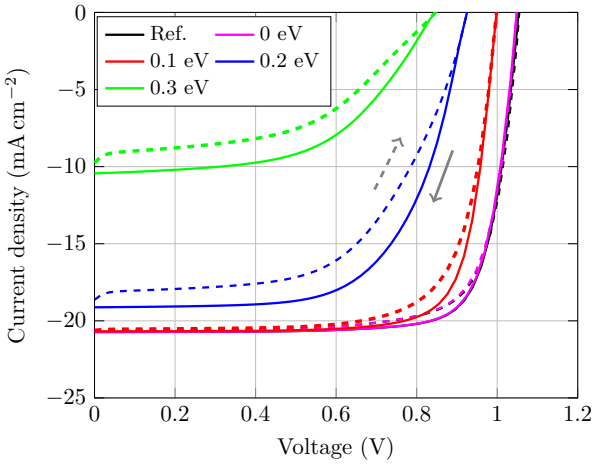

Figure 4.4: JV-characteristics of the $MAPbI_3$ devices with different cation energies. The cation energy is the energy level with respect to the conduction band minimum. The black curve shows the JV-characteristics without cation mediated recombination. Dashed and solid lines show the current density in forward and backward sweep direction, respectively. The arrows denote the sweep direction. Reproduced with permission from ref [185]. Copyright © 2020 Elsevier B.V.

Usually, literature refers to defect energies of 0.1 eV to 0.2 eV as shallow defects. As a result, the role of such defects in device performance is usually ignored. Especially when considering grain boundaries or interfaces between the perovskite and the HTL, ion densities of 1×10^{18} cm^{-3} are reasonable [193]. It is known from the experiments that the shallow traps can trap the charge carriers, resulting in trap filling. The trap filling process can contribute to the capacitive currents, and hence the JV hysteresis [81, 194]. Photoluminescence studies point out that the transition between various ionic defect states (most likely within the bandgap) can be related to the JV hysteresis [195]. Therefore, it is likely that the electron-trapping by the shallow cation is responsible for the JV hysteresis.

Deep cation defects cause a tremendous loss of efficiency and induce large JV hysteresis. From the obtained simulation results, deep cation states can be ruled out. Cation states need to be close to the perovskite conduction band to justify the high efficiencies observed for PSCs. The results support the hypothesis that shallow cation traps (i.e. V_I) are

Table 4.2: Photovoltaic performance parameters in forward (backward) direction for different cation energies E_{ct}. The open-circuit voltage is equal for both the forward and backward direction. Reproduced with permission from ref [185]. Copyright © 2020 Elsevier B.V.

E_{ct}	V_{oc} (V)	j_{sc} (mA cm^{-2})	FF (-)	PCE (%)	HI
Ref.	1.06	20.7(20.7)	0.77(0.79)	16.8(17.3)	0.01
0	1.05	20.7(20.7)	0.76(0.79)	16.5(17.1)	0.01
0.1	0.99	20.6(20.7)	0.73(0.78)	14.9 (15.9)	0.02
0.2	0.93	18.6(19.1)	0.57(0.64)	9.9 (11.4)	0.10
0.3	0.85	9.7(10.4)	0.47(0.54)	3.9 (4.8)	0.17
0.4	0.76	3.5(4.0)	0.40(0.47)	1.1(1.4)	0.20
0.5	0.62	1.2(1.3)	0.39(0.48)	0.3(0.4)	0.26

responsible for electron-trapping [196, 197, 192, 198, 199], and hence the enhanced JV hysteresis.

4.3.3 Voltage scan rate

The JV hysteresis in PSCs is connected to the motion of slow ions within the perovskite layer. Here, the role of the voltage scan rate on the hysteresis is studied in the presence of cation-mediated recombination. The cation energy is fixed at 0.1 eV below the conduction band. The capture coefficient and the ion density are fixed at $10^{-8}\,\mathrm{cm^3\,s^{-1}}$ and $10^{18}\,\mathrm{cm^{-3}}$, respectively. The voltage scan rate is varied from $10\,\mathrm{mV\,s^{-1}}$ to $10\,\mathrm{V\,s^{-1}}$.

Figure 4.5(a) and (b) show the JV-characteristics without and with the cation-mediated recombination, respectively. In both cases, a negligible hysteresis for voltage scan rates below $100\,\mathrm{mV\,s^{-1}}$ is observed. In this regime, ions can easily follow the change in the applied bias voltage. This reduces the role of the scanning direction of the bias voltage on the current densities. For higher voltage scan rates, a significant hysteresis arises. Anions ($\mu_{\mathrm{an}} = 10^{-9}\,\mathrm{cm^2\,V^{-1}\,s^{-1}}$) migrate and accumulate near the perovskite/HTL interface. The mobility of cations ($10^{-12}\,\mathrm{cm^2\,V^{-1}\,s^{-1}}$), however, is too low to follow the change in the applied bias voltage. On the other hand, at higher voltage scan rates, the hysteresis is expected to vanish again as neither of the ions can follow the change in the applied voltage [96].

Now, the extracted JV hysteresis (index) is compared for two different ionic models. In one of the models, the cation-mediated recombination is neglected, and the ions lead to electrostatic screening only. In the other model, along with the electrostatic screening, the cation-mediated recombination is activated. The calculated HIs are summarized in Table 4.3. When the cation-mediated recombination is neglected, a negligible hysteresis of HI $= 6 \times 10^{-4}$ is observed for slow scan rates of $10\,\mathrm{mV\,s^{-1}}$. Upon inclusion of cation-mediated recombination, the HI increases to 2.5×10^{-3}. For all investigated voltage scan rates, the simulated HI with cation-mediated recombination ($R_{\text{c-e}} > 0$) is significantly higher than for $R_{\text{c-e}} = 0$. Furthermore, the J_{sc} and the V_{oc} remains roughly the same for all the scan rates. For very high scan rate (i.e.,$10\,\mathrm{V\,s^{-1}}$), a strong S-shape is observed in the JV characteristics. This is mainly attributed to the screening of the built-in field due to the accumulation of ions at the interface between the perovskite and the transport layers [200, 96]. For scan rates of $\geq 500\,\mathrm{V\,s^{-1}}$ (not shown here), the hysteresis vanishes while a strong S-shape is observed. At such high scan rates, the ions cannot follow the

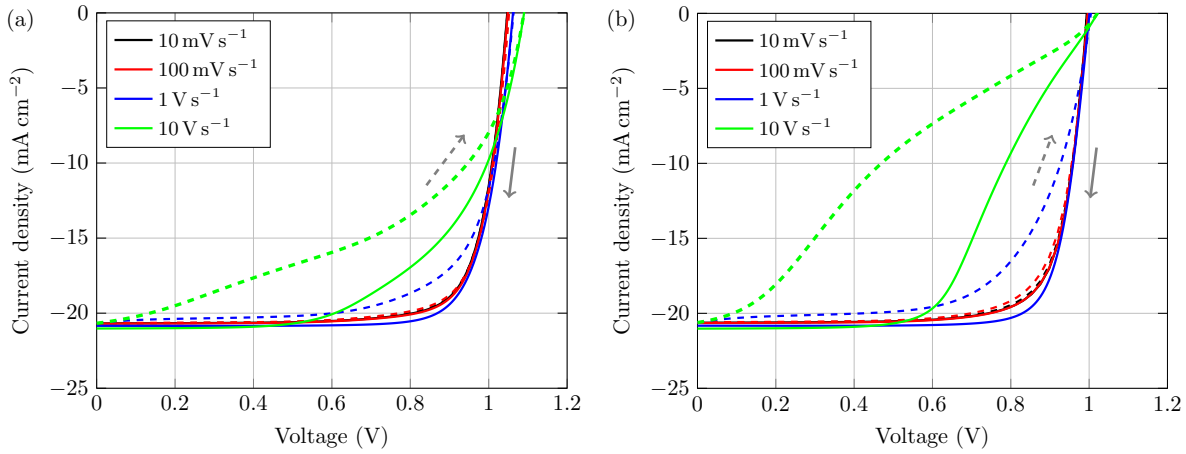

Figure 4.5: JV-characteristics of the $MAPbI_3$ device with varying voltage scan rate for two different ion models: In (a), the cation-mediated recombination is neglected and only electrostatic screening of ions is considered. (b) The JV-curves accounting for the cation-mediated non-radiative electron-hole recombination. Dashed and solid lines show the current density in forward and backward sweep direction, respectively. The arrows denote the sweep direction. Reproduced with permission from ref [185]. Copyright © 2020 Elsevier B.V.

change in the applied voltage, which leads to a negligible change in the current values [96].

Table 4.3: Calculated hysteresis index (HI) without ($R_{\text{c-e}} = 0$) and with ($R_{\text{c-e}} \neq 0$) cation-mediated recombination. Reproduced with permission from ref [185]. Copyright © 2020 Elsevier B.V.

Scan Rate (V s^{-1})	HI($R_{\text{c-e}} = 0$)	HI($R_{\text{c-e}} \neq 0$)
0.01	0.0006	0.0025
0.1	0.0027	0.0099
1	0.0480	0.0859
10	0.1449	0.3633

Dynamic measures such as the voltage scan of the JV characteristics and impedance spectroscopy or deep-level transient spectroscopy can provide further insight into the dynamics of photogenerated charge carriers & ionic defects, and their interactions. DD calculations allow the extraction of parameters of the dynamics and the charge-ionic interaction by fitting experimental data. Existing time-dependent DD studies, however, fail to include the interactions between mobile ions and charge carriers, i.e., cation-mediated recombination. This can lead to a significant overestimation of ion densities. Considering the interaction of ionic defects with charge carriers within time-dependent DD will be useful as an additional tool to probe properties such as the capture coefficient or the defect energy levels.

4.3.4 Role of the capture coefficient

This section investigates the role of the capture coefficient C_{cn} on the JV hysteresis. Higher value of the capture coefficient results in more electron capture by the cations,

and subsequently higher recombination rate ($R_{\text{c-e}}$). A recent study by Zhang *et al.* showed that iodine interstitial are the dominant non-radiative recombination center [201], with room temperature capture coefficients ranging between $10^{-9}\,\text{cm}^3\,\text{s}^{-1}$ and $10^{-7}\,\text{cm}^3\,\text{s}^{-1}$. To investigate further, here, the capture coefficient is varied between $10^{-10}\,\text{cm}^3\,\text{s}^{-1}$ and $10^{-7}\,\text{cm}^3\,\text{s}^{-1}$. The voltage scan rate and the ion density are fixed to $250\,\text{mV}\,\text{s}^{-1}$ and $10^{18}\,\text{cm}^{-3}$, respectively. The energy of cations is taken as 0.2 eV below the perovskite conduction band edge.

Figure 4.6 shows the JV characteristics for the different capture coefficients. Table 4.4 summarizes the performance values for the forward and backward voltage scans, as well as the extracted HI. For capture coefficient below $10^{-10}\,\text{cm}^3\,\text{s}^{-1}$, the same JV characteristics is observed as if there was no cation mediated recombination. Increasing the capture coefficient up to $10^{-9}\,\text{cm}^3\,\text{s}^{-1}$, the main change observed in the JV characteristics is a reduced open-circuit voltage from 1.06 V to 0.97 V. The J_{sc} remains roughly unchanged. The hysteresis slightly increases leading to change in HI from 0.01 to 0.04. The change in the voltage and the FF leads to a detoriorate the reverse bias PCE from 17.3% to 14.7%. For larger C_{cn} beyond $10^{-9}\,\text{cm}^3\,\text{s}^{-1}$, a significant reduction in the J_{sc}, V_{oc} and the fill-factor is observed. For $C_{\text{cn}} = 10^{-7}\,\text{cm}^3\,\text{s}^{-1}$, the reverse (forward) bias PCE drops to 7.3% (5.9%).

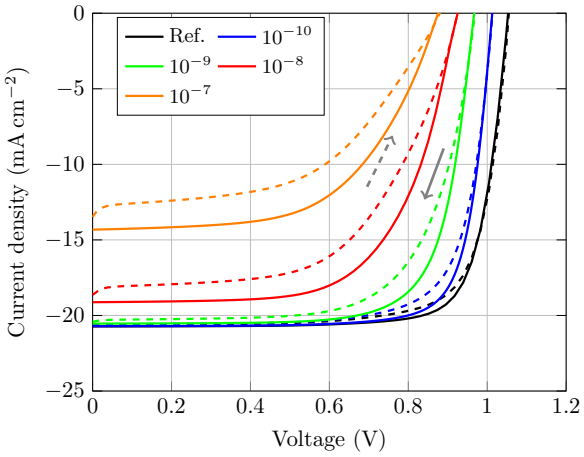

Figure 4.6: JV-characteristics of the $MAPbI_3$ devices with different electron capture coefficients (in units $\text{cm}^3\,\text{s}^{-1}$). The black curve shows the JV-characteristics without cation-mediated recombination. Dashed and solid lines show the current density in forward and backward sweep direction, respectively. The arrows denote the sweep direction. Reproduced with permission from ref. [185]. Copyright © 2020 Elsevier B.V.

These C_{cn} values are in the range of interstitial capture coefficients, predicted from first-principles study [201] and previous DD simulations [75, 144]. However, accurate values need to be obtained experimentally as defect properties and their densities strongly depend on the fabrication scheme and the perovskite materials. Moreover, the impact of the defects can be sensitive to the device architecture.

The obtained results highlight the need to understand the interactions between charge carriers and ionic defects. Experimental access of such properties is difficult, as many properties of PSCs are hidden under the dominant losses due to the perovskite/HTL and/or perovskite/ETL interfaces. First-principle analysis, in conjunction with DD study,

Table 4.4: Photovoltaic performance parameters in forward (backward) direction for different capture coefficients C_{cn} (in units cm^3/s). The open-circuit voltage is equal for both the forward and backward direction. Reproduced with permission from ref. [185]. Copyright © 2020 Elsevier B.V.

C_{cn}	V_{oc} (V)	j_{sc} ($\mathrm{mA/cm^2}$)	FF (-)	PCE (%)	HI
Ref.	1.06	20.7(20.7)	0.77(0.79)	16.8(17.3)	0.01
10^{-10}	1.01	20.6(20.7)	0.75(0.79)	15.6(16.5)	0.02
10^{-9}	0.97	20.4(20.5)	0.68(0.74)	13.5(14.7)	0.04
10^{-8}	0.93	18.6(19.1)	0.57(0.64)	9.9(11.4)	0.10
10^{-7}	0.88	13.5(14.3)	0.50(0.58)	5.9(7.3)	0.16

may further help to understand the nature of energy losses in PSCs and to enhance device stability and efficiency.

4.3.5 Role of ionic mobility

The mobility of ionic defects plays an important role in the JV characteristics of PSCs. This final section investigates the impact of the anion and cation mobilities on the JV-characteristics and its hysteresis. The capture coefficient value is fixed at $10^{-7}\,\mathrm{cm^3\,s^{-1}}$ to induce high electron capturing. Cation energy is fixed at 0.1 eV below the perovskite conduction band edge. Equal ionic density of $10^{18}\,\mathrm{cm^{-3}}$ is considered for both the cations and the anions. A fixed voltage scan rate of $250\,\mathrm{mV\,s^{-1}}$ is employed to calculated the JV characteristics. Figure 4.7a shows JV curves when both the $\mu_a = \mu_c$ are varied simultaneously. Initially, $\mu_a = \mu_c = 10^{-8}\,\mathrm{cm^2\,V^{-1}\,s^{-1}}$ is used to obtain the forward in reverse bias JV curves. At this high mobility, both the anions and the cations move too fast, and hence a negligible JV hysteresis (HI = 0.0005) is obtained. The J_{sc} remains the same for the forward ($20.1\,\mathrm{mA\,cm^{-2}}$) and reverse ($20.2\,\mathrm{mA\,cm^{-2}}$) bias. However, a low $V_{\mathrm{oc}} = 0.94\,\mathrm{V}$ (as compared to a 'neat' device) which is be attributed to the electron capturing by the cation.

While varying the ionic mobility from $1 \times 10^{-11}\,\mathrm{cm^2\,V^{-1}\,s^{-1}}$ and $1 \times 10^{-8}\,\mathrm{cm^2\,V^{-1}\,s^{-1}}$, the change in V_{oc} (0.93 V to 0.97 V) and J_{sc} ($20.1\,\mathrm{mA\,cm^{-2}}$ to $21.0\,\mathrm{mA\,cm^{-2}}$) is rather small. A small change in J_{sc} could be due to the change in the interface energetics. For low ionic mobilities, after a voltage sweep, the density of ions at the interface to the perovskite and HTL/ETL reduces. Thus, charge carriers see a reduced barrier to be transported to the charge transport layers. This reduction in barrier helps the charge carriers to escape before they recombine at the interface traps, and hence a slight increase in the J_{sc} is observed.

The main changes are observed in the HI and the FF, and hence, in the efficiency. The JV hysteresis increases with decreasing ionic mobilities which is in-line with existing studies [84, 94, 96, 169, 155]. For the ionic mobilities of $10^{-11}\,\mathrm{cm^2\,V^{-1}\,s^{-1}}$, the device performance is significantly deteriorated. A very high hysteresis (HI = 0.5520) is observed with 'S' shape in the JV curves. Furthermore, due to a drastic decrease in FF in both the forward and reverse bias, the cell PCS drops to 2.3% and 9.3% in forward and reverse bias, respectively. Table 4.5 summarizes the photovoltaic performance parameters for the forward and backward scan directions.

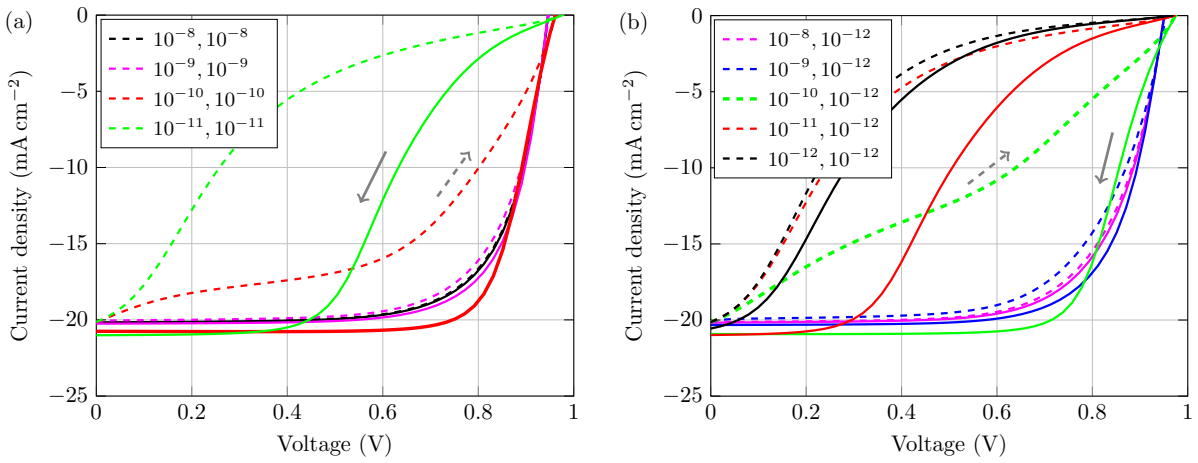

Figure 4.7: JV-characteristics of the $MAPbI_3$ devices with different ionic mobility $\mu = (\mu_a, \mu_c)$: (a) Varying both anion and cation mobility, (b) varying anion mobility while keeping cation mobility fixed at $1 \times 10^{-12}\,cm^2\,V^{-1}\,s^{-1}$. Mobility units are in $cm^2\,V^{-1}\,s^{-1}$. Dashed and solid lines show the current density in forward and backward sweep direction, respectively. The arrows denote the sweep direction. Reproduced with permission from ref. [185]. Copyright © 2020 Elsevier B.V.

Figure 4.7(b) shows calculated JV profiles for various anion mobilities while keeping cation mobility fixed at $10^{-12}\,cm^2\,V^{-1}\,s^{-1}$. Here, the hysteresis decreases with increasing the anion mobility. For $\mu_a = \mu_c = 10^{-12}\,cm^2\,V^{-1}\,s^{-1}$, a big "S"-shape is observed along with high HI of 0.1655. Also, the fill-factor and the efficiency are significantly reduced as summarized in Table 4.5. Anion mobilities of $1 \times 10^{-8}\,cm^2\,V^{-1}\,s^{-1}$ to $1 \times 10^{-9}\,cm^2\,V^{-1}\,s^{-1}$, in combination with cation mobility of $1 \times 10^{-9}\,cm^2\,V^{-1}\,s^{-1}$ to $1 \times 10^{-12}\,cm^2\,V^{-1}\,s^{-1}$ result in HI values obtained experimentally (0.00 to 0.48) [202, 203, 204, 205]. Simulations of low mobilities for both the ions do not match the experimentally observed high efficiency and low JV hysteresis of state-of-art perovskite solar cells. Similarly, simulations of high mobilities for both the ions do not justify the significant HI observed in experimental studies.

4.4 Conclusion

In conclusion, the impact of cation-assisted recombination of photogenerated charge carriers within $MAPbI_3$ PSCs is studied. The results indicate that the moving cations can mediate electron-hole recombination leading to a significant JV hysteresis. Shallow cations of $\leq$0.1 eV, such as iodine vacancies, mainly lead to a slight increase in the hysteresis and a reduced open-circuit voltage. Deep-level traps, such as methylammonium interstitials, can trap electrons efficiently and lead to strong JV hysteresis. If the cation-mediated recombination is neglected, hysteresis remains low even at high ionic defect densities. Apart from the hysteretic effects, the cation-mediated recombination significantly limits the cell performance. Due to the additional non-radiative recombination, fewer charge carriers are collected at the transport layers, resulting in reduced output current. The JV hysteresis is very sensitive to the voltage scan rate. At slow voltage scan rates, the ions can follow the change in potential, resulting in less JV hysteresis. At higher voltage scan rates, the applied voltage can increase the accumulation of local

Table 4.5: Photovoltaic performance parameters in forward (backward) direction for different ionic mobilities, μ_a, and μ_c (in units $cm^2\,V^{-1}\,s^{-1}$). The open-circuit voltage is equal for both the forward and backward direction. Reproduced with permission from ref. [185]. Copyright © 2020 Elsevier B.V.

μ_a, μ_c	V_{oc} (V)	J_{sc} (mA/cm^2)	FF (-)	PCE (%)	HI
10^{-8}, 10^{-8}	0.95	20.1(20.2)	0.71(0.71)	13.5(13.6)	0.0005
10^{-9}, 10^{-9}	0.95	20.1(20.3)	0.69(0.73)	13.2(13.9)	0.0250
10^{-10}, 10^{-10}	0.93	20.1(20.7)	0.51(0.76)	9.8(15.1)	0.2106
10^{-11}, 10^{-11}	0.97	20.1(21.0)	0.13(0.45)	2.6(9.3)	0.5220
10^{-8}, 10^{-12}	0.95	20.1(20.2)	0.67(0.69)	12.9(13.2)	0.0071
10^{-9}, 10^{-10}	0.94	20.1(20.3)	0.67(0.73)	12.8(14.1)	0.04
10^{-9}, 10^{-12}	0.95	20.1(20.3)	0.71(0.71)	12.3(13.7)	0.0528
10^{-10}, 10^{-12}	0.97	20.1(20.9)	0.33(0.71)	6.5(14.4)	0.3615
10^{-11}, 10^{-12}	0.97	20.1(21)	0.13(0.32)	2.5(6.6)	0.4556
10^{-12}, 10^{-12}	0.96	20.1(20.6)	0.12(0.15)	2.3(3.0)	0.1655

charges near the perovskite/transport layer interface, resulting in increased JV hysteresis. The JV hysteresis increases with increasing the capture coefficients, as it increases the recombination rate. A poor PCE is observed for higher capture coefficients. The JV hysteresis also depends on the ionic mobilities. For a given capture coefficient, the JV hysteresis disappears for higher ionic mobility. For lower ionic mobilities, an "S" shape along with hysteresis is observed in the JV characteristics.

The presented study highlights the importance of cation-mediated recombination, which is left out in most existing studies. At the same time, the study provides an insight into the possible interaction of moving ions with charge carriers within PSCs. The presented results combined with experimental characterization of charge carrier dynamics and first-principle calculations can initiate new investigations in PSCs' device physics.

5 Efficiency analysis of all-perovskite two-terminal tandem solar cells

5.1 Background

A single-junction solar cell has the theoretical efficiency limit of about 31% [72]. To surpass the theoretical limit, it is needed to adopt multijunction technologies, like tandem solar cells. Tandem solar cells offer higher efficiencies than a single junction solar cell by utilizing the solar spectrum in better manner. A top cell with a wider-bandgap material uses the high energy part of the solar spectrum and transmits the lower energy part to the bottom cell consisting of a lower bandgap material. III-V and II-VI compounds based multijunction solar cells have already shown good efficiencies [206, 7, 5], but they are expensive due to costly single crystal (epitaxial) fabrication methods. Excellent optoelectronic properties of organic-inorganic hybrid perovskites (OIHPs) have enabled high power conversion efficiency of OIHPs based single-junction solar cells [207, 15, 136, 14, 5]. Most of OIHPs show high absorption for energies above and very low absorption at energies below the bandgap [29], making them a suitable choice for subcells of a tandem cell. Due to their high optical absorption (energies above the bandgap), the incident light can be absorbed by a thin layer of perovskite, i.e., $\simeq 1\,\mu m$ or even less. Furthermore, solution processibility makes OIHPs easy to integrate with existing solar cell technologies (i.e., Si, GaAs) as a subcell in a tandem solar cell [208, 105].

There have been efforts to develop perovskite/silicon tandem solar cells [209, 210, 211, 212, 213, 89], but the technology is still far from commercialization due to the cost-ineffectiveness. To achieve high efficiency and simultaneously reduce the solar-electricity cost per kWh, a cheaper thin-film based tandem solar cell technology is desired. Perovskite/organic tandem cells have been demonstrated with a potentially low-cost fabrication, but large open-circuit voltage loss in the organic cell limits the tandem cell efficiency [214, 215, 216].

OIHPs based all-perovskite tandem cells show a great promise due to the simple fabrication process and high potential efficiency [217, 218, 219, 88, 89, 220, 221, 222, 223]. To meet the absorption spectrum required for a tandem architecture, perovskite bandgap can be fine-tuned by compositional engineering [104, 33, 31, 32], which offers a great advantage in using OIHPs in a low bandgap bottom cell as well a wide bandgap top cell.

In a tandem solar cell, subcells can be connected electrically in parallel or a series connection. The configuration in which the subcells are connected plays an important role in the final performance of the tandem cell. When spectrally split subcells are connected electrically in parallel with voltage matched, the configuration is known as four-terminal (4T). This configuration does not require a current matching between the subcells; therefore, it can use almost any bandgap combinations [225]. In a 4T tandem cell, since each subcell is fabricated independently, it leads to additional cost and involves more optical losses. If the subcells are connected electrically in series, the configuration is known as

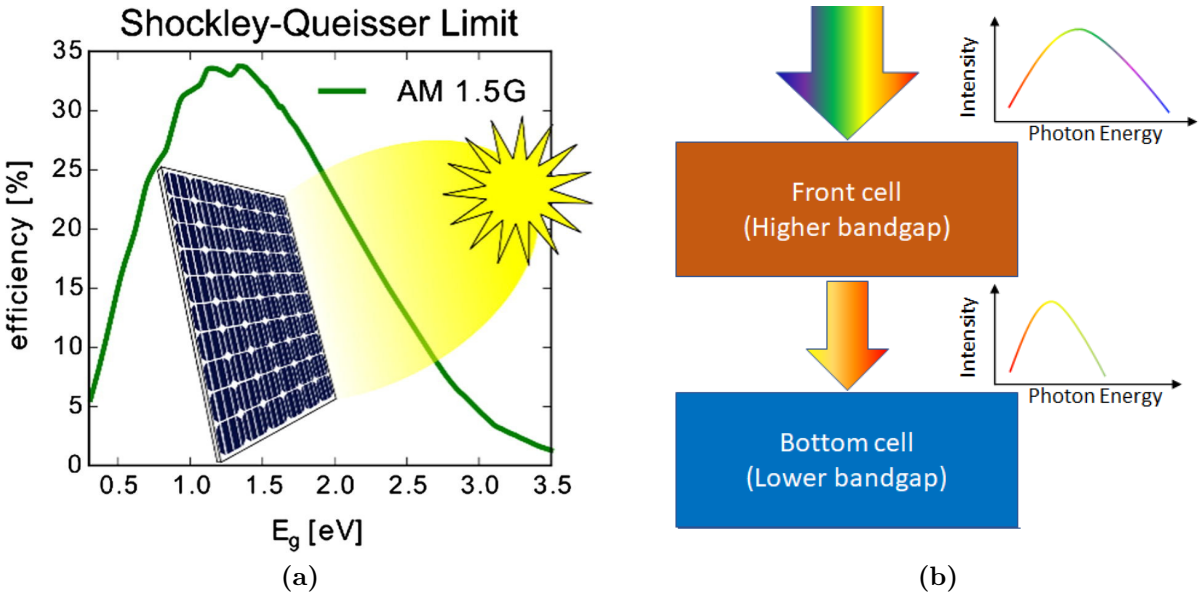

Figure 5.1: (a) Shockley–Queisser limit for efficiency of a single-junction solar cells. Reproduced with permission from ref. [72], copyright 2016 Elsevier Ltd. (b) Solar spectrum splitting scheme for a tandem solar cell. The figure is obtained from ref. [224].

Two-terminal (2T) tandem. Due to electrically series connection, a 2T tandem cell requires a current matching between the subcells. A 2T tandem cell's performance strongly depends on series-connected individual cells because the operating current is limited by the cell producing the lowest current [220]. Since the cell operates at "a lower current being transported at a higher voltage", it suffers less series resistance losses. Also, since the lateral current flow needs only two external contact layers, less number of heavily doped transport layers are needed for vertical charge transport [88]. With the latter, lower parasitic absorption and thus higher power conversion efficiencies could practically be realized. Furthermore, in a 2T configuration, the subcells can be monolithically integrated, it suffers less optical losses and enables similar module related costs as single-junction modules.

Some of the perovskite material combinations have already been used experimentally to demonstrate 2T perovskite tandem cells [217, 219, 220, 221, 222]. However, the efficiencies reported so far are still far away from the possible theoretical efficiency limit (42% for a 2T tandem device) [106]. There have not been many efforts to investigate the effect of various parameters and several loss mechanisms hampering tandem cells' performance. To improve the tandem cell efficiency, it is required to carefully optimize the electronic and optical characteristics of various layers and contacts. This optimization becomes even more crucial for two-terminal tandem cells because of the need for current matching between the subcells. To obtain the current matching and the light management within a 2T tandem cells, optimum bandgaps and thicknesses should be chosen for the top and bottom cells. Furthermore, to obtain maximum photocurrent and the photovoltage of 2T tandem cells, charge transport throughout the tandem device should be optimized. To ensure the best charge transport, the contact workfunctions and the band energies (and Fermi energies) of the charge transport layers must be optimized.

In the literature, numerical methods have been proposed to optimize design of all-perovskite p-i-n and all-perovskite tandem solar cells [226, 227, 228, 229] considering particular bandgap combinations of subcells (top and bottom cells). Zheng *et al.* [223] and Hörantner *et al.* [230] presented simulations to optimize top and bottom cell bandgaps in all-perovskite 2T tandem solar cells, without talking much about the role of various loss mechanisms and the contacts. Furthermore, there have not been studies on the role of charge carrier mobilities and doping in the charge transport layer in a 2T tandem architecture. This chapter presents a generalized simulation model to investigate the effect of material parameters such as mobility, trap density, and device parameters such as subcell bandgaps and thicknesses, and contact workfunction on the final performance of a 2T tandem solar cell. The role of doping of the charge transport layers is also studied. Finally, the optimization of top and bottom cell bandgaps and thicknesses and contact workfunctions is presented to realize the best performing all-perovskite 2T tandem solar cells.

5.2 Simulation model

TiberCAD implemented one-dimensional drift-diffusion simulation is adopted as explained in chapter 2. The drift-diffusion and Poisson equations are simultaneously solved for electrons, holes, and traps, accounting for electron-hole pair generation upon absorption of light in the bulk perovskite and the recombination processes. The drift-diffusion equations are solved for the top cell and the bottom cell independently. Two buffers of 2 nm each are defined on both sides of the perovskite layer, connected to the hole transport layer and the electron transport layer (see Figure 5.2a). The buffers account for the interface traps near the respective interfaces.

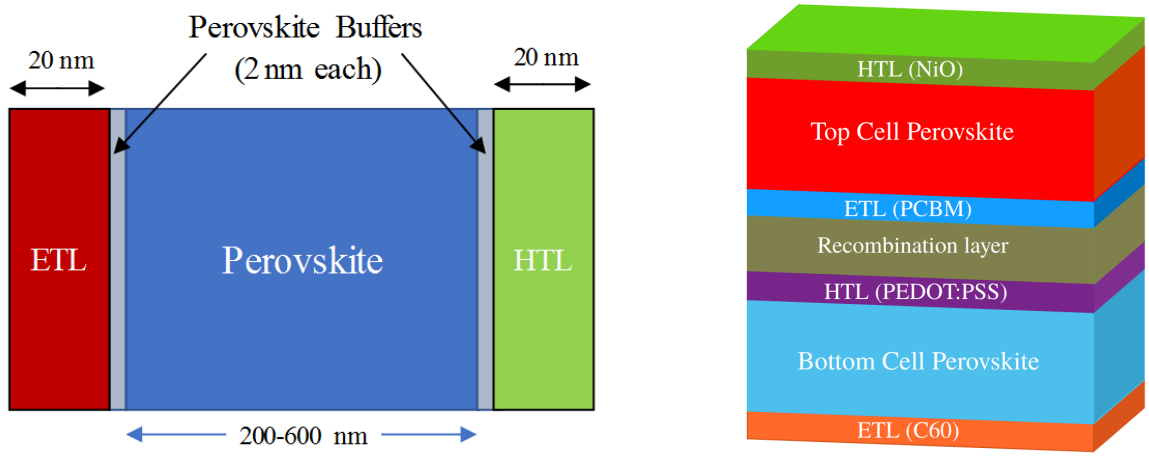

(a) (b)

Figure 5.2: (a) 1D simulation model of a perovskite solar cell, and (b) All-perovskite two terminal (2T) tandem solar cell representation. Reproduced with permission from ref. [101]. © 2019 International Solar Energy Society and Elsevier Ltd.

Generated electrons and holes in the perovskite are transferred to the electron and hole transport layers, respectively. Transport of these charges is governed by diffusion

and electrically induced drift, as described by equation 2.1. The perovskite films are assumed to be free of any ionic defects and/or fixed charges.

Generation of electron-hole pairs upon light absorption is governed by equation 2.2. The AM 1.5 standard spectrum between 350 nm and 2500 nm is used to calculate the optical generation. To calculate $\alpha(\lambda)$, direct bandgap nature of perovskie semiconductors is considered [27, 28]. Considering parabolic band approximation, optical absorption in a direct bandgap material is given by [145]:

$$\alpha(\lambda) = A^* \sqrt{\frac{hc}{\lambda} - E_g} \ , \tag{5.1}$$

where h is the Planck's constant, c is the light velocity in vacuum, E_g is the material bandgap, and A^* is given by the following:

$$A^* \approx q^2 \frac{\left(2\frac{m_e^* m_h^*}{m_e^* + m_h^*}\right)^{\frac{3}{2}}}{n_r c h^2 m_e^*} \ , \tag{5.2}$$

where, m_e^* and m_h^* are the effective masses of electron and hole, respectively, and n_r is the (real) refractive index. From equation 5.2, it is clear that the only variables here are the effective masses. Assuming the effective masses of the electron and the hole remain almost constant, A^* can be considered to be a constant; hence α shows a square root dependence on the energy of the incident photon of wavelength λ. For the simulations in this study, $A^* = 18\,\mathrm{cm^{-1}}\sqrt{\mathrm{eV}}$ is considered as a fitting parameter. The parameters used for the drift-diffusion simulations are summarized in Table 5.1. The mobilities of the ETL and HTL have been taken as fitting parameters ensuring the tandem cell is not limited by the charge transport in the collection layers. To account for the charge selectivity, the hole mobility in ETL is considered to be 5 orders of magnitude smaller compared to the electron mobility. Similarly, the electron mobility in the HTL is considered to be 5 orders of magnitude smaller compared to the hole mobility. Cathode and anode energy levels have been chosen based on the workfunction of the typically available contact metals, such as, gold, aluminium, copper, and silver, etc. Considering the ambipolar nature of the hybrid perovskites [15, 222], same electron and hole mobility value ($5\,\mathrm{cm^2/(V\,s)}$) has been chosen for the perovskite layer.

Two types of recombination processes are considered in the perovskite and the buffer regions. First, direct (radiative) recombination given by equation 2.3. The second, to include the effect of traps, is a Shockley-Read-Hall recombination rate defined by equation 3.3.

As mentioned earlier, since the top and bottom cells are simulated independently, the effect of the recombination layer is ignored. Two terminal (2T) configuration is similar to two cells connected in series. To achieve the optical coupling, the amount of light filtered by the top cell is considered as the input for the bottom cell. Since the charge carriers injected from the high current cell recombine in the low current cell, for an ideal system, the output current will be the minimum of the two cell currents. For this reason, for a 2T tandem cell, the total output current is considered to be the minimum current of the two subcells. On the other hand, like series-connected voltage sources, the output voltage comes to be the sum of the voltages from the two subcells. For the scope of this study, it is assumed that the ETL, HTL, and the typically used combining layer (combining the top and bottom cells, such as TiO_2) are ideal and do not consist of optical losses. The

Table 5.1: List of parameters used in the drift-diffusion simulations. Values of the parameters marked with asterisks(*) are varied during the simulation. Reproduced with permission from ref. [101]. © 2019 International Solar Energy Society and Elsevier Ltd.

Parameter	Value	Unit	Ref.
Electron and hole mobility in Perovskite	5	cm^2/Vs	*
Perovskite relative permittivity	20	-	-
PCBM bandgap	1.8	eV	[125]
PCBM LUMO	-5.9	eV	[124]
Electron mobility in PCBM and C_{60}	1	cm^2/Vs	[231]
Hole mobility in PCBM and C_{60}	$1x10^{-5}$	cm^2/Vs	-
C_{60} bandgap	2	eV	[232]
C_{60} HOMO	-6.2	eV	[233]
PCBM relative permitivitty	3.9	-	[123]
C_{60} relative permitivitty	3.03	-	[234]
NIO bandgap	2.8	eV	[235]
NIO valence band	-5.3	eV	[235]
NIO relative permitivitty	8	-	[236]
Electron mobility in NIO and PEDOT:PSS	$1x10^{-5}$	cm^2/Vs	-
Hole mobility in NIO and PEDOT:PSS	1	cm^2/Vs	-
PEDOT:PSS bandgap	3	eV	[237]
PEDOT:PSS HOMO	-5	eV	[237]
PEDOT:PSS relative permitivitty	3	-	[238]
Top cell cathode fermi level	-4.9	eV	*
Top cell anode fermi level	-4.5	eV	*
Bottom cell cathode fermi level	-4.9	eV	*
Bottom cell anode fermi level	-4.5	eV	*
Bimolecular recombination constant	$1x10^{-10}$	$cm^3\ s^{-1}$	[103]

total output characteristics of the tandem cell are studied by parameterizing one subcell's properties at a time.

5.3 Results and discussion

Considering parabolic absorption approximation (absorption, $\alpha \propto \sqrt{E - E_g}$), the efficiency for a 2T tandem solar cell configuration is calculated. The top cell bandgap is varied between 1.5 eV and 2 eV and the bottom cell bandgap is varied between 0.9 eV and 1.45 eV. To start with, the parameters in table 5.1 are considered as a reference. Initially, an ideal device is simulated with no losses (such as optical and non-radiative recombination losses). The efficiency of a 2T tandem cell is calculated for different bandgaps and the thicknesses of the subcells. The simulation results for the ideal device are explained in subsection 5.3.1. Then, the traps are introduced as non-radiative recombination centers, first at the interface and then in the bulk perovskite film. In section 5.3.2, the role of these traps on the performance of the tandem cell is investigated. It is also studied how the optimum thicknesses change in the presence of different traps. Section 5.3.3 is dedicated to analyzing the effect of mobility on the optimum subcell thicknesses and the final

output of the tandem cell. In section 5.3.4, optimization of the contact workfunctions is studied to obtain the maximum output power. Finally, section 5.3.5 investigates the role of the transport layer on doping tandem cell efficiency.

5.3.1 The ideal device

In this subsection, the recombination losses within the device are neglected. A 2T tandem cell efficiency is calculated for various combinations of subcell bandgaps and thicknesses. Initially, a fixed thickness of 350 nm is chosen for both the top and bottom cells. Figure. 5.3a shows calculated tandem cell efficiency considering initial parameters from Table 5.1. The dots, ● [220], ◆ [221], ★ [220, 222],✸ [239] and ■ [222] represent some of the experimentally used bandgap combinations for 2T tandem cells. As shown in the figure, the maximum efficiency (36.6%) is achieved for an ideal device with a bottom cell bandgap of 0.95 eV and a top cell bandgap of 1.55 eV. For each bandgap of the bottom cell, there is an optimum top cell bandgap corresponding to the maximum the output power. Away from the optimum bandgap, changing the bandgap (either increasing or decreasing) leads to sub-optimum efficiency of the tandem cell.

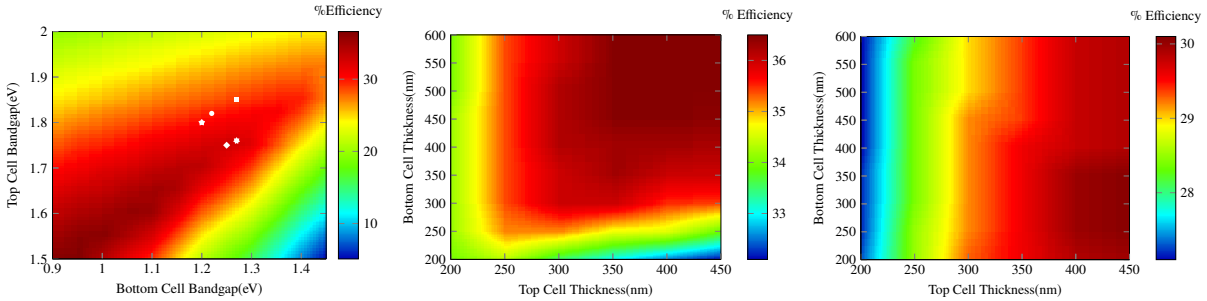

(a) **(b)** **(c)**

Figure 5.3: 2T tandem solar cell efficiency charts for different bandgap and thickness combinations: (a) Top Cell 350 nm, Bottom Cell 350 nm, (b) Top Cell 1.55 eV, Bottom Cell 1.0 eV, and (c) Top Cell 1.82 eV, Bottom Cell 1.2 eV. Reproduced with permission from ref. [101]. © 2019 International Solar Energy Society and Elsevier Ltd.

As a second analysis, the subcell thicknesses are varied while keeping fixed bandgaps. Two sets of bandgaps are chosen from Figure 5.3a; one close to the maximum output efficiency and another one close to the experimentally demonstrated bandgaps. For the first set, the bottom cell bandgap of 1.0 eV and the top cell bandgap of 1.55 eV, the calculated efficiencies are shown in Figure 5.3b. For this bandgap combination, the maximum efficiency (36.5%) is achieved corresponding to bottom cell thickness of $\simeq$ 450 nm and the top cell thickness of $\simeq$ 350 nm. Further increase in the cell thickness does not improve the output power. For bottom cell thickness of 600 nm and the top cell thickness of 450 nm, the maximum output efficiency remains to be 36.5%. On the other hand, reducing the thickness of any of the subcell (or both) results in a tandem cell with a lower output efficiency.

For the second set, the bottom cell bandgap of 1.2 eV and top cell bandgap of 1.82 eV, the calculated tandem cell efficiencies are shown in Figure 5.3c. For this bandgap combination, the maximum efficiency is achieved for the top cell thickness of 400-450 nm and the bottom cell thickness of $\simeq$ 250 nm. It is observed that the efficiency shows a

weak dependence on the bottom cell thickness, while it increases with the top cell thickness. In this case, the top cell operates at a lower current and limits the tandem cell efficiency. Increasing the top cell thickness leads to more light absorption by the top cell, and hence the top cell produces more current, resulting in higher efficiency. Therefore, increasing top cell thickness increases the tandem cell efficiency. In contrast, the bottom cell contributes only to the voltage of the tandem cell (like a voltage source). Though increasing the bottom cell thickness increases its current, the tandem cell output current is determined by the top cell only. Hence, increasing the bottom cell thickness does not increase the overall current or efficiency of the tandem cell. Since the bottom cell voltage is not much affected by its thickness, the tandem cell voltage is also not affected for the given thickness range. Ultimately, increasing bottom cell thickness beyond 350 nm does not lead to a significant enhancement in the tandem cell efficiency. This can be inferred from here that the thickness of the current-limiting-subcell limits the 2T tandem solar cell efficiency when there are no losses involved.

5.3.2 Non-ideality: The impact of interface and bulk traps, and recombinations

Trap-assisted non-radiative recombination at the interfaces have been demonstrated to be the dominant loss mechanisms in PSCs [15, 74, 75]. The perovskite interface consists of a much higher trap density compared to the bulk perovskite film; due to abrupt ending of the lattice, dislocation defects, and the presence of dangling bonds. So far, the ideal devices for both top and bottom cell were considered, without trap assisted recombinations involved. In this section, the interface traps are introduced in both the top and bottom cells. The traps are confined in the buffers defined near the perovskite/ETL and perovskite/HTL interfaces (see Figure 5.2a). Acceptor type traps are considered in the buffer region between the perovskite and the HTL. Donor type traps are considered in the buffer region between the perovskite and the ETL. Equal trapping time ($\tau_n = \tau_p$) is considered for both the electrons and the holes. Tandem cell efficiency is calculated considering both of the subcells of 350 nm thickness. The simulation results, considering the interface traps with various trapping times, are shown in Figure 5.4.

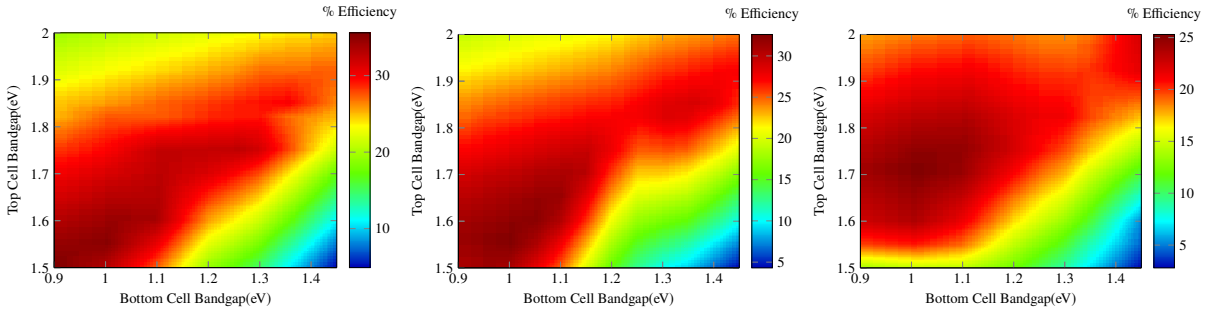

Figure 5.4: 2T tandem solar cell efficiency for (a) $\tau_n = \tau_p = 1 \times 10^{-8}$ s, (b) $\tau_n = \tau_p = 1 \times 10^{-9}$ s, and (c) $\tau_n = \tau_p = 1 \times 10^{-10}$ s. The tandem cell consists of both of the top and bottom cells of 350 nm thickness. Reproduced with permission from ref. [101]. © 2019 International Solar Energy Society and Elsevier Ltd.

The maximum achievable efficiency after introducing interface traps decreases compared to the ideal case. The efficiency continues to decrease while decreasing the trapping times. Also, there is a rapid drop in efficiency at a particular bandgap combination for a given recombination time. For $\tau_n = \tau_p = 1 \times 10^{-9}$ s, this behaviour is found for a top cell bandgap of $\simeq 1.80$ eV and the bottom cell bandgap of $\simeq 1.25$ eV as shown in Fig 5.4b. This behaviour shifts to a different bandgap combination with a change in the trapping time (Fig 5.4a and Fig 5.4c). This suggests that the maximum tandem efficiency can be achieved by tuning the bandgap away from this value. As explained in chapter 1, the bandgap of (ABX_3) perovskite can be tuned by changing the composition of A, B and/or X site.

For trapping times $\tau_n = \tau_p = 1 \times 10^{-10}$ s, the maximum efficiency is achieved for the bottom cell bandgap of $\simeq 1.1$ eV and the top cell bandgap of $\simeq 1.75$ eV. Also, in this case the maximum efficiency drops to a much lower value compared to the other two cases. For further analysis in this chapter, $\tau_n = \tau_p = 1 \times 10^{-9}$ s is chosen to account for the interface traps.

Fixing the trapping times, tandem cell efficiency is calculated for different bottom and top cells' thicknesses. The calculated efficiencies for two bandgap combinations are shown in Fig 5.5. As shown in the Figure, to obtain the optimum efficiency, comparatively thicker subcells are required for the case when 1.82 eV top cell and 1.2 eV bottom cell are used. The optimum thickness values change depending upon the strength of the trap (recombination time and/or trap density) in the subcells.

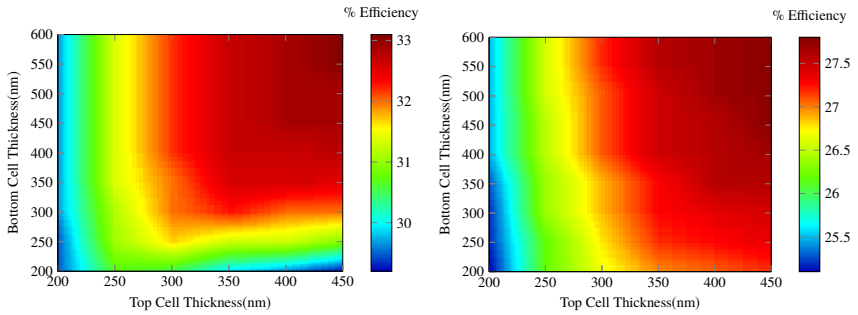

(a) **(b)**

Figure 5.5: 2T tandem cell efficiency after introducing interface traps with fixed trapping time $\tau_n = \tau_p = 1 \times 10^{-9}$ s, for (a) Top Cell 1.55 eV, Bottom Cell 1.0 eV, and (b) Top Cell 1.82 eV, Bottom Cell 1.2 eV. Reproduced with permission from ref. [101]. © 2019 International Solar Energy Society and Elsevier Ltd.

So far, the interface traps were introduced in the buffer regions. In the next analysis, the traps are introduced in the bulk perovskite film along with the interfaces. This is well known that the solution-processed perovskite films consist of grain boundaries and defect states [240, 135, 91, 19, 127]. These defect states and the grain boundaries can host the traps as explained in chapter 3. These bulk (film) traps and the grain-boundary-hosted traps act as non-radiative recombination centers for the electrons and holes, limiting the device performance [74, 241, 127, 73, 75]. This chapter does not explicitly account for the grain boundaries. Rather, the trap centers are considered to be uniformly distributed within the perovskite film. Since the bulk (film) consists a lower trap density compared to the interface, higher trapping times $\tau_n = \tau_p = 5 \times 10^{-7}$ s are considered for the perovskite

film (see eq 3.4). Including both the bulk and interface traps, calculated tandem cell efficiencies are shown in Figure 5.6.

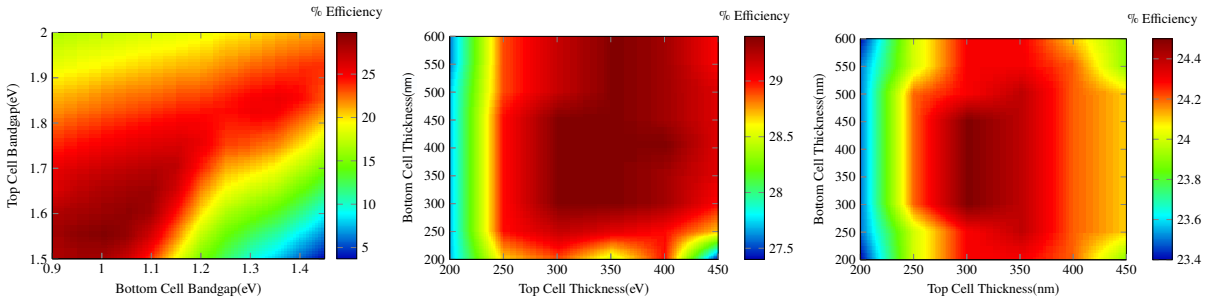

Figure 5.6: 2T tandem solar cell efficiency charts after introducing interface and bulk traps, for different bandgap and thickness combinations: (a) Top Cell 350 nm, Bottom Cell 350 nm, (b) Top Cell 1.55 eV, Bottom Cell 1.0 eV, and (c) Top Cell 1.82 eV, Bottom Cell 1.2 eV. Reproduced with permission from ref. [101]. © 2019 International Solar Energy Society and Elsevier Ltd.

Figure 5.6a shows that the overall efficiency of the tandem device decreases while considering the traps. The maximum efficiency for the tandem cell (both cells 350 nm) is achieved (29.8%) for the top cell bandgap of 1.55 eV and the bottom cell bandgap of 1.0 eV. Figures 5.6b and 5.6c show that the optimum thickness of the top cell decreases to obtain the maximum tandem cell efficiency. On the other hand, optimum power shows poor dependence on the bottom cell thickness. Changing the bottom thickness does not change (much) the maximum efficiency because the output power is limited by the top cell. Further increasing the top and bottom cell thickness results in less output efficiency because the recombination losses increase with the thickness.

5.3.3 Impact of perovskite mobility

Charge transport in methylammonium lead iodide ($CH_3NH_3Pb_3$) perovskite has been studied extensively [198, 108, 179, 112, 163, 96, 242, 243, 103, 14]. $CH_3NH_3PbI_3$ shows very good mobility, high carrier diffusion length and defect tolerance. On the other hand, not many other perovskite materials have been equivalently investigated, especially low bandgap perovskite semiconductors. For a tandem cells, different possible bandgap combinations are needed in order to obtain the maximum output power. Different materials have different chemical, physical, optical and electrical properties. For a material, mobility is one of the most important property to determine the charge transport. Higher mobility implies better charge carrier transport and hence an efficient solar cell. When the mobility in one of the subcell perovskite layers is decreased, the corresponding cell underperforms, and hence the total current in the 2T tandem cell changes.

After incorporating interface and bulk (film) traps in the simulations, this section investigates the tandem cell performance while changing the mobility of perovskite layer in the bottom cell. The bottom cell perovskite mobility is reduced to $2\,\mathrm{cm}^2/(\mathrm{V\,s})$ compared to the previous value of $5\,\mathrm{cm}^2/(\mathrm{V\,s})$. Calculated tandem cell efficiencies are shown in Figure 5.7. Figure 5.7a represents the tandem cell efficiency while changing the subcell bandgaps. The calculated efficiency for two bandgap combinations (as mentioned in section 5.3.1) are shown in Figures 5.7b and 5.7c.

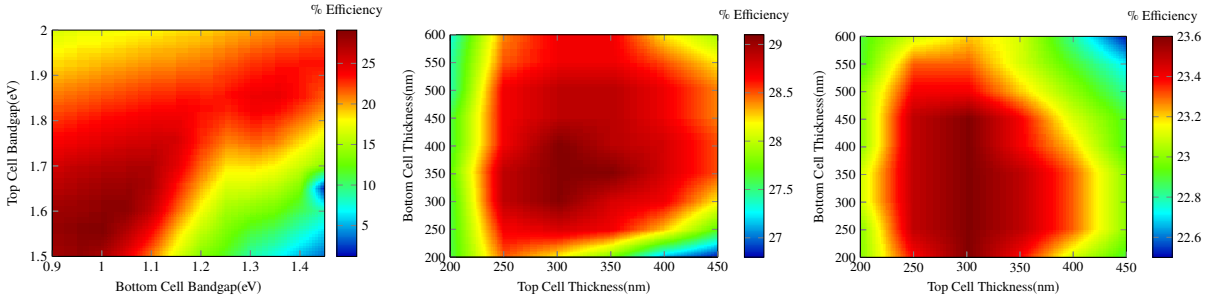

(a) **(b)** **(c)**

Figure 5.7: 2T tandem solar cell efficiency charts after introducing interface and bulk traps and lowering bottom cell mobility, for different bandgap and thickness combinations: (a) Top Cell 350 nm, Bottom Cell 350 nm, (b) Top Cell 1.55 eV, Bottom Cell 1.0 eV, and (c) Top Cell 1.82 eV, Bottom Cell 1.2 eV. Reproduced with permission from ref. [101]. © 2019 International Solar Energy Society and Elsevier Ltd.

This is evident from Figure 5.7a that, after introducing traps in the bulk perovskite film, the maximum achievable efficiency of the tandem device reduces for all of the bandgap combinations. The maximum efficiency of $\simeq 29\%$ is obtained for bottom cell 1.0 eV and top cell 1.55 eV compared to the previous case (29.8%) as shown in figure 5.6a. It is also clear that the maximum efficiency is obtained for the bandgap combination similar to the ideal device, as described in section 5.3.1 (see Figure 5.7a). On the other hand, for the given bandgap combinations, the maximum efficiency is achieved for the different subcell thicknesses as shown in Figures 5.7b and 5.7c. Lower mobility gives more time for the traps to trap the charge carriers in the perovskite film. Hence, fewer charge carriers (and/or the charge carriers with less energy) reach the contacts resulting in a poor performing solar cell.

5.3.4 Impact of contact workfunction

The energy levels of the anode and the cathode (hereafter called contacts) play an important role in the charge carrier extraction and hence in the solar cell performance. Proper energy alignment of contacts, active material, and charge transport layers (ETL and HTL) is required to obtain good charge transport, charge collection, and solar cell efficiency. Workfunctions of the contacts determine the charge extraction from the charge transport layers. Also, good energy level alignment at the interfaces between the contacts and the charge transport layers reduces contact resistance and improves the performance of the cell. Along with the charge transport layers, the contact workfunction affects the fill-factor and the V_{OC} of a single-junction perovskite solar cells [244, 245, 87]. Improper workfunctions can result in the accumulation of charge carriers in the charge transport layers, leading to capacitive effects. In a 2T tandem cell, optimizing the contact energy levels becomes even more crucial due to a need for the current matching between the subcells. The anode workfunction should be close to the lowest unoccupied molecular orbital (LUMO) level of the ETL. Similarly, the cathode workfunction should be close to the highest occupied molecular orbital (HOMO) level of the HTL, to ensure a best performing solar cell (see Figure 1.5b).

Once the subcell bandgaps and thicknesses are finalized, the contact workfunctions can be optimized to obtain a tandem cell's maximum efficiency. This section investigates the effect of contact energy levels on the final performance of the 2T tandem cell. For the tandem cell consisting of a bottom cell bandgap of 1.2 eV and a top cell bandgap of 1.82 eV (both of 350 nm thickness), tandem cell efficiency is calculated by varying the bottom cell cathode workfunction. One of the contacts' workfunction is varied at a time. Initially, the bottom cell cathode workfunction is varied, keeping all other parameters unchanged. As shown in Figure 5.8a, while varying bottom cell cathode workfunction from −5.1 eV to −4.5 eV, the tandem cell efficiency varies between 23.4% and 25.5%. The maximum efficiency (25.5%) is obtained for the cathode workfunction ≃ −4.7 eV.

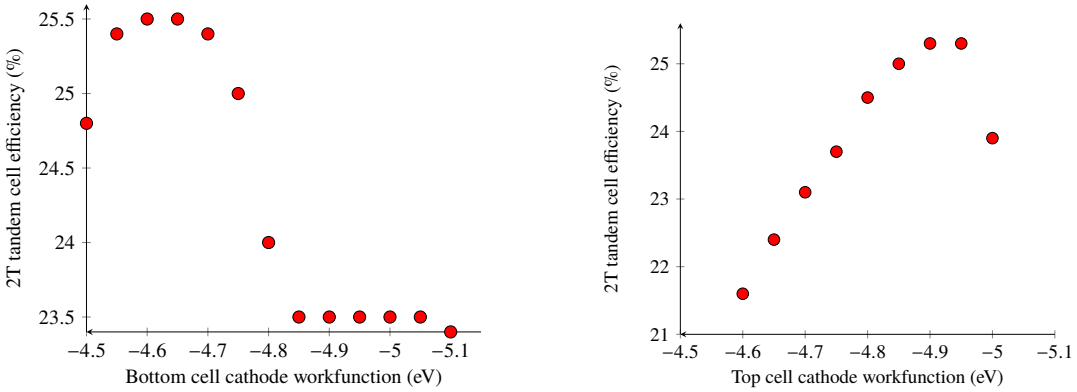

Figure 5.8: 2T tandem solar cell efficiency with cathode workfunction: Top Cell 1.82 eV, Bottom Cell 1.2 eV, both 350 nm thick. Reproduced with permission from ref. [101]. © 2019 International Solar Energy Society and Elsevier Ltd.

With a fixed bottom cell cathode workfunction to (−4.7 eV), no significant change is observed in tandem cell output power while varying the bottom cell anode workfunction. Considering optimized bottom cell contact workfunctions, bottom cell cathode (−4.7 eV) and anode (−4.3 eV) are chosen for optimizing the contact workfunctions of the top cell. Figure 5.8b shows the calculated efficiency of the tandem cell (bottom cell: 1.20 eV, 350 nm and top cell: 1.82 eV, 350 nm) with top cell cathode workfunction. It is observed that the tandem cell shows the maximum efficiency corresponding to top cell cathode workfunctions of ≃ −4.95 eV.

In conclusion, first, the optimum bandgaps and thicknesses of the subcells should be optimized. Then, based on the bandgaps and the charge transport layer's energy levels, the contact energy levels must be chosen. The final tandem cell performance is sensitive to the cathode energy levels. Therefore, the cell efficiency should be optimized by varying one of the cathode workfunction at a time. This is important to note that the optimum values of the contact workfunctions can vary with the choice of transport layers, perovskite conduction and valence band positions, and the recombination losses in the subcells. Therefore, it is advisable to optimize the contacts after optimizing the optics of the device (i.e., thicknesses and the bandgaps of the subcells).

5.3.5 Impact of charge transport layers doping

The doping level of the charge transport layer affects the performance of a single-junction solar cell, as explained in chapter 2 (Figure 2.2b). Most of the charge transport layers are synthesized by using organic materials. Doping of organic materials leads to change in their conductivity by changing mobility and the charge carrier density [246]. Apart from the change in conductivity, the doping of the charge transport layers determines the Fermi energy level of that particular layer. The improved conductivity (by doping ETL and HTL) and the energy alignment improve the performance of single-junction perovskite solar cells [247, 87, 45, 49, 50]. Similar to a single- junction solar cell, the tandem cell performance is also affected by the doping of transport layers. After optimizing the subcell bandgaps and thicknesses and the contact energy levels, this section investigates the effect of doping of the charge transport layers. So far, in this study, high mobility (doping independent) of the transport layers were considered to make sure that the cell performance is not transport-layer-limited.

A tandem cell consisting of 1.2 eV bottom cell and 1.82 eV top cell (both of 350 nm thickness) is chosen for the analysis. First, the impact of ETL and HTL doping of the bottom cell is studied. For the doping $\leq 1 \times 10^{17}\,\mathrm{cm}^{-3}$, only a slight improvement is observed in the bottom cell current and fill-factor. However, for the chosen bandgap combination, the tandem cell current is limited by the top cell, the bottom cell ETL and HTL dopings do not lead to much improvement in the final tandem cell efficiency. In the next step, ETL and HTL doping of the top cell is studied. Like the bottom cell doping, the top cell's doping slightly improves the top cell current but doesn't change much for the tandem cell. Little improvement in the final tandem device output was observed for the doping levels approaching $10^{18}\,\mathrm{cm}^{-3}$. For further higher doping, the current matching conditions for the subcells are changed; hence, the poor performance of the tandem cell efficiency is obtained. This loss in efficiency might be further optimized by changing anode and cathode workfunctions appropriately. In this study, since the bandgaps, thicknesses, and the contact workfunctions were already optimized, a poor dependence on the doping was observed. A different trend can be found for different bandgap and thicknesses combinations.

5.4 Conclusion

In conclusion, the role of various device and material parameters on the performance of a two-terminal all perovskite tandem solar cell is investigated. The role of subcell bandgaps, thicknesses, contact workfunctions, transport layer doping, and charge carrier mobility has been studied in detail. Individual subcells have been simulated by using a one-dimensional drift-diffusion model, and the 2T tandem cell has been realized by optical coupling along with a series connection circuit model. Optical coupling is achieved by using the top-cell-filtered light as an input to the bottom cell. For every bandgap pair (bottom and top cell), an optimum thickness combination is found to achieve tandem cell's maximum output power. For an ideal tandem device with each subcell thickness of 350 nm, the maximum output efficiency (36.6%) is achieved by a bottom cell bandgap of 0.95 eV and a top cell bandgap of 1.5 eV. For the ideal device, the thickness of the current-limiting-cell determines the overall current. The tandem cell efficiency is significantly reduced while introducing traps at the interface and in the perovskite film. Both the bulk

and the interface traps deteriorate the tandem cell performance. The maximum achievable efficiency reduces to $\sim 29.8\%$ for interface trap time constant $\tau_n = \tau_p = 1 \times 10^{-9}\,\mathrm{s}$, and the bulk trap time constant $\tau_n = \tau_p = 5 \times 10^{-7}\,\mathrm{s}$. This is also observed that the impact of the interface traps is bandgap selective, and hence the optimum efficiency can be achieved by tuning the bandgaps. The optimum thicknesses for the subcells depend on the traps present in the device and the charge carrier mobilities. Current matching between both subcells is crucial in order to realize the optimum output of the tandem device. To achieve the current matching, the energy level alignment throughout the tandem device (the contacts, transport layers, and the perovskite films) is very important. For the bottom cell of 1.2 eV and the top cell of 1.82 eV, optimizing the top and bottom cell cathode workfunctions leads to improve the tandem cell efficiency by up to 4 %.

The performance of a tandem device is also affected by the doping of the charge transport layers. Depending upon the transport layers' mobility and energy alignment, doping of transport layers can help to improve efficiency. Doping of the transport layers must be chosen wisely since it can even deteriorate the 2T tandem cell efficiency. For the current limiting subcell, high conductive charge transport layers are recommended. For the other subcell, the focus must be on the maximum output voltage, which can be achieved by doping of the transport layers.

6 Fabrication and characterization of $CH_3NH_3PbBr_3$ perovskite solar cells

6.1 Background

The potential use of the organic-inorganic hybrid perovskites (OIHPs) for single-junction and multijunction solar cells has already been discussed in previous chapters. So far, the best performing OIHPs employ iodine (such as $CH_3NH_3PbI_3$ and $CH(NH_2)_2PbI_3$) or mixed iodine/bromide as anion, resulting in bandgap of $1.5 - 1.6\,\text{eV}$, not far from the optimum bandgap ($1.2 - 1.4\,\text{eV}$) required for a solar cell [5, 72, 41]. Employing bromine (Br) as anion leads to an increase in bandgap compared to the iodine-based perovskites, and therefore results in low power conversion efficiency (PCE) of a solar cell [31, 72, 248]. In spite of their lower efficiency, Br-based perovskite solar cells are attractive because of their high open-circuit voltage and optical transparency [249, 250, 251, 248]. High open-circuit voltage makes them a potential candidate for electrochemical applications [252]. Because of their semitransparent nature, they are attractive for building integration photovoltaics (BIPV) and high-efficiency all-perovskite tandem solar cells [248, 253, 254, 228]. Furthermore, high photoluminescence quantum efficiency of Br-based perovskites makes them a suitable choice for light-emitting diodes and lasers [255, 256, 257, 258].

There have been several efforts to develop $CH_3NH_3PbBr_3$ (known as $MAPbBr_3$) perovskite solar cells [259, 260, 249, 251, 261]. Low-cost fabrication typically incorporates spin-coating based deposition of the perovskite and the charge transport layers. Very often, the synthesis process of $MAPbBr_3$ perovskite films is based on mixing different cation and anion precursors. In many cases, complex chemical processes and post-annealing are required to improve the film quality, and to dry the solvents used. Most of these procedures end up with a perovskite film consisting of grain boundaries (GBs) and bulk and interface traps. Interface and grain boundary traps limit the perovskite solar cell efficiency and play an active role in the JV hysteresis [81, 95, 75, 127, 140]. To obtain high-efficiency perovskite solar cell, it is very important to obtain GBs-free smooth perovskite films.

Lewis base additives have been reported to improve the quality of lead halide perovskite films by improved crystallinity and defect-passivation [262, 263, 264, 68]. Enabling self-passivation by growing microstructures on the GBs is another way to improve the perovskite film quality [265, 266]. The films with additional microstructures show better defect tolerance, therefore lead to an improved device performance. By measuring time-resolved photoluminescence (TRPL), Liu *et al.* [267] revealed that the grain-boundaries with cross-linked perovskite agents show higher charge carrier lifetime, and hence lower trap densities. Further, by using electrochemical impedance spectroscopy measurements, they showed that the cross-linked device exhibited suppressed charge recombination and enhanced charge collection.

In 2015, Zhou *et al.* [268] proposed a very simple and effective method of defect healing in $MAPbI_3$ perovskite films by using methylamine (MA) gas. They reported that the healing process involves formation of a transparent $MAPbI_3 \cdot xMA$ complex, that ultimately results into a smooth film with improved crystallinity. Thereafter, MA treatment has been applied to improve film quality of $CH_3NH_3PbI_3$ [269, 270, 271], $Cs_xMA_{1-x}PbI_{3-x}Br_x$ [272], $CH_3NH_3PbI_2Br$ [273], and $CH_3NH_3PbI_{3-x}Cl_x$ [274]. The application of MA treatment is well studied for $MAPbI_3$ based solar cells and LEDs but, in the literature, there is not much work on MA treatment for $MAPbBr_3$ perovskite solar cells. Zhang *et al.* [275], used MA gas and $PbBr_2$ to synthesize highly luminescent $CH_3NH_3PbBr_3$ (also known as $MAPbBr_3$) films. Chih *et al.* [276] reported MA treatment for $CH_3NH_3PbBr_3$ films to make perovskite LEDs using planar architecture. Chih *et. al* obtained MA gas upon a solid reaction between KOH and MACl powders at room temperature. The produced MA gas was then supplied to the $MAPbBr_3$ film for about $150-180$ sec. In the process, they obtained $MAPbBr_3$ films exhibiting pinholes. In this chapter, a two-step processing method is presented to convert a rough $MAPbBr_3$ film into a film with high transparency and grain-passivating microstructures, resulting in high efficiency of $MAPbBr_3$ perovskite solar cell. The process is much simpler and faster than the ones reported by Chih *et. al* and Zhang *et al.*. In the first step, $MAPbBr_3$ films are obtained by using spin coating, and then, the film quality is improved by using MA gas treatment. Synthesized $MAPbBr_3$ films both inside and outside the glovebox show very good film quality. This can be a very good move for commercializing $MAPbBr_3$ perovskite devices fabricated in an ambient environment. The MA treatment is performed for both planar and mesoporous structures, and it is found that the treatment is much effective for a mesoporous structure as compared to the planar structure. The MA-treated (mesoporous) films show improved transparency, passivated grains, and higher photoluminescence, enabling improved charge transport in $MAPbBr_3$ perovskite solar cells.

6.2 Experimental procedure

The experimental procedure consists of procuring materials, preparing substrate samples, fabricating solar cell devices, and characterizing films and fabricated devices. The used materials are obtained from different manufacturers, as follows:

$PbBr_2$, Titanium diisopropoxide bis(acetylacetonate), Methylamine in Ethanol solution, 4-tert-Butylpyridine (TBP), Lithium (Li) salt, Dimethyl sulfoxide (DMSO), and Toluene solution were purchased from Sigma-Aldrich. 30D TiO_2 colloidal paste and MABr were purchased from Greatcell Materials. Poly[bis(4-phenyl)(2,4,6-trimethylphenyl)amine Poly(triarylamine), (also known as PTAA) was procured from Solaris. Fluorine doped tin oxide (FTO) and indium tin oxide (ITO) were obtained from Pilkington and KINTEC, respectively. The chemicals not mentioned here were obtained from Sigma-Aldrich.

The device fabrication consists of cleaning substrate, ETL deposition, Perovskite absorber deposition, HTL deposition, and contact deposition. The fabrication process is summarized in Figure 6.1. The detailed fabrication and characterization processes are explained in the following sections.

6.2.1 FTO Sample preparation and cleaning

Tec12 FTO deposited on glass was chosen as substrate. One FTO sample of 5 cm x 5 cm consists of 16 pixel cells, each of $\simeq 0.16\,cm^2$ area. Eight of such samples were prepared at a time. In each sample, the individual pixels are electrically isolated by using laser scribing. The samples were cleaned with 1 % soap solution in deionized (DI) water. Then, the samples were ultrasonicated in acetone followed by isopropanol solution each for 10 min. The samples were then transferred to a hot plate. The hot plate temperature was then ramped to 460 °C in 40 min.

6.2.2 ETL deposition

3 mL of Titaniumdiisopropoxidebis(acetylacetonate) was mixed with 2 mL of acetylene in a clean vial. The resultant solution was then mixed with 45 mL of ethanol, to obtain a total of 50 mL of TiO_2 solution. A controlled flow of TiO_2 solution mixed with air is sprayed on the FTO samples kept on the hot plate at 460 °C. The process is known as spray-pyrolysis. After spraying, the hot-plate was turned off to bring down the samples to room temperature. The process results in compact TiO_2 (c$-TiO_2$) film of $\simeq 30$ nm.

On top of the c$-TiO_2$, mesoporous TiO_2 (mp$-TiO_2$) was deposited by using spin coating followed by sintering. For spin coating, the solution was obtained by dissolving TiO_2 colloidal paste (1 g) in ethanol (1 g). A 400 µL of resultant solution was spin coated (3000 rpm, 1 sec ramp, 20 sec deposition) on each c$-TiO_2$ sample. The spin coated samples were annealed (sintered) at 480 °C to evaporate ethanol and convert TiO_2 paste in to mp$-TiO_2$. The temperature ramp function for the sintering process is shown in Figure A.1. The combined spin coating and sintering result in to a mesoporous (c$-TiO_2$) mp$-TiO_2$ layer of $\simeq 220$ nm.

6.2.3 Perovskite deposition

Perovskite solution is prepared by dissolving 470.27 mg of CH_3NH_3Br and 1541.40 mg of $PbBr_2$ in 3 mL of DMSO. The following reaction occurs upon stirring the solution:

$$CH_3NH_3Br + PbBr_2 \longrightarrow CH_3NH_3{-}DMSO{-}PbBr_3$$

Prior to the perovskite deposition, mp$-TiO_2$ deposited samples were kept under UV ozone lamp for $\simeq 10$ min, followed by annealing at 80 °C for $\simeq 5$ min on a hot plate. Each sample from the hot plate was then spin-coated with 70 µL of $CH_3NH_3{-}DMSO{-}PbBr_3$ solution (4000 rpm, 2 sec ramp, 20 sec deposition). During the spin-coating, after 10 sec of the rotation, 200 µL of toluene was pipetted as an antisolvant for DMSO. Such a removal a solvent by using antisolvent is known as solvent quenching. During the solvent quenching, the following reaction occurs:

$$CH_3NH_3PbBr{-}DMSO{-}PbBr_3 \xrightarrow{\text{Toluene}} CH_3NH_3PbBr_3$$

Just after the spin coating, the samples were annealed at 80 °C for 5 min. The process results in an orangish $MAPbBr_3$ film with rough and hazy surface due to rapid crystallization under annealing.

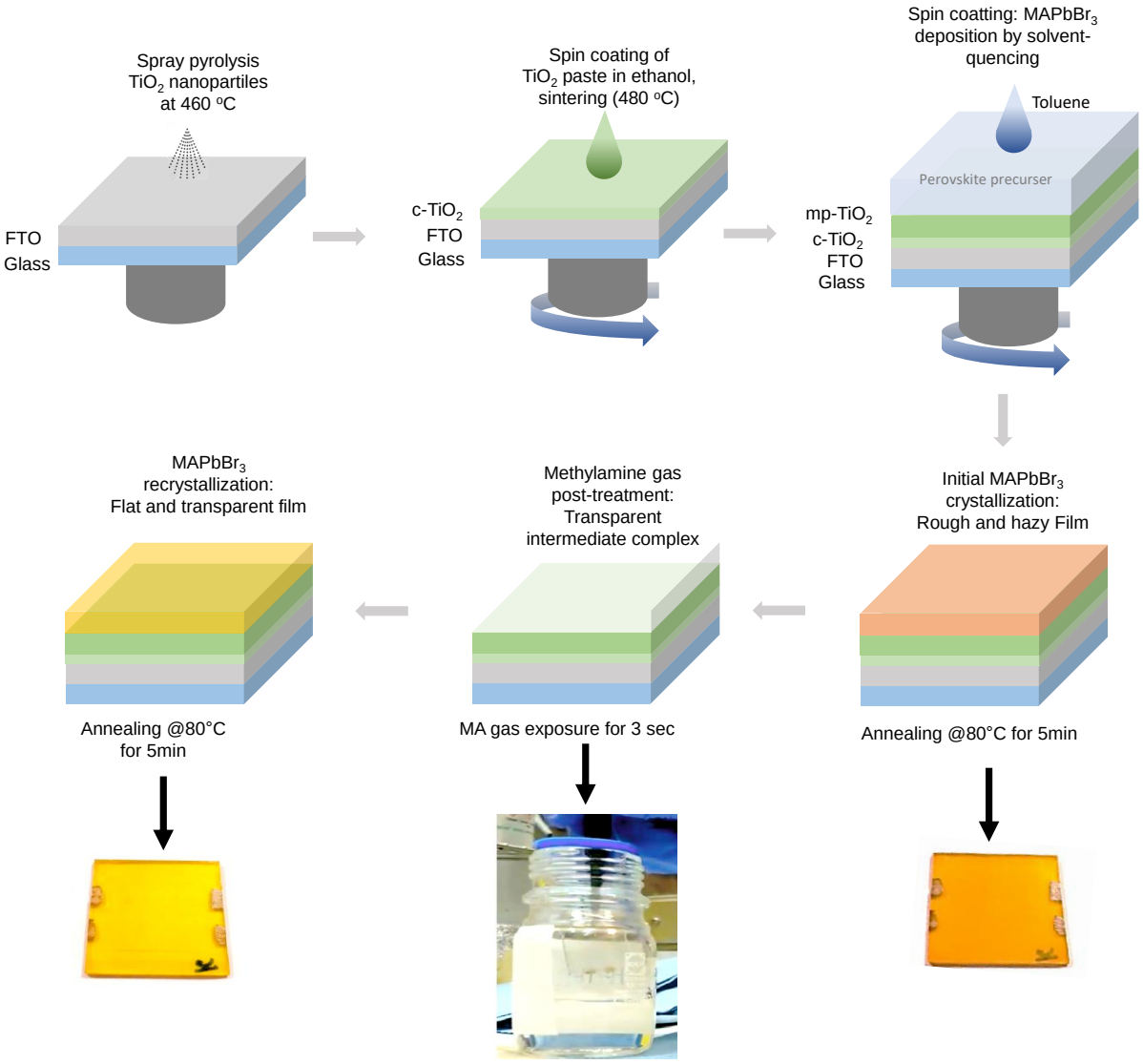

Figure 6.1: Deposition steps of $c{-}TiO_2/mp{-}TiO_2/CH_3NH_3PbBr_3$ stack, and MA gas post-treatment. $CH_3NH_3PbBr_3$ crystallization is obtained during the solvent quenching process. The $CH_3NH_3PbBr_3$ film then undergoes a recrystallization process during MA gas post-treatment. Part of the figure is reproduced with the permission from ref. [277], © 2021 Wiley-VCH GmbH.

6.2.4 MA treatment

The perovskite deposited (by the spin-coating) samples were exposed to Methylamine solution (33 wt% in absolute ethanol) for 2 sec to 3 sec. The MA (vapor) exposure leads to instantaneous conversion into a transparent intermediate as explained by the following chemical reaction suggested by Zhou *et al.* [268] for $MAPbI_3$ perovskite films:

$$MAPbBr_3(s) + MA(g) \longrightarrow MAPbBr_3{\cdot}xCH_3NH_2$$

After removing the sample from the MA exposure, the film immediately recrystallizes in a smooth yellowish film with increased visible transparency. The recrystallization method works independently from the device structure (planar or mesoporous).

6.2.5 HTL deposition

Poly[bis(4-phenyl)(2,4,6-trimethylphenyl)amin, commonly known as PTAA, was used for the hole transparent layer. However, intrinsic PTAA is not a good HTL for the device architecture used in this study. Therefore, PTAA is doped with Li salt and tributyl phosphate (TBP). 20 mg of PTAA powder was dissolved in 2 mL of toluene. Li salt solution was prepared in a separate vial, by dissolving 180 mg of Li salt in 1 mL of acetonitrile solution. As a dopent, 10 µL of Li salt solution and 20 µL of TBP and mixed in the PTAA solution. 60 µL of the doped PTAA solution was spin coated (4000 rpm, 2 sec ramp, 20 sec deposition) on the MA treated samples to obtain $\simeq$ 30 nm PTAA film as HTL.

6.2.6 Gold/ITO deposition

On some of the PTAA deposited samples, gold contacts were deposited by using thermal evaporation. The evaporation rate was kept at 0.3 Å/s for the first 10 nm, and then increased to 1 Å/s to obtain $\simeq$ 80 nm thick gold electrode. To obtain semitransparent devices, 110 nm thick ITO electrodes were deposited (instead of gold) by using low temperature RF sputtering at 60 W.

6.2.7 Characterization techniques

Transmission and reflectance spectrums were recorded by using UV-VIS-NIR Spectrophotometer (Shimadzu UV-2600i). X-ray diffraction study was done by using a Bruker D8 Cu K_α diffractometer in $\theta - 2\theta$ Bragg-Brentano configuration. Steady-state fluorescence and Time-Correlated Single Photon Counting (TCSPC) experiments were carried out on Edinburgh Instrument FLS980 spectrometer equipped with a 450 W Xe arc lamp with two excitation/emission monochromators (excitation/emission bandwidth of 2 nm). TCSPC spectra were acquired in front phase configuration using a 475 nm pulsed laser diode (FWHM 70 ps) at 1 MHz. A MCP-PMT detector (Hamamatsu) was set after the first emission monochromator. A 495 nm long-pass filter was used to avoid detection of direct light scattering. The typical IRF (Instrument Response Function) value in this configuration is in the range of 100 ps. For TCSPC, the slit bandwidth of the monochromator was set at 10 nm to maximize the PL intensity from the samples. The excitation energy from the laser diodes was chosen to be $\simeq$ 5 nJ cm^{-2}. Incident Photon-to-electron Conversion Efficiency (IPCE) was measured by using ARKEO setup (CICCI Research). JV statistics were obtained by using ARKEO Sun Simulator (CICCI Research). Maximum-power-point tracking was recorded by using ARKEO stability setup.

6.3 Results and discussion

6.3.1 Transmission and reflectance measurement

To study the optical quality of the $MAPbBr_3$ film and the device as a whole, transmission and reflectance spectra were recorded before and after the MA treatment. The transmission spectrum shown in Figure 6.2a clearly suggests an improvement in the transmission post MA treatment. In the wavelength region lower than the bandgap, the transmission

increases by $\simeq$ 20%. In the perovskite absorbance window though, the transmission is not much affected. However, the post-treatment helps to reduce the reflectance of the $MAPbBr_3$ film in the entire visible light spectrum, suggesting an improvement in the film quality. This improvement is attributed to the reduced surface roughness, pinholes and other morphological defects in the film. These morphological defects lead to the film's haze and therefore induce multiple light interactions in the non-treated film. Upon MA treatment, the Average Visible Transmittance (AVT) metric is remarkably increased from 39.5 % to 56.0 %, a very important value of semitransparent BIPVs.

Interestingly, the absorbance cut-off wavelength is blue-shifted for MA-treated film; therefore the film colour slightly changes from orange to yellow after the gas treatment. Considering a direct bandgap of $MAPbBr_3$ [28], the Tauc plot comparison shown in Figure 6.2b confirms an increase in the perovskite's bandgap from 2.31 eV to 2.34 eV post MA treatment. This bandgap energy difference corresponds to a blue-shift of 7 nm. The blue-shift is further confirmed by steady-state photoluminescence measurements.

6.3.2 Steady-state photoluminescence

Steady-state photoluminescence (PL) spectra of $MAPbBr_3$ films deposited on glass, and Glass/FTO/c$-TiO_2$/mp$-TiO_2$/Perovskite/PTAA are shown in Figure 6.2c and Figure 6.2d, respectively. The MA-treated film deposited on glass shows a higher PL intensity and narrower emission linewidth compared to the control (non MA-treated) film. The increased PL intensity suggests that the MA exposure reduces the non-radiative recombination pathways. The PL maximum is also blue-shifted by 7 nm, in agreement with the bandgap widening obtained by the Tauc plot. In complete device, i.e., perovskite film in contact with both selective layers (mp-TiO_2 and PTAA), the MA-treated film shows a greater PL quenching. This suggests that MA-treated $MAPbBr_3$-based device has a better yield of carrier injection [278, 279]. The details on PL quenching will be discussed in section 6.3.6.

To understand the role of contact layers in detail, the PL spectrum is recorded for $MAPbBr_3$ in contact with various layers. The recorded PL spectra are shown in Figure 6.3. In order to track the PL peak position, normalized PL is plotted in Figure 6.3c and Figure 6.3d. In both the cases with and without MA-treatment, an exaltation of the PL intensity is observed for the $MAPbBr_3$ film contacting the "blocking and mesoporous layers of TiO_2" in air. This exaltation of PL intensity, without any change in the emission band position and shape, is more pronounced for a non-treated MA film (+850 %) as compared to a treated MA film (+450 %). This might be due to a quenching owing to electron injection in TiO_2. This suggests that the infiltration of the perovskite inside the mesoporous layer is of better optical and photo-physical quality with fewer non-radiative defects than the control film.

6.3.3 X-ray diffraction analysis

X-ray diffraction (XRD) analysis was carried out to grasp further insights on the structural difference between the control and MA treated perovskite films. Figure 6.4a and Figure 6.4b show the recorded XRD spectra for control and MA-treated films, respectively. It is evident from the XRD analysis that $MAPbBr_3$ crystallizes in a cubic lattice within Pm-3m space group. Both control and MA-treated films are highly textured

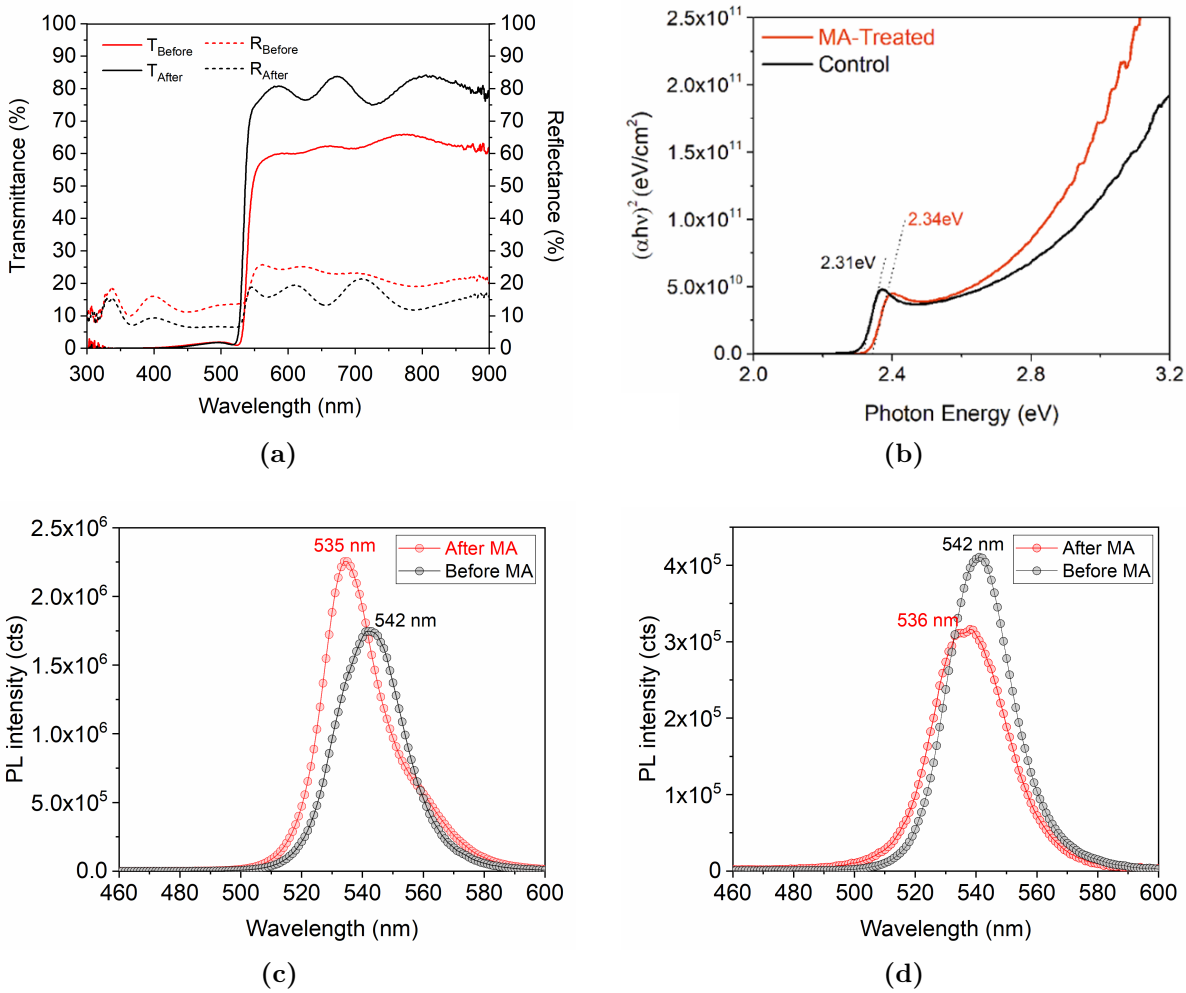

Figure 6.2: a) Transmittance (solid curves) and reflectance (dashed curves) spectra for control (black curve) and MA-Treated (red curve) Glass/FTO/c-TiO_2/mp-TiO_2/$MAPbBr_3$ stack. b) Tauc plots for the same stack, calculated for an absorber thickness of 500 nm. Comparison of steady-state photoluminescence spectrum of Glass/$MAPbBr_3$ (c), and Glass/FTO/c-TiO_2/mp-TiO_2/$MAPbBr_3$/PTAA (d) stacks for control (black curve) and MA-treated (red curve) samples. The PL excitation is done at 450 nm with an excitation and emission slit bandwidth of 1 nm. Reproduced with permission from ref. [277] (Copyright © 2021, John Wiley and Sons).

with preferential orientation along (00l) planes. The lattice cell parameter (a) refined in full pattern matching mode for the control and MA-treated films are 5.9309(2) Å and 5.9305(2) Å, respectively. These results suggest that the film stoichiometry and bulk punctual defects remain the same after the recrystallization induced by the MA treatment. However, a higher diffraction intensity is observed in the case of the MA-treated film, indicating a more textured film after the MA treatment. A difference in film's texturisation has been also reported by Zhou *et al.* in $CH_3NH_3PbI_3$ films (tetragonal crystal structure, S.G. I4/mcm) for which a MA-treatment favors the recrystallization of the (110) plane, that corresponding to the denser Pb^{2+}/I^- planes in $MAPbI_3$ [268].

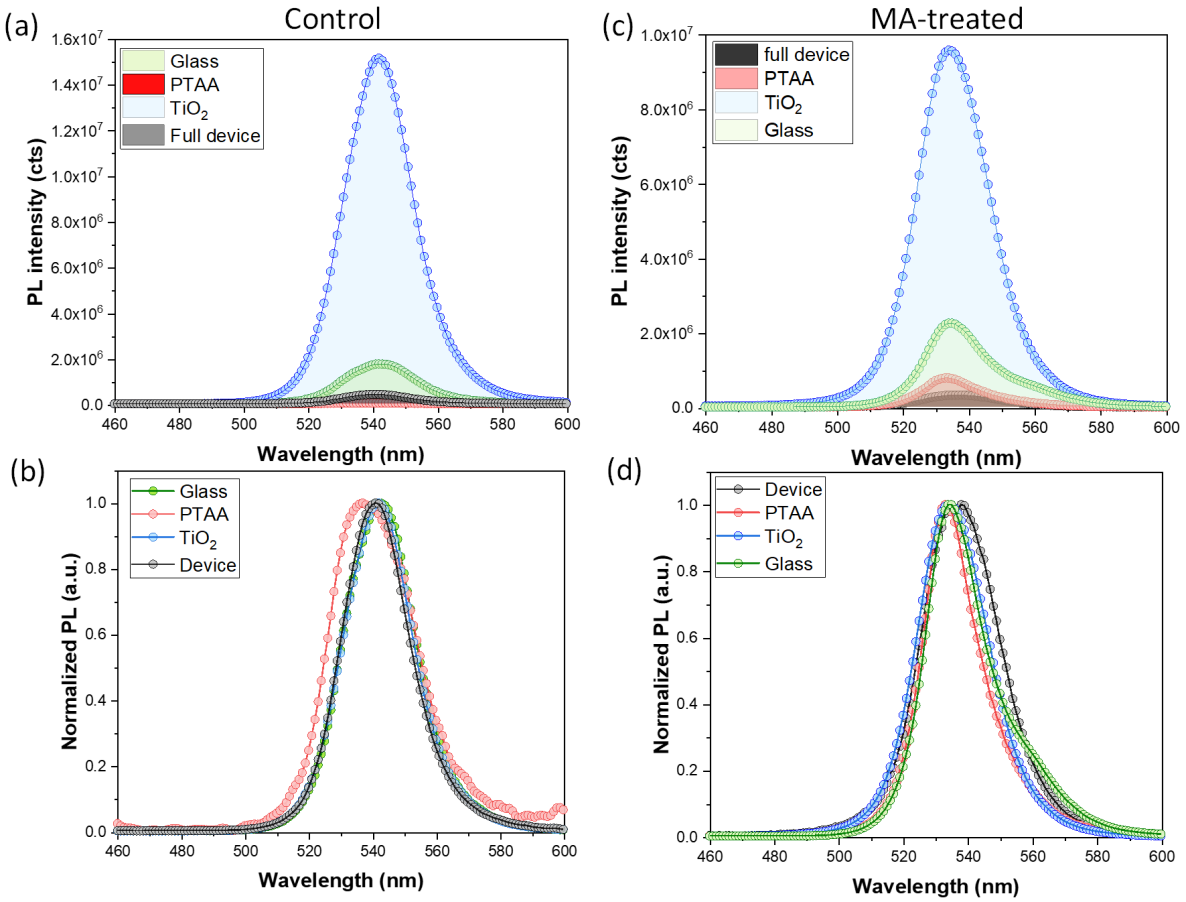

Figure 6.3: Steady-state PL spectra (a, c) and normalized spectra (b, d) of $MAPbBr_3$ film deposited on different configurations (in contact with glass, in contact with PTAA, in contact with TiO_2 and in full device). (a, b) spectra are for control-$MAPbBr_3$ and (c, d) corresponds to MA-treated $MAPbBr_3$. The normalization is done for all individual spectra. The full device corresponds to Glass/FTO/c-TiO_2/mp-TiO_2/$MAPbBr_3$/PTAA stack. Reproduced with permission from ref. [277] (Copyright © 2021, John Wiley and Sons).

6.3.4 Scanning electron microscope imaging

To study the surface morphology, scanning electron microscope (SEM) images were recorded for $MAPbBr_3$ films with and without MA treatment. Figures 6.4c and 6.4d show top view SEM images of control and MA-treated films, respectively. The top-view SEM pictures reveal a noticeable modification of the film's morphology after recrystallization. The control film shows the crystal enucleation from seed crystals (dotted squares in Figure 6.4c), leading to a network of cracks at the GBs between them. By contrast, the MA-treated film shows a coalescence phenomenon between crystals upon recrystallization. The coalescence is driven by the fast dissolution and recrystallization induced by the exposure of MA vapor and its release in ambient conditions, respectively. The films become crack-free and thus with less detrimental GBs/cracks as a result of the particle healing process as described by Zhou *et al.* [268].

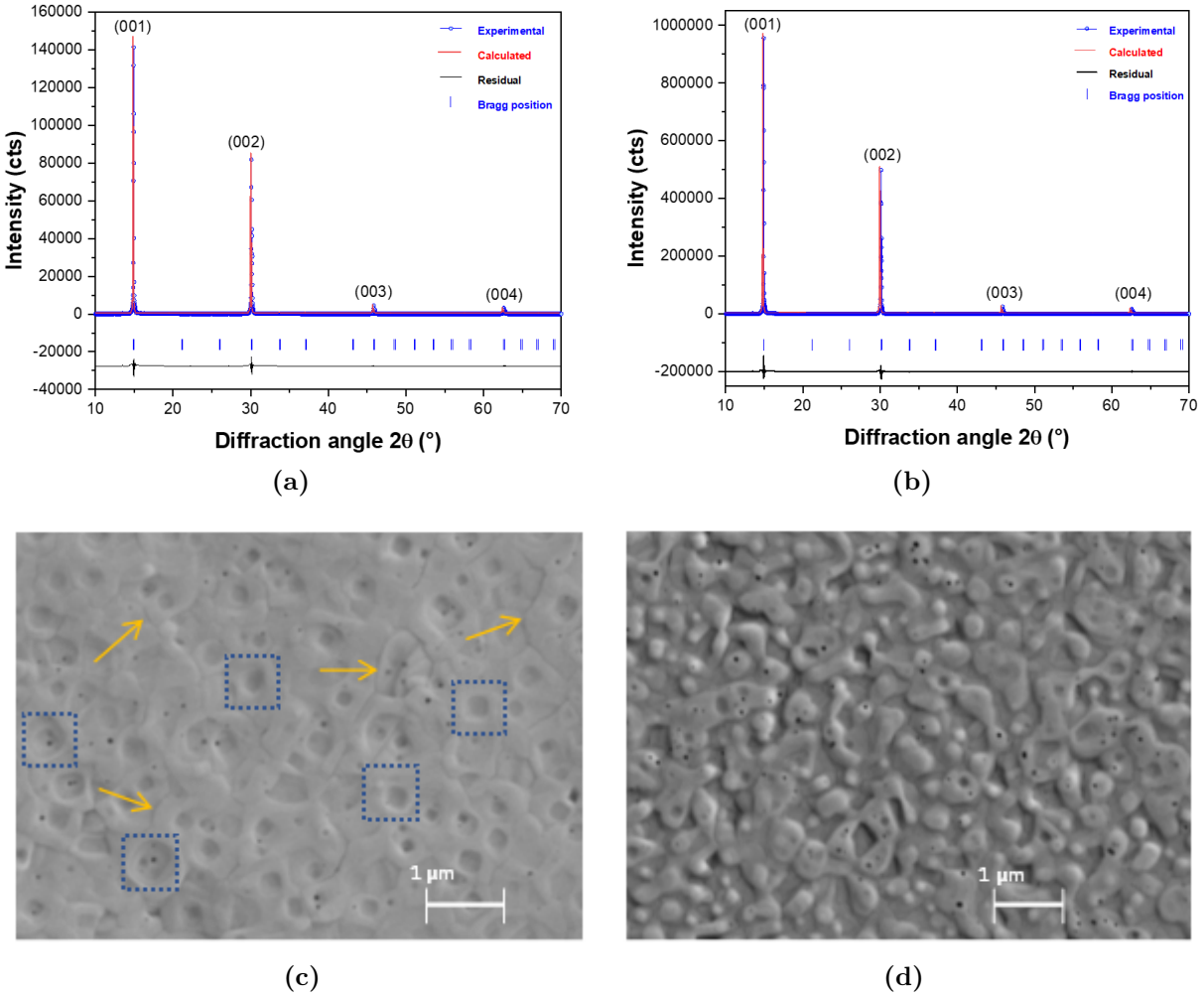

Figure 6.4: X-ray diffraction patterns refined of control (a), and methylamine-treated (b) perovskite films. c-d) Top view SEM images of the control (c), and methylamine-treated (d) perovskite films deposited upon glass/FTO/c−TiO_2/mp−TiO_2 stack. The arrows in Figure (c) indicate the presence of cracks at the grain boundaries of the control film. Dotted squares in Figure (c) represent seed crystals leading to crystals enucleation post MA treatment. Reproduced with permission from ref. [277] (Copyright © 2021, John Wiley and Sons).

6.3.5 Photovoltaic performance analysis

The control and MA-treated $MAPbBr_3$ films are used to obtain solar cell devices with a device stack of Glass/FTO/c-TiO_2/mp-TiO_2/$MAPbBr_3$/PTAA/gold. The statistical results collected on a batch of 26 different cells are shown in Figure 6.5. The results show a remarkable improvement in all the photovoltaic parameters for MA-treated devices. The most prominent change is observed in the photocurrent production which is enhanced by 2 to 3 mA/cm^2. The average fill-factor (FF) is also improved. As a result, the average PCE increases from 4.4 % (control devices) to 7.3 % (MA-treated devices) under A.M.1.5G conditions.

To study the reason behind increased photocurrent, IPCE is measured for control and MA-treated devices, as shown in 6.6a. In the wavelength range 380 nm to 530 nm, the MA-treated $MAPbBr_3$ cell shows a maximum of IPCE of $\simeq$ 90 % as compared to $\simeq$

60 % for the control cell. Considering optical reflection losses by glass surface, the MA-treated film produces a photo-current very close to the theoretical limit. Considering the reflection losses by the perovskite film, a higher optical reflectance is observed in the control film from 300 nm 550 nm corresponds to a current loss of $\simeq 0.5\,\mathrm{mA/cm^2}$ [277]. This is direct evidence of the improved film quality after recrystallization. This also means that the further 2 to 2.5 $\mathrm{mA/cm^2}$ of photocurrent enhancement should be related to the free carriers' injection (as deduced by PL measurements) and their collection. Given the high measured IPCE, the free carrier injection and collection efficiency is expected to be close to 100 % in this case. The increased charge injection can be attributed to better contact between the perovskite and TiO_2 layers, induced by the pore filling of perovskite into TiO_2. Indeed, the MA treatment triggers an extremely fast solid-to-liquid conversion upon exposure and liquid-to-solid phase transition during withdraw, therefore improves the pore filling. This improved contact between TiO_2 and perovskite is favorable for the charge injection as supported by TCSPC measurements (is discussed later).

In addition to the enhanced photocurrent and FF, average photovoltage increases by $\simeq 180\,\mathrm{mV}$ for the MA-treated devices. This enhancement could result from the reduction of non-radiative recombination pathways after MA treatment as demonstrated by PL measurements. Also, a reduction of the surface morphological defects at the mp$-TiO_2$/Perovskite interface leads to an enhanced photovoltage. The reduction into non-radiative pathways is further supported by TCSPC measurements.

Figure 6.6b shows the JV characteristics measured under reverse and forward scan for the champion devices based on control and MA-treated $MAPbBr_3$ perovskite films. The MA treatment leads to increase the PCE from 5.1 % ($J_{sc} = 5.5\,\mathrm{mA/cm^2}$, $V_{oc} = 1.37\,\mathrm{V}$) to 9.1 % ($J_{sc} = 8\,\mathrm{mA/cm^2}$, $V_{oc} = 1.53\,\mathrm{V}$). In both cases, a negligible (JV) hysteresis is observed between reverse and forward scan.

6.3.6 Time-correlated single photon counting analysis

The carrier's injection and recombination were further studied by time-resolved PL experiments using the single-photon counting technique (TCSPC). Figure 6.7 shows the PL decay of $MAPbBr_3$ either on glass or in a full device without and with MA treatment. The figure compares the excited state dynamic for the devices. Regardless of the devices, the decays require a multi-exponential function after convolution with the IRF. In case of $MAPbBr_3$ glass, two contributions (t_1 and t_2) are needed to fit the decay profile. The t_1 and t_2 contributions are attributed to band-to-band surface recombination processes for the fastest component and bulk recombination for the slowest component.

Compared to non-treated MA sample (($t_1(f_1) = 2.33\,\mathrm{ns}$ (4.5 %)), the MA-treated sample show reduced fraction and increased decay time for the fast component (($t_1(f_1) = 5.09\,\mathrm{ns}$ (3.4 %)). This results in a longer average excited state lifetime $<t>$ of 32.8 ns, as compared to 24.0 ns for the control sample. The slow component dynamic ($t_2(f_2)$) remains comparatively less affected upon the MA treatment. This suggests that, MA treatment reduces non-radiative deactivation and therefore prolongs the excited state lifetime of the absorber by reducing/slowing down surface recombination processes.

By contrast, in full devices, the decay requires a third component for the control sample. Two of the components represent the fast components ($t_1(f_1) = 0.748\,\mathrm{ns}$ (11.3 %)) and ($t_2(f_2) = 3.3\,\mathrm{ns}$ (38.8 %)) and the third component represents the dominating slower main ($t_2(f_2) = 10.58\,\mathrm{ns}$ (49.9 %)). This leads to an average lifetime $<t>$ of 3.67 ns, sig-

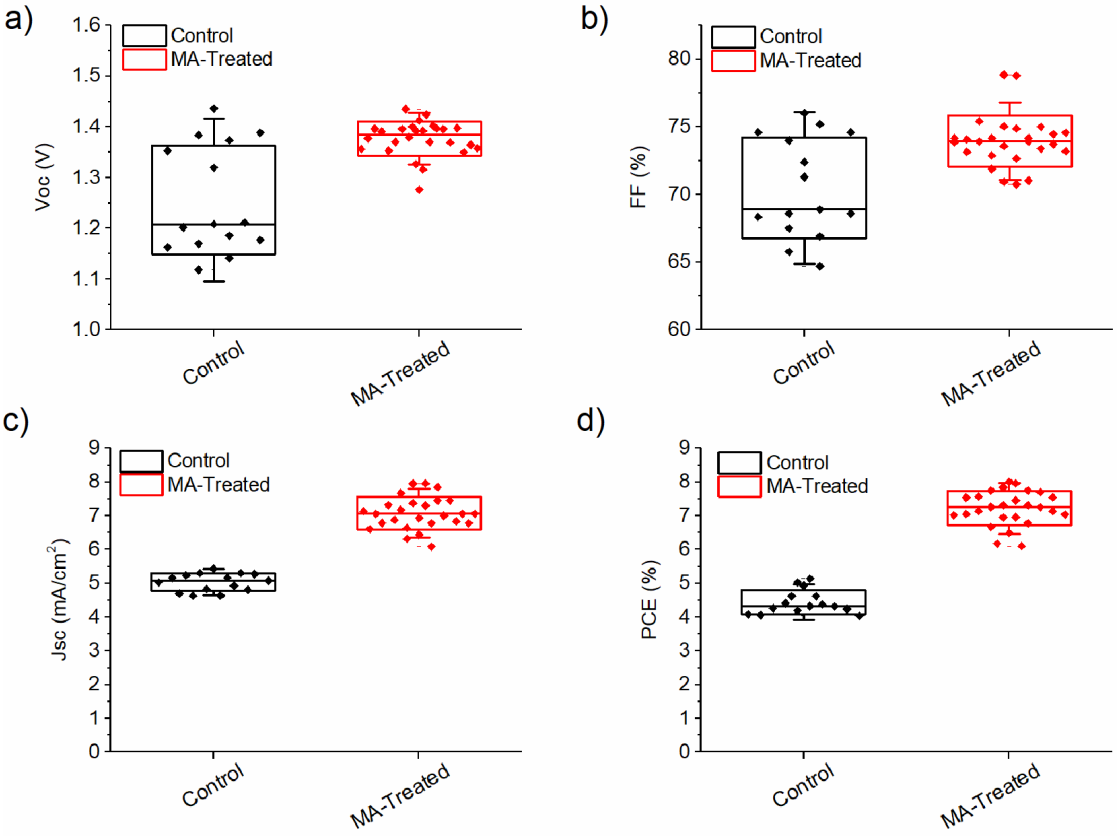

Figure 6.5: Measured open-circuit voltege (V_{oc}), short-circuit current density (J_{sc}), fill-factor (FF) and power conversion efficiency (PCE) for Glass/FTO/c-TiO_2/mp-TiO_2/$MAPbBr_3$/PTAA/gold devices. Reproduced with permission from ref. [277] (Copyright © 2021, John Wiley and Sons).

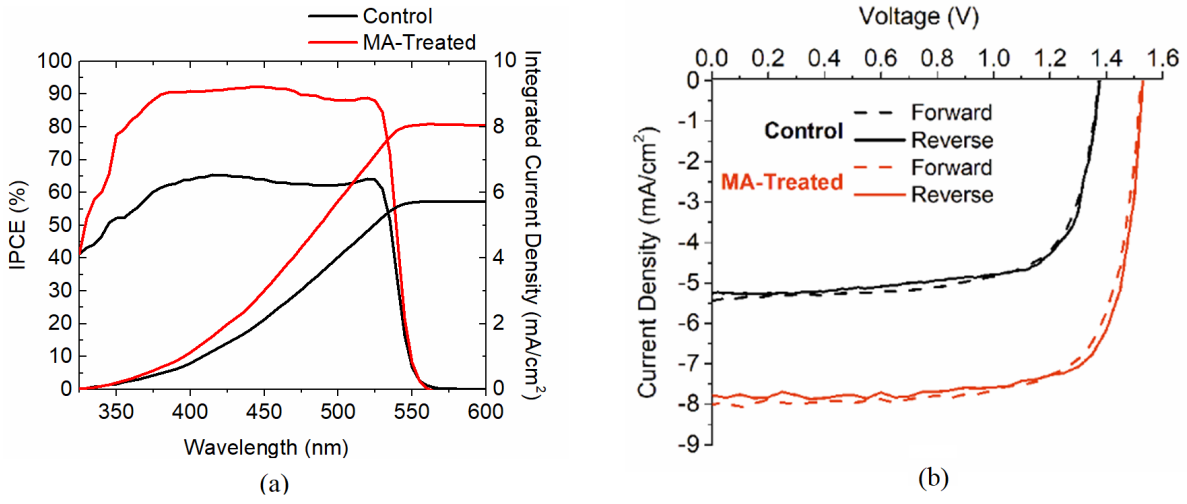

Figure 6.6: (a) Measured IPCE and integrated current density for control and the MA-treated champion devices (Glass/FTO/c-TiO_2/mp-TiO_2/$MAPbBr_3$/PTAA/gold). (b) JV characteristics measured for the same devices. Reproduced with permission from ref. [277] (Copyright © 2021, John Wiley and Sons).

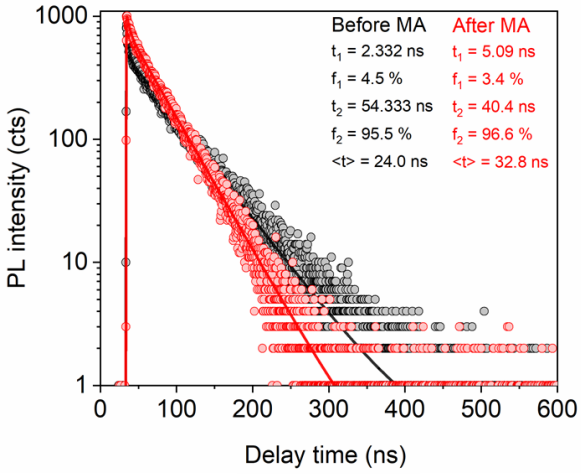

(a)

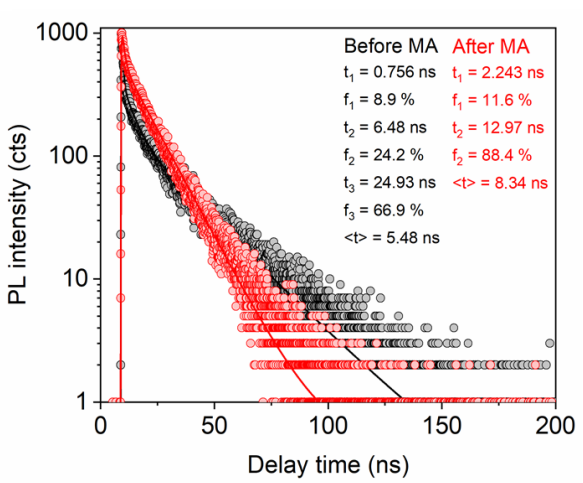

(b)

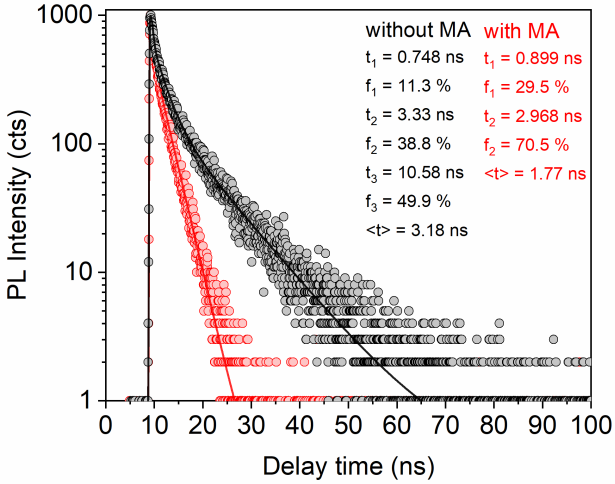

(c)

Figure 6.7: Time-Resolved PL measurement for (a) Glass/Perovskite, (b) Glass/FTO/c-TiO_2/mp-TiO_2/Perovskite, and (c) Glass/FTO/c-TiO_2/mp-TiO_2/Perovskite/PTAA device stacks with and without MA-treated $MAPbBr_3$ perovskite films. The device stacks in (c) are known as Control and MA-treated in case of without and with MA-treatment, respectively. The measurements were carried out with an excitation wavelength of 475 nm, emission at 540 nm with bandwidth of 10 nm, and the excitation pulse energy of 5 nJ cm^{-2}. Reproduced with permission from ref. [277] (Copyright © 2021, John Wiley and Sons).

nificantly faster than the Glass/$MAPbBr_3$ case (24.0 ns) because of the injection of the free carriers into the charge transport layers. Based on these two average values, the estimated yield of injection is 86.7 %. By contrast, the MA-treated device requires only two components ($t_1(f_1)$ = 0.899 ns (29.5 %)) and ($t_2(f_2)$ = 2.97 ns (70.5 %)) leading to an excited state average lifetime $<t>$ of 1.77 ns. The dynamic of these two components are similar to the two faster contributions of the non-treated film. Interestingly, the MA-treatment suppresses the slowest contribution, leading to increased injection yield of 94.5 %. Note that this value is close to the maximum of IPCE suggesting that the charge collection efficiency is close to 100 % in the MA-treated sample. The two faster contri-

butions correspond to the extraction of the carriers by the transport layers. The slowest third contribution in the non-MA-treated film comes from the interfacial recombination process either at TiO_2/Perovskite interface or Perovskite/PTAA interface in agreement with Kirchartz *et al.* [280]. In case of Glass/FTO/c-TiO_2/mp-TiO_2/Perovskite stack, the only charge injection is from perovskite into TiO_2, therefore all the 't' are lower compared to a full device (charge injection from perovskite into TiO_2 and PTAA), but higher compared to Glass/Perovskite (no change injection). To summarize, the TCSPC results support (i) the improved yield of free carriers' extraction of from $MAPbBr_3$ layer upon MA-treatment, and (ii) the MA treatment suppresses detrimental interfacial recombination processes which induce the device performance losses. The improved charge injection translates into an increased IPCE and hence the photocurrent. The suppression of interfacial recombination centers results in increased photovoltage of the device.

Another very important advantage of MA treatment is that this process works even when the devices are fabricated entirely in the air (without a controlled environment, such as N_2). To prove this, a double-step deposition method was adopted for the same $MAPbBr_3$ device stack processed in air. Figure A.2 shows the JV characteristics and the maximum-power-point tracking (MPPT) measurement for control and MA-treated samples fabricated in air. The results show that the both the J_{sc} and V_{oc} values are enhanced upon the MA treatment. This results in the PCE increasing from 5.5 % to 8.2 % after the MA-treatment. The results suggest that the MA-treatment is a universal defect-healing method to improve the efficiency and semi-transparency of $MAPbBr_3$ PSCs, independent of the deposition method and the environment used for processing the perovskite film.

6.3.7 Semitransparent solar cells

The main advantage of using wide-bandgap perovskites is their optical transparency. $MAPbBr_3$ has a bandgap of ca. 2.3 eV, very much suitable for semitransparent BIPV applications. In this work, optically opaque gold back-contact has been replaced by a transparent RF-sputtered ITO electrode. Lamanna *et al.* [210] have demonstrated the effectiveness of the sputtered ITO on top of the PTAA polymer without using buffer layers. The transparent 110 nm-thick ITO layer shows an optimized AVT of 85 % and a sheet resistance value of 34 $\Omega/\square$. A thicker ITO layer shows poor AVT value, while a thinner layer can result in higher sheet resistance. Use of too thin ITO layer results in a physically weaker electrode. For the full device stack, a batch of twenty MA-treated semitransparent devices is obtained. The results show an average AVT and PCE of 52 % and 6.50 %, respectively (Figure 6.8). The champion cell shows a PCE of $\simeq$ 7.8% with a V_{oc} exceeding 1.52 V. The photovoltaic performance can further be optimized by optimizing ITO deposition parameters with respect to the device stack. Furthermore, this is important to note that ITO may not have an ideal workfunction for the FTO/TiO_2/$MAPbBr_3$/PTAA device stack. Using a different workfunction transparent electrode can further increase the photovoltage and the device efficiency.

Figure 6.9 shows some of the real pictures of the ITO based semitransparent MA-treated devices. To study the stability of the semitransparent cells, the light soaking test at maximum-power-point were performed following the ISOS-L-1 protocol reported by Khenkin *et al.* [281], as shown in Figure 6.10. The PCE increases within the first few 10 h, with a plateau between 20 h to 40 h under operating condition. Remarkably, a non-encapsulated semitransparent device retains more than 80 % of the initial PCE after

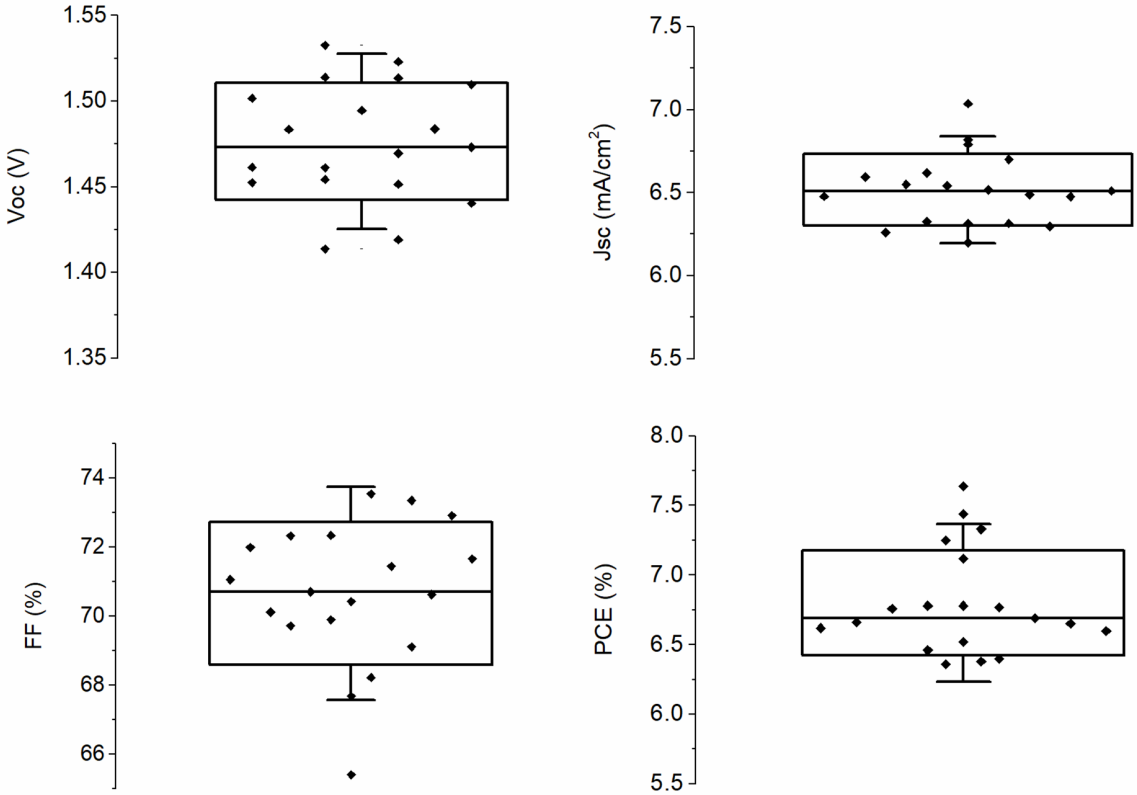

Figure 6.8: Measured open-circuit voltage (V_{oc}), short-circuit current density (J_{sc}), fill-factor (FF) and power conversion efficiency (PCE) for semitransparent Glass/FTO/c-TiO_2/mp-TiO_2/$MAPbBr_3$/PTAA/ITO devices. Reproduced with permission from ref. [277] (Copyright © 2021, John Wiley and Sons).

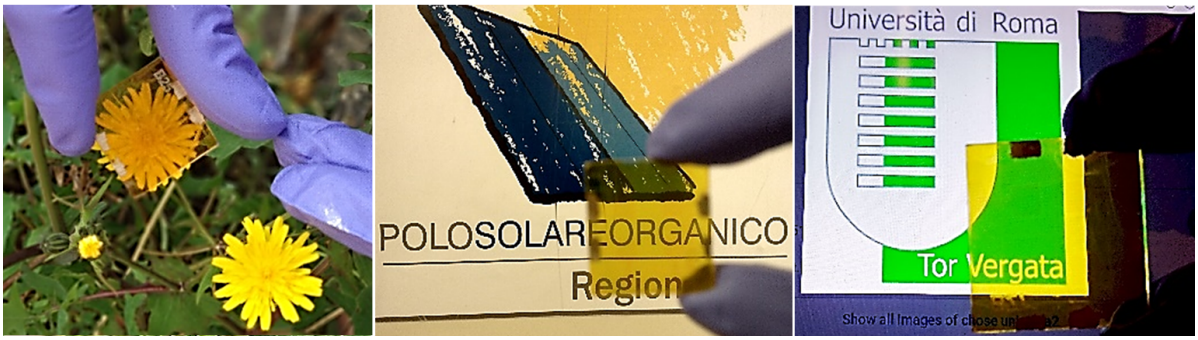

Figure 6.9: Fabricated semitransparent Glass/FTO/c-TiO_2/mp-TiO_2/$MAPbBr_3$/PTAA/ITO solar cell devices.

270 h. These encouraging results demonstrate that MA-treatment affords fabrication of semitransparent, highly efficient, and stable $MAPbBr_3$ PSCs.

6.4 Conclusion

In conclusion, MA-treated $MAPbBr_3$ perovskite solar cells are obtained exceeding a PCE of 9 % an excellent fill factor value approaching 80 %. The cells show a negligible JV

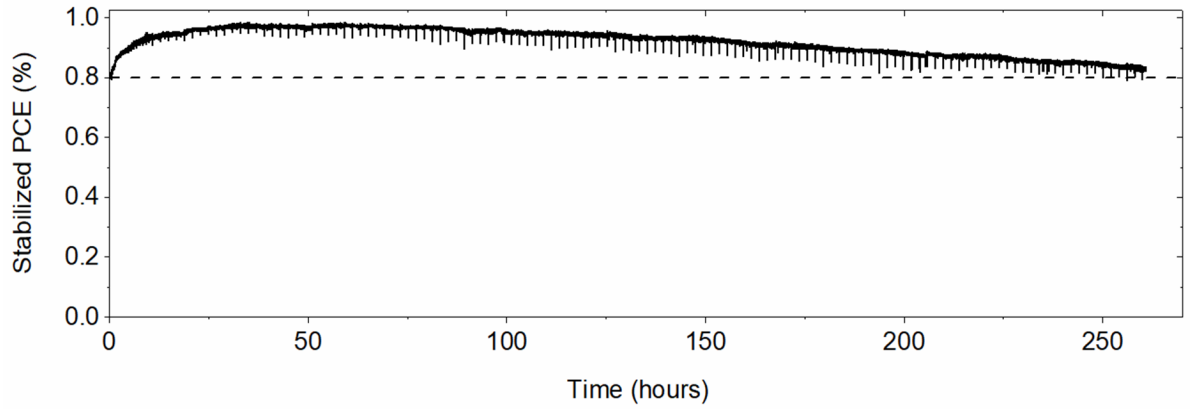

Figure 6.10: PCE stability tracking over the maximum-power-point for a semitransparent Glass/FTO/c-TiO_2/mp-TiO_2/$MAPbBr_3$/PTAA/ITO solar cell device. Reproduced with permission from ref. [277] (Copyright © 2021, John Wiley and Sons).

hysteresis. The rapid and easy MA-treatment minimizes non-radiative recombination pathways, and therefore helps to obtain a V_{oc} of higher than 1.5 V, a value close to the record for $MAPbBr_3$ PSCs [282]. The XRD, SEM and PL measurements confirm the morphologically improved and less defective $MAPbBr_3$ perovskite films after MA treatment. TCSPC measurements show that the MA treatment suppresses non-radiative recombinations and improves the charge injection from the perovskite to the TiO_2 layer. Reduced reflection losses and improved contact between the perovskite and the TiO_2 layers result in a remarkable enhancement of the photo-current produced by the cell. Improved optical transparency and reduced reflection losses after the recrystallization help obtaining more transparent solar cells. An ITO electrode-based semitransparent solar cell shows ca. 55 % of AVT. Even without encapsulation, semitransparent devices show very good stability under operating conditions. The MA treatment works well for device fabrication under both nitrogen and ambient environments. Therefore, the proposed MA treatment is a versatile chemical route to obtain highly efficient, transparent and stable $MAPbBr_3$ PSCs.

7 Summary and outlook

The thesis presents a combined theoretical and experimental study of organic-inorganic hybrid perovskite (OIHP) solar cells. Chapter 1 presents a brief introduction of state of art OIHP materials and solar cells, and the motivation to push this technology further. Chapter 2 focuses on developing a one-dimension drift-diffusion method to simulate a perovskite solar cell. The simulation results show that the interface traps significantly limit the solar cell performance. If the charges near the interfaces can be collected before they recombine, the loss in performance can be mitigated. Doping of HTL helps in the charge collection and hence improves the solar cell performance. The contact workfunctions also play an important role in determining the energetics throughout the device, therefore affect the device performance. With limited options available for the charge transport layers, it is not easy to obtain the best energetics. Interestingly, materials such as Lewis base and Lewis acids can tune the OIHPs' workfunction near the interfaces. Simulation results reveal that tuning the perovskite interface workfunction can significantly improve the solar cell output efficiency.

This is well known that the solution process methods result in grain boundaries (GBs) in OIHP films. Perovskite films with GBs result in the poor photovoltaic performance of a perovskite solar cell [136, 108]. The grain boundaries host traps and provide a path for ionic defect migration. Therefore, the GBs reduce efficiency and play a role in the JV hysteresis [73, 127, 137, 80]. Chapter 3 presents the role of GBs as non-radiative recombination centers for the charge carriers. The combined effect of interface and GBs lead to losses in photovoltage. Furthermore, the simulations showed that the solar cell performance is significantly affected when the ionic defects accumulate at the GBs and the interfaces. Therefore, future research should be focused on developing methods to obtain GBs free perovskite films.

Chapter 4 investigates JV hysteresis' origin and evolution in JV characteristics of a perovskite solar cell. A time-dependent drift-diffusion study proposes that the JV hysteresis originates from the ionic defect migration in conjunction with trap centers. However, this hysteresis can be very negligible. Interestingly, when the mobile cations act as trap centers for electrons, the simulations obtain hysteresis index values similar to those measured experimentally. This is a very important finding to gain insight into the role of ionic-electronic interactions in the JV hysteresis. This study, along with the First-principle study, can solve the well-known puzzle of JV hysteresis in perovskite solar cells. The developed drift-diffusion method can also be further extended to study various dynamic phenomena in perovskite solar cells.

Chapter 5 focuses on the potential of fully-perovskite 2T tandem solar cells. The present study predicts that the 2T tandem cells can obtain practical efficiencies up to 30% even in the presence of various loss mechanisms. The study presents a look-up chart for choosing the best design and material parameters for optimum output efficiency. The model also proposes ways to optimize the full device, i.e., doping of charge transport layers and optimizing contact workfunctions. Overall the study will help the experimentalists

in developing highly efficient and low-cost fully-perovskite 2T tandem solar cells. In the study, the role of recombination layer between the two sub-cells has been ignored. The obtained results are accurate enough to get an estimation of various parameters. However, considering a recombination layer and adopting better optical models can help to improve the accuracy of the results.

Chapter 6 proposes a new chemical route to obtain highly transparent and GBs-passivated $CH_3NH_3PbBr_3$ perovskite films. The experimental method by using methylamine gas treatment is proposed to obtain high efficiency, semitransparent $CH_3NH_3PbBr_3$ perovskite solar cells. The characterization by SEM, XRD, photoluminescence (PL), time-resolved PL, and IPCE and JV measurements reveal the tremendous improvement in transparency and photovoltaic performance while employing the methylamine gas treatment. The semitransparent cells are obtained by using ITO as back contact. The developed semitransparent cells have potential application in BIPVs and tandem perovskite solar cells. The ITO back contact under-performs as compared to the gold contacts. Optimizing ITO deposition parameters and/or replacing ITO with a suitable transparent contact can help to improve the device efficiency further. Furthermore, the MA treatment can be mimicked to improve other devices' performance based on $CH_3NH_3PbBr_3$, i.e., LEDs and Lasers. The method is also helpful for electrochemical applications where cells with high open-circuit-voltage are desired. Most importantly the MA treatment works independently of substrate morphology (i.e., planar or mesoporous), and works well for the fabrication in ambient conditions. This could be a very good move towards commercialization of this technology.

Overall the thesis covers broad aspects of OIHP solar cells. Investigation of various loss mechanisms and ways to improve are proposed. A new insight has been presented to understand the JV hysteresis in perovskite cells. Optimum design parameters have been presented to develop fully-perovskite high-efficiency 2T tandem perovskite solar cells. A new chemical route is presented to obtain semitransparent perovskite solar cells for BIPVs and tandem solar cells.

Bibliography

[1] bp. Statistical review of world energy 2020 — 69th edition, 2020. URL: https://www.bp.com/content/dam/bp/business-sites/en/global/corporate/pdfs/energy-economics/statistical-review/bp-stats-review-2020-full-report.pdf.

[2] W. E. Council. World energy resources: Solar world energy council 2013, 2013. URL: https://www.worldenergy.org/assets/images/imported/2013/10/WER_2013_8_Solar_revised.pdf.

[3] D. Feldman and R. Margolis. Q4 2019/q1 2020 solar industry update, 2020. URL: https://www.nrel.gov/docs/fy20osti/77010.pdf.

[4] P. Würfel and U. Würfel. *Physics of solar cells: from basic principles to advanced concepts*. John Wiley & Sons, 2016.

[5] Solar cell efficiency chart, NREL, Accessed on 07 October 2020. URL: https://www.nrel.gov/pv/assets/pdfs/best-research-cell-efficiencies.20200925.pdf.

[6] J. Liu, Y. Yao, S. Xiao, and X. Gu. Review of status developments of high-efficiency crystalline silicon solar cells. *J. Phys. D: Appl. Phys.*, 51(12):123001, 2018.

[7] M. Yamaguchi, K.-H. Lee, et al. A review of recent progress in heterogeneous silicon tandem solar cells. *J. Phys. D: Appl. Phys.*, 51(13):133002, 2018.

[8] M. K. Sahoo and P. Kale. Restructured porous silicon for solar photovoltaic: A review. *Microporous Mesoporous Mater.*, 289:109619, 2019.

[9] M. A. Zahid, M. Q. Khokhar, E.-C. Cho, Y. H. Cho, and J. Yi. Impact of anti-reflective coating on silicon solar cell and glass substrate: A brief review. *Curr. Photovolt. Res.*, 8(1):1–5, 2020.

[10] M. Benghanem and A. Almohammedi. *Organic Solar Cells: A Review*. Springer, 2020.

[11] J. Gao, J. Wang, C. Xu, Z. Hu, X. Ma, et al. A critical review on efficient thick-film organic solar cells. *Solar RRL*, 4(11):2000364, 2020.

[12] Y. Xu, H. Yao, L. Ma, J. Wang, and J. Hou. Efficient charge generation at low energy losses in organic solar cells: a key issue review. *Rep. Prog. Phys.*, 83(8), 2020.

[13] S. M. Menke, N. A. Ran, G. C. Bazan, and R. H. Friend. Understanding energy loss in organic solar cells: Toward a new efficiency regime. *Joule*, 2(1):25–35, 2018.

[14] J. S. Manser, J. A. Christians, and P. V. Kamat. Intriguing optoelectronic properties of metal halide perovskites. *Chem. Rev.*, 116(21):12956–13008, 2016.

[15] C. Wehrenfennig, G. E. Eperon, M. B. Johnston, H. J. Snaith, and L. M. Herz. High charge carrier mobilities and lifetimes in organolead trihalide perovskites. *Adv. Mater.*, 26(10):1584–1589, 2014.

[16] L. Qiu, S. He, L. K. Ono, S. Liu, and Y. Qi. Scalable fabrication of metal halide perovskite solar cells and modules. *ACS Energy Lett.*, 4(9):2147–2167, 2019.

[17] Z. Song, C. L. McElvany, A. B. Phillips, I. Celik, P. W. Krantz, et al. A technoeconomic analysis of perovskite solar module manufacturing with low-cost materials and techniques. *Energy Environ. Sci.*, 10(6):1297–1305, 2017.

[18] H. Chen, Z. Wei, X. Zheng, and S. Yang. A scalable electrodeposition route to the low-cost, versatile and controllable fabrication of perovskite solar cells. *Nano Energy*, 15:216–226, 2015.

[19] J. Y. Kim, J.-W. Lee, H. S. Jung, H. Shin, and N.-G. Park. High-efficiency perovskite solar cells. *Chem. Rev.*, 120(15):7867–7918, 2020.

[20] Perovskite solar cell developers. URL: `https://www.perovskia.solar/,https://www.oxfordpv.com/,https://u-renew.com/,https://www.enecoat.com/en/,https://www.p3ctsl.com/,http://cubicpv.com/,https://www.perovskite-info.com/companies/perovskite-solar-panels-developers`.

[21] C. Li, X. Lu, W. Ding, L. Feng, Y. Gao, and Z. Guo. Formability of ABX_3 (X= F, Cl, Br, I) halide perovskites. *Acta Crystallogr., Sect. B: Struct. Sci.*, 64(6):702–707, 2008.

[22] W. Travis, E. Glover, H. Bronstein, D. Scanlon, and R. Palgrave. On the application of the tolerance factor to inorganic and hybrid halide perovskites: a revised system. *Chem. Sci.*, 7(7):4548–4556, 2016.

[23] C. C. Stoumpos, C. D. Malliakas, and M. G. Kanatzidis. Semiconducting tin and lead iodide perovskites with organic cations: Phase transitions, high mobilities, and near-infrared photoluminescent properties. *Inorg. Chem.*, 52(15):9019–9038, 2013.

[24] K. P. Ong, T. W. Goh, Q. Xu, and A. Huan. Structural evolution in methylammonium lead iodide $CH_3NH_3PbI_3$. *J. Phys. Chem. A*, 119(44):11033–11038, 2015.

[25] P. Whitfield, N. Herron, W. Guise, K. Page, Y. Cheng, et al. Structures, phase transitions and tricritical behavior of the hybrid perovskite methyl ammonium lead iodide. *Sci. Rep.*, 6(1):1–16, 2016.

[26] M. T. Weller, O. J. Weber, J. M. Frost, and A. Walsh. Cubic perovskite structure of black formamidinium lead iodide, α-$[HC(NH_2)_2]PbI_3$, at 298 K. *J. Phys. Chem. Lett.*, 6(16):3209–3212, 2015.

[27] Y. Ye, X. Run, X. Hai-Tao, H. Feng, X. Fei, and W. Lin-Jun. Nature of the band gap of halide perovskites ABX_3 (A= CH_3NH_3, Cs; B= Sn, Pb; X= Cl, Br, I): First-principles calculations. *Chin. Phys. B*, 24(11):116302, 2015.

[28] J. M. Richter, K. Chen, A. Sadhanala, J. Butkus, J. P. Rivett, et al. Direct bandgap behavior in rashba-type metal halide perovskites. *Adv. Mater.*, 30(52):1803379, 2018.

[29] S. De Wolf, J. Holovsky, S.-J. Moon, P. Löper, B. Niesen, et al. Organometallic halide perovskites: sharp optical absorption edge and its relation to photovoltaic performance. *J. Phys. Chem. Lett.*, 5(6):1035–1039, 2014.

[30] S. D. Stranks, G. E. Eperon, G. Grancini, C. Menelaou, M. J. Alcocer, et al. Electron-hole diffusion lengths exceeding 1 micrometer in an organometal trihalide perovskite absorber. *Science*, 342(6156):341–344, 2013.

[31] E. T. Hoke, D. J. Slotcavage, E. R. Dohner, A. R. Bowring, H. I. Karunadasa, and M. D. McGehee. Reversible photo-induced trap formation in mixed-halide hybrid perovskites for photovoltaics. *Chem. Sci.*, 6(1):613–617, 2015.

[32] I. E. Castelli, J. M. García-Lastra, K. S. Thygesen, and K. W. Jacobsen. Bandgap calculations and trends of organometal halide perovskites. *APL Mater.*, 2(8):081514, 2014.

[33] Z. Hu, Z. Lin, J. Su, J. Zhang, J. Chang, and Y. Hao. A review on energy band-gap engineering for perovskite photovoltaics. *Solar RRL*, 3(12):1900304, 2019.

[34] E. Unger, L. Kegelmann, K. Suchan, D. Sörell, L. Korte, and S. Albrecht. Roadmap and roadblocks for the band gap tunability of metal halide perovskites. *J. Mater. Chem. A*, 5(23):11401–11409, 2017.

[35] A. Kojima, K. Teshima, Y. Shirai, and T. Miyasaka. Organometal halide perovskites as visible-light sensitizers for photovoltaic cells. *J. Am. Chem. Soc.*, 131(17):6050–6051, 2009.

[36] J.-H. Im, C.-R. Lee, J.-W. Lee, S.-W. Park, and N.-G. Park. 6.5% efficient perovskite quantum-dot-sensitized solar cell. *Nanoscale*, 3(10):4088–4093, 2011.

[37] H.-S. Kim, C.-R. Lee, J.-H. Im, K.-B. Lee, T. Moehl, et al. Lead iodide perovskite sensitized all-solid-state submicron thin film mesoscopic solar cell with efficiency exceeding 9%. *Sci. Rep.*, 2(1):1–7, 2012.

[38] M. M. Lee, J. Teuscher, T. Miyasaka, T. N. Murakami, and H. J. Snaith. Efficient hybrid solar cells based on meso-superstructured organometal halide perovskites. *Science*, 338(6107):643–647, 2012.

[39] W. Chen, X. Yin, M. Que, H. Xie, J. Liu, C. Yang, Y. Guo, Y. Wu, and W. Que. A comparative study of planar and mesoporous perovskite solar cells with printable carbon electrodes. *J. Power Sources*, 412:118–124, 2019.

[40] T. Leijtens, B. Lauber, G. E. Eperon, S. D. Stranks, and H. J. Snaith. The importance of perovskite pore filling in organometal mixed halide sensitized tio2-based solar cells. *J. Phys. Chem. Lett.*, 5(7):1096–1102, 2014.

[41] P. Roy, N. K. Sinha, S. Tiwari, and A. Khare. A review on perovskite solar cells: Evolution of architecture, fabrication techniques, commercialization issues and status. *Sol. Energy*, 198:665–688, 2020.

[42] K. Fu, A. W. Ho-Baillie, H. K. Mulmudi, and P. T. T. Trang. *Perovskite solar cells: technology and practices*. CRC Press, 2019.

[43] S. Zheng, G. Wang, T. Liu, L. Lou, S. Xiao, and S. Yang. Materials and structures for the electron transport layer of efficient and stable perovskite solar cells. *Sci. China Chem.*, 62(7):800–809, 2019.

[44] Q. Jiang, Y. Zhao, X. Zhang, X. Yang, Y. Chen, et al. Surface passivation of perovskite film for efficient solar cells. *Nat. Photonics*, 13(7):460–466, 2019.

[45] L. Lin, T. W. Jones, T. C.-J. Yang, N. W. Duffy, J. Li, et al. Inorganic electron transport materials in perovskite solar cells. *Adv. Funct. Mater.*, 31(5):2008300, 2021.

[46] Q. Jiang, X. Zhang, and J. You. SnO_2: A wonderful electron transport layer for perovskite solar cells. *Small*, 14(31):1801154, 2018.

[47] A. C. Nkele, A. C. Nwanya, N. M. Shinde, S. Ezugwu, M. Maaza, et al. The use of nickel oxide as a hole transport material in perovskite solar cell configuration: Achieving a high performance and stable device. *Int. J. Energy Res.*, 44(13):9839–9863, 2020.

[48] R. Singh, P. K. Singh, B. Bhattacharya, and H.-W. Rhee. Review of current progress in inorganic hole-transport materials for perovskite solar cells. *Appl. Mater. Today*, 14:175–200, 2019.

[49] A. A. Said, J. Xie, and Q. Zhang. Recent progress in organic electron transport materials in inverted perovskite solar cells. *Small*, 15(27):1900854, 2019.

[50] S. Pitchaiya, M. Natarajan, A. Santhanam, V. Asokan, and A. o. Yuvapragasam. A review on the classification of organic/inorganic/carbonaceous hole transporting materials for perovskite solar cell application. *Arab. J. Chem.*, 13(1):2526–2557, 2020.

[51] A. Dubey, N. Adhikari, S. Mabrouk, F. Wu, K. Chen, et al. A strategic review on processing routes towards highly efficient perovskite solar cells. *J. Mater. Chem. A*, 6(6):2406–2431, 2018.

[52] N. J. Jeon, J. H. Noh, Y. C. Kim, W. S. Yang, S. Ryu, and S. I. Seok. Solvent engineering for high-performance inorganic–organic hybrid perovskite solar cells. *Nat. Mater.*, 13(9):897–903, 2014.

[53] T. Miyadera, T. Sugita, H. Tampo, K. Matsubara, and M. Chikamatsu. Highly controlled codeposition rate of organolead halide perovskite by laser evaporation method. *ACS Appl. Mater. Interfaces*, 8(39):26013–26018, 2016.

[54] A. Giuri, S. Masi, A. Listorti, G. Gigli, S. Colella, et al. Polymeric rheology modifier allows single-step coating of perovskite ink for highly efficient and stable solar cells. *Nano Energy*, 54:400–408, 2018.

[55] L. Gil-Escrig, C. Dreessen, I. C. Kaya, B.-S. Kim, F. Palazon, M. Sessolo, and H. J. Bolink. Efficient vacuum-deposited perovskite solar cells with stable cubic $FA_{1-x}MA_xPbI_3$. *ACS Energy Lett.*, 5(9):3053–3061, 2020.

[56] Z. Wang, L. Zeng, C. Zhang, Y. Lu, S. Qiu, et al. Rational interface design and morphology control for blade-coating efficient flexible perovskite solar cells with a record fill factor of 81%. *Adv. Funct. Mater.*, 30(32):2001240, 2020.

[57] A. Yi, S. Chae, H. Lee, and H. J. Kim. The synergistic effect of cooperating solvent vapor annealing for high-efficiency planar inverted perovskite solar cells. *J. Mater. Chem. A*, 7(48):27267–27277, 2019.

[58] N. Ahn, D.-Y. Son, I.-H. Jang, S. M. Kang, M. Choi, and N.-G. Park. Highly reproducible perovskite solar cells with average efficiency of 18.3% and best efficiency of 19.7% fabricated via lewis base adduct of lead (II) iodide. *J. Am. Chem. Soc*, 137(27):8696–8699, 2015.

[59] M. Roß, L. Gil-Escrig, A. Al-Ashouri, P. Tockhorn, M. Jŏst, et al. Co-evaporated pin perovskite solar cells beyond 20% efficiency: Impact of substrate temperature and hole-transport layer. *ACS Appl. Mater. Interfaces*, 12(35):39261–39272, 2020.

[60] Y. Galagan. Perovskite solar cells: toward industrial-scale methods. *J. Phys. Chem. Lett.*, 9(15):4326–4335, 2018.

[61] J. Burschka, N. Pellet, S.-J. Moon, R. Humphry-Baker, P. Gao, et al. Sequential deposition as a route to high-performance perovskite-sensitized solar cells. *Nature*, 499(7458):316–319, 2013.

[62] J. B. Patel, R. L. Milot, A. D. Wright, L. M. Herz, and M. B. Johnston. Formation dynamics of $CH_3NH_3PbI_3$ perovskite following two-step layer deposition. *J. Phys. Chem. Lett.*, 7(1):96–102, 2016.

[63] S. Yuan, Z. Qiu, C. Gao, H. Zhang, Y. Jiang, et al. High-quality perovskite films grown with a fast solvent-assisted molecule inserting strategy for highly efficient and stable solar cells. *ACS Appl. Mater. Interfaces*, 8(34):22238–22245, 2016.

[64] Y. Wang, Y. Liu, Y. Xu, C. Zhang, H. Bao, et al. $(CH_3NH_3)_3Bi_2I_9$ perovskite films fabricated via a two-stage electric-field-assisted reactive deposition method for solar cells application. *Electrochim. Acta*, 329:135173, 2020.

[65] C. M. Sutter-Fella, Y. Li, M. Amani, J. W. Ager III, F. M. Toma, et al. High photoluminescence quantum yield in band gap tunable bromide containing mixed halide perovskites. *Nano lett.*, 16(1):800–806, 2016.

[66] J. Bing, S. Huang, and A. W. Ho-Baillie. A review on halide perovskite film formation by sequential solution processing for solar cell applications. *Energy Technol.*, 8(4):1901114, 2020.

[67] R. Liu and K. Xu. Solvent engineering for perovskite solar cells: a review. *Micro Nano Lett.*, 15(6):349–353, 2020.

[68] F. Gao, Y. Zhao, X. Zhang, and J. You. Recent progresses on defect passivation toward efficient perovskite solar cells. *Adv. Energy Mater*, 10(13):1902650, 2020.

[69] H.-S. Kim, A. Hagfeldt, and N.-G. Park. Morphological and compositional progress in halide perovskite solar cells. *ChemComm*, 55(9):1192–1200, 2019.

[70] C. M. Wolff, L. Canil, C. Rehermann, N. Ngoc Linh, F. Zu, et al. Perfluorinated self-assembled monolayers enhance the stability and ffficiency of inverted perovskite solar cells. *ACS nano*, 14(2):1445–1456, 2020.

[71] F. Ansari, E. Shirzadi, M. Salavati-Niasari, T. LaGrange, K. Nonomura, et al. A passivation mechanism exploiting surface dipoles affords high-performance perovskite solar cells. *J. Am. Chem. Soc.*, 2020.

[72] S. Rühle. Tabulated values of the Shockley–Queisser limit for single junction solar cells. *Sol. Energy*, 130:139–147, 2016.

[73] A.-F. Castro-Méndez, J. Hidalgo, and J.-P. Correa-Baena. The role of grain boundaries in perovskite solar cells. *Adv. Energy Mater.*, 9(38):1901489, 2019.

[74] G.-J. A. Wetzelaer, M. Scheepers, A. M. Sempere, C. Momblona, J. Ávila, and H. J. Bolink. Trap-assisted non-radiative recombination in organic–inorganic perovskite solar cells. *Adv. Mater.*, 27(11):1837–1841, 2015.

[75] T. S. Sherkar, C. Momblona, L. Gil-Escrig, J. Ávila, M. Sessolo, et al. Recombination in perovskite solar cells: Significance of grain boundaries, interface traps, and defect ions. *ACS Energy Lett.*, 2(5):1214–1222, 2017.

[76] J. M. Azpiroz, E. Mosconi, J. Bisquert, and F. De Angelis. Defect migration in methylammonium lead iodide and its role in perovskite solar cell operation. *Energy Environ. Sci*, 8(7):2118–2127, 2015.

[77] C. Eames, J. M. Frost, P. R. Barnes, B. C. O'regan, A. Walsh, et al. Ionic transport in hybrid lead iodide perovskite solar cells. *Nat. Commun.*, 6:7497, 2015.

[78] J. M. Frost and A. Walsh. What is moving in hybrid halide perovskite solar cells? *Acc. Chem. Res.*, 49(3):528–535, 2016.

[79] H. J. Snaith, A. Abate, J. M. Ball, G. E. Eperon, T. Leijtens, et al. Anomalous hysteresis in perovskite solar cells. *J. Phys. Chem. Lett.*, 5(9):1511–1515, 2014.

[80] F. Wu, R. Pathak, and Q. Qiao. Origin and alleviation of J-V hysteresis in perovskite solar cells: A short review. *Catal. Today*, 2021. `doi:10.1016/j.cattod.2020.12.025`.

[81] J.-W. Lee, S.-G. Kim, S.-H. Bae, D.-K. Lee, O. Lin, et al. The interplay between trap density and hysteresis in planar heterojunction perovskite solar cells. *Nano Lett.*, 17(7):4270–4276, 2017.

[82] P. Calado, A. M. Telford, D. Bryant, X. Li, J. Nelson, et al. Evidence for ion migration in hybrid perovskite solar cells with minimal hysteresis. *Nat. Commun.*, 7:13831, 2016.

[83] J. Wei, H. Li, Y. Zhao, W. Zhou, R. Fu, et al. Suppressed hysteresis and improved stability in perovskite solar cells with conductive organic network. *Nano Energy*, 26:139–147, 2016.

[84] G. Richardson, S. E. O'Kane, R. G. Niemann, T. A. Peltola, J. M. Foster, et al. Can slow-moving ions explain hysteresis in the current–voltage curves of perovskite solar cells? *Energy Environ. Sci.*, 9(4):1476–1485, 2016.

[85] L. Xu, R. M. Imenabadi, W. G. Vandenberghea, and J. W. P. Hsu. Minimizing performance degradation induced by interfacial recombination in perovskite solar cells through tailoring of the transport layer electronic properties. *APL Mater.*, 6(3):036104, 2018.

[86] T. Minemoto and M. Murata. Theoretical analysis on effect of band offsets in perovskite solar cells. *Sol. Energy Mater Sol. Cells*, 133:8–14, 2015.

[87] T. S. Sherkar, C. Momblona, L. Gil-Escrig, H. J. Bolink, and L. J. A. Koster. Improving perovskite solar cells: Insights from a validated device model. *Adv. Energy Mater.*, 7(13):1602432, 2017.

[88] M. Jošt, L. Kegelmann, L. Korte, and S. Albrecht. Monolithic perovskite tandem solar cells: A review of the present status and advanced characterization methods toward 30% efficiency. *Adv. Energy Mater.*, 10(26):1904102, 2020.

[89] Z. Fang, Q. Zeng, C. Zuo, L. Zhang, H. Xiao, M. Cheng, et al. Perovskite-based tandem solar cells. *Sci. Bull.*, 66(6):621–636, 2021.

[90] Z. Wang, Z. Song, Y. Yan, S. Liu, and D. Yang. Perovskite-a perfect top cell for tandem devices to break the S–Q limit. *Adv. Sci.*, 6(7):1801704, 2019.

[91] M. I. H. Ansari, A. Qurashi, and M. K. Nazeeruddin. Frontiers, opportunities, and challenges in perovskite solar cells: A critical review. *J. Photochem. Photobiol. C*, 35:1–24, 2018.

[92] B. Conings, J. Drijkoningen, N. Gauquelin, A. Babayigit, J. D'Haen, et al. Intrinsic thermal instability of methylammonium lead trihalide perovskite. *Adv. Energy Mater.*, 5(15):1500477, 2015.

[93] Q. Wali, F. J. Iftikhar, M. E. Khan, A. Ullah, Y. Iqbal, and R. Jose. Advances in stability of perovskite solar cells. *Org. Electron.*, 78:105590, 2020.

[94] K. Domanski, B. Roose, T. Matsui, M. Saliba, S.-H. Turren-Cruz, et al. Migration of cations induces reversible performance losses over day/ night cycling in perovskite solar cells. *Energy Environ. Sci*, 10(2):604–613, 2017.

[95] J.-P. Correa-Baena, M. Anaya, G. Lozano, W. Tress, K. Domanski, et al. Unbroken perovskite: Interplay of morphology, electro-optical properties, and ionic movement. *Adv. Mater.*, 28(25):5031–5037, 2016.

[96] W. Tress, N. Marinova, T. Moehl, S. M. Zakeeruddin, M. K. Nazeeruddin, and M. Grätzel. Understanding the rate-dependent J–V hysteresis, slow time component, and aging in $CH_3NH_3PbI_3$ perovskite solar cells: the role of a compensated electric field. *Energy Environ. Sci*, 8(3):995–1004, 2015.

[97] S. M. Sze and K. K. Ng. *Physics of semiconductor devices*. John wiley & sons, 2006.

[98] S. Altazin, C. Kirsch, E. Knapp, A. Stous, and B. Ruhstaller. Refined drift-diffusion model for the simulation of charge transport across layer interfaces in organic semiconductor devices. *J. Appl. Phys.*, 124(13):135501, 2018.

[99] I. Pisarenko and E. Ryndin. Drift-diffusion simulation of high-speed optoelectronic devices. *Electronics*, 8(1):106, 2019.

[100] A. Singh, E. Radicchi, S. Fantacci, F. Nunzi, F. De Angelis, et al. Interface electrostatics of solid-state dye-sensitized solar cells: A joint drift-diffusion and density functional theory study. *J. Phys. Chem. C*, 123(24):14955–14963, 2019.

[101] A. Singh and A. Gagliardi. Efficiency of all-perovskite two-terminal tandem solar cells: A drift-diffusion study. *Sol. Energy*, 187:39–46, 2019.

[102] D. Rossi, F. Santoni, M. A. Der Maur, and A. Di Carlo. A multiparticle drift-diffusion model and its application to organic and inorganic electronic device simulation. *IEEE Trans. Electron Devices*, 66(6):2715–2722, 2019.

[103] T. Kirchartz, J. A. Márquez, M. Stolterfoht, and T. Unold. Photoluminescence-based characterization of halide perovskites for photovoltaics. *Adv. Energy Mater.*, 10(26):1904134, 2020.

[104] K. A. Bush, K. Frohna, R. Prasanna, R. E. Beal, T. Leijtens, et al. Compositional engineering for efficient wide band gap perovskites with improved stability to photoinduced phase segregation. *ACS Energy Lett.*, 3(2):428–435, 2018.

[105] J. You, Z. Hong, Y. Yang, Q. Chen, M. Cai, et al. Low-temperature solution-processed perovskite solar cells with high efficiency and flexibility. *ACS nano*, 8(2):1674–1680, 2014.

[106] A. De Vos. Detailed balance limit of the efficiency of tandem solar cells. *J. Phys. D: Appl. Phys.*, 13(5):839, 1980.

[107] M. C. Schubert, L. E. Mundt, D. Walter, A. Fell, and S. W. Glunz. Spatially resolved performance analysis for perovskite solar cells. *Adv. Energy Mater.*, 10(26):1904001, 2020.

[108] W. Tress, N. Marinova, O. Inganäs, M. K. Nazeeruddin, S. M. Zakeeruddin, et al. Predicting the open-circuit voltage of $CH_3NH_3PbI_3$ perovskite solar cells using electroluminescence and photovoltaic quantum efficiency spectra: the role of radiative and non-radiative recombination. *Adv. Energy Mater.*, 5(3):1400812, 2015.

[109] S. van Reenen, M. Kemerink, and H. J. Snaith. Modeling anomalous hysteresis in perovskite solar cells. *J. Phys. Chem. Lett.*, 6(19):3808–3814, 2015.

[110] N. E. Courtier, J. M. Cave, J. M. Foster, A. B. Walker, and G. Richardson. How transport layer properties affect perovskite solar cell performance: insights from a coupled charge transport/ion migration model. *Energy Environ. Sci.*, 12(1):396–409, 2019.

[111] M. T. Neukom, A. Schiller, S. Züfle, E. Knapp, J. Ávila, et al. Consistent device simulation model describing perovskite solar cells in steady-state, transient, and frequency domain. *ACS Appl. Mater. Interfaces*, 11(26):23320–23328, 2019.

[112] Q. Zhou, D. Jiao, K. Fu, X. Wu, Y. Chen, et al. Two-dimensional device modeling of $CH_3NH_3PbI_3$ based planar heterojunction perovskite solar cells. *Sol. Energy*, 123:51–56, 2016.

[113] A. Gagliardi, M. A. der Maur, D. Gentilini, F. di Fonzo, A. Abrusci, and et al. The real TiO_2/HTM interface of solid-state dye solar cells: role of trapped states from a multiscale modelling perspective. *Nanoscale*, 7(3):1136–1144, 2015.

[114] M. A. der Maur, G. Penazzi, G. Romano, F. Sacconi, A. Pecchia, and A. Di Carlo. The multiscale paradigm in electronic device simulation. *IEEE Trans. Electron Devices*, 58(5):1425–1432, 2011.

[115] W. Shockley and W. Read Jr. Statistics of the recombinations of holes and electrons. *Phys. Rev.*, 87(5):835, 1952.

[116] R. Hall. Germanium rectifier characteristics. *Phys. Rev.*, 83(1):228–228, 1951.

[117] S. Selberherr. *Analysis and simulation of semiconductor devices*. Springer Science & Business Media, 2012.

[118] J. Simmons and G. Taylor. Nonequilibrium steady-state statistics and associated effects for insulators and semiconductors containing an arbitrary distribution of traps. *Phys. Rev. B*, 4(2):502, 1971.

[119] Y. Zhou, Z. Zhou, M. Chen, Y. Zong, J. Huang, et al. Doping and alloying for improved perovskite solar cells. *J. Mater. Chem. A*, 4(45):17623–17635, 2016.

[120] S. Foster, F. Deledalle, A. Mitani, T. Kimura, K.-B. Kim, et al. Electron collection as a limit to polymer: PCBM solar cell efficiency: effect of blend microstructure on carrier mobility and device performance in PTB7: PCBM. *Adv. Energy. Mater.*, 4(14):1400311, 2014.

[121] S. Cheylan, J. Puigdollers, H. J. Bolink, E. Coronado, C. Voz, et al. Increased conductivity of a hole transport layer due to oxidation by a molecular nanomagnet. *J. Appl. Phys.*, 103:096110, 2008.

[122] F. Brivio, K. T. Butler, A. Walsh, and M. Van Schilfgaarde. Relativistic quasi-particle self-consistent electronic structure of hybrid halide perovskite photovoltaic absorbers. *Phys. Rev. B*, 89(15):155204, 2014.

[123] V. D. Mihailetchi, J. K. van Duren, P. W. Blom, J. C. Hummelen, R. A. Janssen, et al. Electron transport in a methanofullerene. *Adv. Funct. Mater.*, 13(1):43–46, 2003.

[124] H. Wang, X. Wang, P. Fan, X. Yang, and J. Yu. Enhanced power conversion efficiency of P3HT: PC71BM bulk heterojunction polymer solar cells by doping a high-mobility small organic molecule. *Int. j. photoenergy*, 2015, 2015.

[125] F. Arca, M. Loch, and P. Lugli. Enhancing efficiency of organic bulkheterojunction solar cells by using 1,8-diiodooctane as processing additive. *IEEE J. Photovolt.*, 4(6):1560–1565, 2014.

[126] O. Malinkiewicz, A. Yella, Y. H. Lee, G. M. Espallargas, M. Graetzel, et al. Perovskite solar cells employing organic charge-transport layers. *Nat. Photonics*, 8(2):128, 2014.

[127] J.-W. Lee, S.-H. Bae, N. De Marco, Y.-T. Hsieh, Z. Dai, and Y. Yang. The role of grain boundaries in perovskite solar cells. *Mater. Today Energy*, 7:149–160, 2018.

[128] H. Dong, J. Xi, L. Zuo, J. Li, Y. Yang, et al. Conjugated molecules "bridge": Functional ligand toward highly efficient and long-term stable perovskite solar cell. *Adv. Funct. Mater.*, 29(17):1808119, 2019.

[129] L. Qiu, S. He, L. K. Ono, et al. Progress of surface science studies on ABX_3-based metal halide perovskite solar cells. *Adv. Energy Mater.*, 10(13):1902726, 2020.

[130] Z. Wu, Z. Liu, Z. Hu, Z. Hawash, L. Qiu, et al. Highly efficient and stable perovskite solar cells via modification of energy levels at the perovskite/carbon electrode interface. *Adv. Mater.*, 31(11):1804284, 2019.

[131] X. Zhang, Y. Sun, M. Wang, H. Cui, W. Xie, et al. Facilitating electron collection of organic photovoltaics by passivating trap states and tailoring work function. *Sol. Energy*, 181:9–16, 2019.

[132] T. Chen, G. Tong, E. Xu, H. Li, P. Li, et al. Accelerating hole extraction by inserting 2D Ti_3C_2−MXene interlayer to all inorganic perovskite solar cells with long-term stability. *J. Mater. Chem. A*, 7(36):20597–20603, 2019.

[133] J. Xie, K. Yan, H. Zhu, G. Li, H. Wang, et al. Identifying the functional groups effect on passivating perovskite solar cells. *Sci. Bull.*, 65(20):1726–1734, 2020.

[134] L. Canil, T. Cramer, B. Fraboni, D. Ricciarelli, D. Meggiolaro, et al. Tuning halide perovskite energy levels. *Energy Environ. Sci.*, 14:1429–1438, 2021.

[135] W.-J. Yin, H. Chen, T. Shi, S.-H. Wei, and Y. Yan. Origin of high electronic quality in structurally disordered $CH_3NH_3PbI_3$ and the passivation effect of Cl and O at grain boundaries. *Adv. Electron. Mater.*, 1(6):1500044, 2015.

[136] M. B. Johnston and L. M. Herz. Hybrid perovskites for photovoltaics: Charge-carrier recombination, diffusion, and radiative efficiencies. *Acc. Chem. Res.*, 49(1):146–154, 2016.

[137] Y. Shao, Y. Fang, T. Li, Q. Wang, Q. Dong, et al. Grain boundary dominated ion migration in polycrystalline organic–inorganic halide perovskite films. *Energy Environ. Sci*, 9(5):1752–1759, 2016.

[138] J. Xing, Q. Wang, Q. Dong, Y. Yuan, Y. Fang, and J. Huang. Ultrafast ion migration in hybrid perovskite polycrystalline thin films under light and suppression in single crystals. *Phys. Chem. Chem. Phys.*, 18(44):30484–30490, 2016.

[139] B. Roose, A. Ummadisingu, J.-P. Correa-Baena, M. Saliba, A. Hagfeldt, et al. Spontaneous crystal coalescence enables highly efficient perovskite solar cells. *Nano Energy*, 39:24–29, 2017.

[140] M. Stolterfoht, C. M. Wolff, J. A. Márquez, S. Zhang, C. J. Hages, et al. Visualization and suppression of interfacial recombination for high-efficiency large-area pin perovskite solar cells. *Nat. Energy*, 3(10):847–854, 2018.

[141] C. Liu, Z. Huang, X. Hu, X. Meng, L. Huang, et al. Grain boundary modification via F4TCNQ to reduce defects of perovskite solar cells with excellent device performance. *ACS Appl. Mater. Interfaces*, 10(2):1909–1916, 2018.

[142] M. Ameri, M. Ghaffarkani, R. T. Ghahrizjani, N. Safari, and E. Mohajerani. Phenomenological morphology design of hybrid organic-inorganic perovskite solar cell for high efficiency and less hysteresis. *Sol. Energy Mater. Sol. Cells*, 205:110251, 2020.

[143] B. Olyaeefar, S. Ahmadi-Kandjani, and A. Asgari. Classical modelling of grain size and boundary effects in polycrystalline perovskite solar cells. *Sol. Energy Mater. Sol. Cells*, 180:76–82, 2018.

[144] A. Singh and A. Gagliardi. Role of ion-assisted recombination and grain boundaries in perovskite solar cell hysteresis and efficiency. In *2020 IEEE 20th International Conference on Nanotechnology (IEEE-NANO)*, pages 227–232. IEEE, 2020.

[145] J. I. Pankove. *Optical processes in semiconductors*. Courier Corporation, 1975.

[146] J. M. Ball, S. D. Stranks, M. T. Hörantner, S. Hüttner, W. Zhang, et al. Optical properties and limiting photocurrent of thin-film perovskite solar cells. *Energy Environ. Sci.*, 8(2):602–609, 2015.

[147] C. Zhang, W. Luan, and Y. Yin. High efficient planar-heterojunction perovskite solar cell based on two-step deposition process. *Energy Procedia*, 105:793–798, 2017.

[148] P. Tiwana, P. Docampo, M. B. Johnston, H. J. Snaith, and L. M. Herz. Electron mobility and injection dynamics in mesoporous ZnO, SnO_2, and TiO_2 films used in dye-sensitized solar cells. *ACS Nano*, 5(6):5158–5166, 2011.

[149] A. Wypych, I. Bobowska, M. Tracz, A. Opasinska, S. Kadlubowski, et al. Dielectric properties and characterisation of titanium dioxide obtained by different chemistry methods. *J. Nanomater.*, 2014, 2014.

[150] Z. Li, J. Chen, H. Li, Q. Zhang, Z. Chen, X. Zheng, et al. A facilely synthesized 'spiro' hole-transporting material based on spiro [3.3] heptane-2, 6-dispirofluorene for efficient planar perovskite solar cells. *RSC Adv.*, 7(66):41903–41908, 2017.

[151] A. J. Moulé, H. J. Snaith, M. Kaiser, H. Klesper, D. M. Huang, et al. Optical description of solid-state dye-sensitized solar cells. I. Measurement of layer optical properties. *J. Appl. Phys.*, 106(7):073111, 2009.

[152] T. Leijtens, J. Lim, J. Teuscher, T. Park, and H. J. Snaith. Charge density dependent mobility of organic hole-transporters and mesoporous TiO_2 determined by transient mobility spectroscopy: Implications to dye-sensitized and organic solar cells. *Adv. Mat.*, 25(23):3227–3233, 2013.

[153] N.-G. Park. Perovskite solar cells: An emerging photovoltaic technology. *Mater. Today*, 18(2):65–72, 2015.

[154] H. Mehrer. *Diffusion in solids: Fundamentals, methods, materials, diffusion-controlled processes*, volume 155. Springer Science & Business Media, 2007.

[155] M. H. Futscher, J. M. Lee, L. McGovern, L. A. Muscarella, T. Wang, et al. Quantification of ion migration in $CH_3NH_3PbI_3$ perovskite solar cells by transient capacitance measurements. *Mater. Horiz.*, 6(7):1497–1503, 2019.

[156] J. Haruyama, K. Sodeyama, L. Han, and Y. Tateyama. First-principles study of ion diffusion in perovskite solar cell sensitizers. *J. Am. Chem. Soc.*, 137(32):10048–10051, 2015.

[157] J. Wei, Y. Zhao, H. Li, G. Li, J. Pan, et al. Hysteresis analysis based on the ferroelectric effect in hybrid perovskite solar cells. *J. Phys. Chem. Lett.*, 5(21):3937–3945, 2014.

[158] J. M. Frost, K. T. Butler, and A. Walsh. Molecular ferroelectric contributions to anomalous hysteresis in hybrid perovskite solar cells. *APL Mater.*, 2(8):081506, 2014.

[159] B. Wu, K. Fu, N. Yantara, G. Xing, S. Sun, et al. Charge accumulation and hysteresis in perovskite-based solar cells: An electro-optical analysis. *Adv. Energy Mater.*, 5(19):1500829, 2015.

[160] S. A. L. Weber, I. M. Hermes, S.-H. Turren-Cruz, C. Gort, V. W. Bergmann, et al. How the formation of interfacial charge causes hysteresis in perovskite solar cells. *Energy Environ. Sci.*, 11(9):2404–2413, 2018.

[161] Y. Rong, Y. Hu, S. Ravishankar, H. Liu, X. Hou, et al. Tunable hysteresis effect for perovskite solar cells. *Energy Environ. Sci.*, 10:2383–2391, 2017.

[162] H. Imran and N. Z. Butt. Investigation of dominant hysteresis phenomenon in perovskite solar cell. In *2016 IEEE 43rd Photovoltaic Specialists Conference (PVSC)*, pages 0776–0780, June 2016. doi:10.1109/PVSC.2016.7749709.

[163] Y. Shao, Z. Xiao, C. Bi, Y. Yuan, and J. Huang. Origin and elimination of photocurrent hysteresis by fullerene passivation in $CH_3NH_3PbI_3$ planar heterojunction solar cells. *Nat. Commun.*, 5:5784, 2014.

[164] J. Beilsten-Edmands, G. Eperon, R. Johnson, H. Snaith, and P. Radaelli. Non-ferroelectric nature of the conductance hysteresis in $CH_3NH_3PbI_3$ perovskite-based photovoltaic devices. *Appl. Phys. Lett.*, 106(17):173502, 2015.

[165] Z. Fan, J. Xiao, K. Sun, L. Chen, Y. Hu, et al. Ferroelectricity of $CH_3NH_3PbI_3$ perovskite. *J. Phys. Chem. Lett.*, 6(7):1155–1161, 2015.

[166] A. M. Leguy, J. M. Frost, A. P. McMahon, V. G. Sakai, W. Kockelmann, et al. The dynamics of methylammonium ions in hybrid organic–inorganic perovskite solar cells. *Nat. Commun.*, 6(1):1–11, 2015.

[167] S. Meloni, T. Moehl, W. Tress, M. Franckevičius, M. Saliba, et al. Ionic polarization-induced current–voltage hysteresis in $CH_3NH_3PbX_3$ perovskite solar cells. *Nat. Commun.*, 7(1):1–9, 2016.

[168] C. Li, A. Guerrero, Y. Zhong, A. Gräser, C. A. M. Luna, et al. Real-time observation of iodide ion migration in methylammonium lead halide perovskites. *Small*, 13(42):1701711, 2017.

[169] W. Peng, C. Aranda, O. M. Bakr, G. Garcia-Belmonte, J. Bisquert, and A. Guerrero. Quantification of ionic diffusion in lead halide perovskite single crystals. *ACS Energy Lett.*, 3(7):1477–1481, 2018.

[170] T. Zhang, H. Chen, Y. Bai, S. Xiao, L. Zhu, et al. Understanding the relationship between ion migration and the anomalous hysteresis in high-efficiency perovskite solar cells: A fresh perspective from halide substitution. *Nano Energy*, 26:620–630, 2016.

[171] G. Xia, B. Huang, Y. Zhang, X. Zhao, C. Wang, et al. Nanoscale insights into photovoltaic hysteresis in triple-cation mixed-halide perovskite: Resolving the role of polarization and ionic migration. *Adv. Mater.*, 31(36):1902870, 2019.

[172] I. Zarazua, J. Bisquert, and G. Garcia-Belmonte. Light-induced space-charge accumulation zone as photovoltaic mechanism in perovskite solar cells. *J. Phys. Chem. Lett.*, 7(3):525–528, 2016.

[173] G. Nagabhushana, R. Shivaramaiah, and A. Navrotsky. Direct calorimetric verification of thermodynamic instability of lead halide hybrid perovskites. *Proc. Natl. Acad. Sci.*, 113(28):7717–7721, 2016.

[174] W.-J. Yin, T. Shi, and Y. Yan. Unusual defect physics in $CH_3NH_3PbI_3$ perovskite solar cell absorber. *Appl. Phys. Lett.*, 104(6):063903, 2014.

[175] A. Buin, P. Pietsch, J. Xu, O. Voznyy, A. H. Ip, et al. Materials processing routes to trap-free halide perovskites. *Nano Lett.*, 14(11):6281–6286, 2014.

[176] A. Walsh, D. O. Scanlon, S. Chen, X. Gong, and S.-H. Wei. Self-regulation mechanism for charged point defects in hybrid halide perovskites. *Angew. Chem. Int. Ed.*, 54(6):1791–1794, 2015.

[177] Z. Xiao, Y. Yuan, Y. Shao, Q. Wang, Q. Dong, et al. Giant switchable photovoltaic effect in organometal trihalide perovskite devices. *Nat. Mater.*, 14(2):193, 2015.

[178] V. Adinolfi, M. Yuan, R. Comin, E. S. Thibau, D. Shi, et al. The in-gap electronic state spectrum of methylammonium lead iodide single-crystal perovskites. *Adv. Mater.*, 28(17):3406–3410, 2016.

[179] S. Heo, G. Seo, Y. Lee, D. Lee, M. Seol, et al. Deep level trapped defect analysis in $CH_3NH_3PbI_3$ perovskite solar cells by deep level transient spectroscopy. *Energy Environ. Sci.*, 10(5):1128–1133, 2017.

[180] E. Mosconi and F. De Angelis. Mobile ions in organohalide perovskites: Interplay of electronic structure and dynamics. *ACS Energy Lett.*, 1(1):182–188, 2016.

[181] D. Meggiolaro, D. Ricciarelli, A. A. Alasmari, F. A. Alasmary, and F. De Angelis. Tin versus lead redox chemistry modulates charge trapping and self-doping in tin/lead iodide perovskites. *J. Phys. Chem. Lett.*, 11(9):3546–3556, 2020.

[182] D. Meggiolaro and F. De Angelis. First-principles modeling of defects in lead halide perovskites: best practices and open issues. *ACS Energy Lett.*, 3(9):2206–2222, 2018.

[183] A. Gagliardi and A. Abate. Mesoporous electron-selective contacts enhance the tolerance to interfacial ion accumulation in perovskite solar cells. *ACS Energy Lett.*, 3(1):163–169, 2017.

[184] P. Calado, I. Gelmetti, and P. R. Barnes. Driftfusion (version v1.0.0). zenodo., 2020. URL: `https://doi.org/10.5281/zenodo.3670155`.

[185] A. Singh, W. Kaiser, and A. Gagliardi. Role of cation-mediated recombination in perovskite solar cells. *Sol. Energy Mater Sol.*, 221:110912, 2021.

[186] P. Lopez-Varo, J. A. Jiménez-Tejada, M. García-Rosell, S. Ravishankar, G. Garcia-Belmonte, et al. Device physics of hybrid perovskite solar cells: theory and experiment. *Adv. Energy Mater*, 8(14):1702772, 2018.

[187] S. N. Habisreutinger, N. K. Noel, and H. J. Snaith. Hysteresis index: A figure without merit for quantifying hysteresis in perovskite solar cells. *ACS Energy Lett.*, 3(10):2472–2476, 2018.

[188] M. H. Futscher, M. K. Gangishetty, D. N. Congreve, and B. Ehrler. Quantifying mobile ions and electronic defects in perovskite-based devices with temperature-dependent capacitance measurements: Frequency vs time domain. *J. Chem. Phys.*, 152(4):044202, 2020.

[189] J.-S. Park, J. Calbo, Y.-K. Jung, L. D. Whalley, and A. Walsh. Accumulation of deep traps at grain boundaries in halide perovskites. *ACS Energy Lett.*, 4(6):1321–1327, 2019.

[190] L. Bertoluzzi, C. C. Boyd, N. Rolston, J. Xu, R. Prasanna, et al. Mobile ion concentration measurement and open-access band diagram simulation platform for halide perovskite solar cells. *Joule*, 4(1):109–127, 2020.

[191] R. Gottesman, P. Lopez-Varo, L. Gouda, J. A. Jimenez-Tejada, J. Hu, S. Tirosh, et al. Dynamic phenomena at perovskite/electron-selective contact interface as interpreted from photovoltage decays. *Chem*, 1(5):776–789, 2016.

[192] M.-H. Du. Density functional calculations of native defects in $CH_3NH_3PbI_3$: effects of spin–orbit coupling and self-interaction error. *J. Phys. Chem. Lett.*, 6(8):1461–1466, 2015.

[193] L. Bertoluzzi, R. A. Belisle, K. A. Bush, R. Cheacharoen, M. D. McGehee, and B. C. O'Regan. In situ measurement of electric-field screening in hysteresis-free PTAA/$FA_{0.83}Cs_{0.17}Pb(I_{0.83}Br_{0.17})_3$/$C_{60}$ perovskite solar cells gives an ion mobility of 3×10^{-7} $cm^2/(vs)$, 2 orders of magnitude faster than reported for metal-oxide-contacted perovskite cells with hysteresis. *J. Am. Chem. Soc.*, 140(40):12775–12784, 2018.

[194] T. Hwang, A. J. Yun, J. Kim, D. Cho, S. Kim, et al. Electronic traps and their correlations to perovskite solar cell performance via compositional and thermal annealing controls. *ACS Appl. Mater. Interfaces*, 11(7):6907–6917, 2019.

[195] D. Hong, Y. Zhou, S. Wan, X. Hu, D. Xie, and Y. Tian. Nature of photoinduced quenching traps in methylammonium lead triiodide perovskite revealed by reversible photoluminescence decline. *ACS Photonics*, 5(5):2034–2043, 2018.

[196] S. H. Kim and D. Lee. Role of charge-trapping iodine frenkel defects for hysteresis in organic–inorganic hybrid perovskite from first-principles calculations. *J. Phys. Chem. C*, 123(14):9629–9633, 2019.

[197] A. Buin, R. Comin, J. Xu, A. H. Ip, and E. H. Sargent. Halide-dependent electronic structure of organolead perovskite materials. *Chem. Mater.*, 27(12):4405–4412, 2015.

[198] M. L. Agiorgousis, Y.-Y. Sun, H. Zeng, and S. Zhang. Strong covalency-induced recombination centers in perovskite solar cell material $CH_3NH_3PbI_3$. *J. Am. Chem. Soc.*, 136(41):14570–14575, 2014.

[199] T. Leijtens, S. D. Stranks, G. E. Eperon, R. Lindblad, E. M. Johansson, et al. Electronic properties of meso-superstructured and planar organometal halide perovskite films: Charge trapping, photodoping, and carrier mobility. *ACS nano*, 8(7):7147–7155, 2014.

[200] F. Xu, J. Zhu, R. Cao, S. Ge, W. Wang, et al. Elucidating the evolution of the current-voltage characteristics of planar organometal halide perovskite solar cells to an S-shape at low temperature. *Sol. Energy Mater. Sol. Cells*, 157:981–988, 2016.

[201] X. Zhang, M. E. Turiansky, J.-X. Shen, and C. G. Van de Walle. Iodine interstitials as a cause of nonradiative recombination in hybrid perovskites. *Phys. Rev. B*, 101(14):140101, 2020.

[202] G. Tumen-Ulzii, T. Matsushima, D. Klotz, M. R. Leyden, P. Wang, et al. Hysteresis-less and stable perovskite solar cells with a self-assembled monolayer. *Comm. Mater.*, 1(1):1–7, 2020.

[203] F. Sadegh, S. Akin, M. Moghadam, V. Mirkhani, M. A. Ruiz-Preciado, et al. Highly efficient, stable and hysteresis–less planar perovskite solar cell based on chemical bath treated Zn_2SnO_4 electron transport layer. *Nano Energy*, 75:105038, 2020.

[204] M. Valles-Pelarda, B. C. Hames, I. García-Benito, O. Almora, A. Molina-Ontoria, et al. Analysis of the hysteresis behavior of perovskite solar cells with interfacial fullerene self-assembled monolayers. *J. Phys. Chem. Lett.*, 7(22):4622–4628, 2016.

[205] W. Huang, J. S. Manser, P. V. Kamat, and S. Ptasinska. Evolution of chemical composition, morphology, and photovoltaic efficiency of $CH_3NH_3PbI_3$ perovskite under ambient conditions. *Chem. Mater.*, 28(1):303–311, 2016.

[206] P. Colter, B. Hagar, and S. Bedair. Tunnel junctions for III-V multijunction solar cells review. *Crystals*, 8(12):445, 2018.

[207] D. A. Egger, A. Bera, D. Cahen, G. Hodes, T. Kirchartz, L. Kronik, et al. What remains unexplained about the properties of halide perovskites? *Adv. Mater.*, 30(20):1800691, 2018.

[208] M. Anaya, G. Lozano, M. E. Calvo, and H. Míguez. ABX_3 perovskites for tandem solar cells. *Joule*, 1(4):769–793, 2017.

[209] L. Mazzarella, Y.-H. Lin, S. Kirner, A. B. Morales-Vilches, L. Korte, et al. Infrared light management using a nanocrystalline silicon oxide interlayer in monolithic perovskite/silicon heterojunction tandem solar cells with efficiency above 25%. *Adv. Energy Mater*, 9(14):1803241, 2019.

[210] E. Lamanna, F. Matteocci, E. Calabrò, L. Serenelli, E. Salza, et al. Mechanically stacked, two-terminal graphene-based perovskite/silicon tandem solar cell with efficiency over 26%. *Joule*, 4(4):865–881, 2020.

[211] F. Sahli, J. Werner, B. A. Kamino, M. Bräuninger, R. Monnard, et al. Fully textured monolithic perovskite/silicon tandem solar cells with 25.2% power conversion efficiency. *Nat. Mater.*, 17(9):820, 2018.

[212] J. Werner, B. Niesen, and C. Ballif. Perovskite/silicon tandem solar cells: Marriage of convenience or true love story? – An overview. *Adv. Mater. Interfaces*, 5(1):1700731, 2018.

[213] M. H. Elshorbagy, E. López-Fraguas, F. A. Chaudhry, J. M. Sánchez-Pena, R. Vergaz, and B. García-Cámara. A monolithic nanostructured-perovskite/silicon tandem solar cell: feasibility of light management through geometry and materials selection. *Sci. Rep.*, 10(1):1–8, 2020.

[214] S. Xie, R. Xia, Z. Chen, J. Tian, L. Yan, et al. Efficient monolithic perovskite/organic tandem solar cells and their efficiency potential. *Nano Energy*, 78:105238, 2020.

[215] P. Wang, Y. Zhao, and T. Wang. Recent progress and prospects of integrated perovskite/organic solar cells. *Appl. Phys. Rev.*, 7(3):031303, 2020.

[216] M. Daboczi, J. Kim, J. Lee, H. Kang, I. Hamilton, et al. Towards efficient integrated perovskite/organic bulk heterojunction solar cells: Interfacial energetic requirement to reduce charge carrier recombination losses. *Adv. Funct. Mater.*, 30(25):2001482, 2020.

[217] K. Xiao, R. Lin, Q. Han, Y. Hou, Z. Qin, et al. All-perovskite tandem solar cells with 24.2% certified efficiency and area over 1 cm^2 using surface-anchoring zwitterionic antioxidant. *Nat. Energy*, 5(11):870–880, 2020.

[218] Y. Yao, F. Lv, L. Luo, L. Liao, G. Wang, et al. Highly efficient Sn–Pb perovskite solar cell and high-performance all-perovskite four-terminal tandem solar cell. *Solar RRL*, 4(3):1900396, 2020.

[219] Y. Wang, M. Zhang, K. Xiao, R. Lin, X. Luo, et al. Recent progress in developing efficient monolithic all-perovskite tandem solar cells. *J. Semicond.*, 41(5):051201, 2020.

[220] A. Rajagopal, Z. Yang, S. B. Jo, I. L. Braly, P.-W. Liang, et al. Highly efficient perovskite–perovskite tandem solar cells reaching 80% of the theoretical limit in photovoltage. *Adv. Mater.*, 29(34):1702140, 2017.

[221] D. Zhao, C. Chen, C. Wang, M. M. Junda, Z. Song, et al. Efficient two-terminal all-perovskite tandem solar cells enabled by high-quality low-bandgap absorber layers. *Nat. Energy*, 3(12):1093, 2018.

[222] G. E. Eperon, T. Leijtens, K. A. Bush, R. Prasanna, T. Green, et al. Perovskite-perovskite tandem photovoltaics with optimized band gaps. *Science*, 354(6314):861–865, 2016.

[223] X. Zheng, A. Y. Alsalloum, Y. Hou, E. H. Sargent, and O. M. Bakr. All-perovskite tandem solar cells: A roadmap to uniting high efficiency with high stability. *Acc. Mater. Res.*, 1(1):63–76, 2020.

[224] Singh, Ajay and Gagliardi, Alessio. Device simulation of all-perovskite four-terminal tandem solar cells: towards 33% efficiency. *EPJ Photovolt.*, 12:4, 2021. URL: `https://doi.org/10.1051/epjpv/2021004`, `doi:10.1051/epjpv/2021004`.

[225] M. H. Futscher and B. Ehrler. Efficiency limit of perovskite/Si tandem solar cells. *ACS Energy Lett.*, 1(4):863–868, 2016.

[226] M. Soldera, A. K. Frischknecht, and K. Taretto. Optical and electrical optimization of all-perovskite pin type junction tandem solar cells. *J. Phys. D Appl. Phys.*, 53(31):315104, 2020.

[227] N. Singh, A. Agarwal, and M. Agarwal. Numerical simulation of highly efficient lead-free all-perovskite tandem solar cell. *Sol. Energy*, 208:399–410, 2020.

[228] R. Sheng, M. T. Hörantner, Z. Wang, Y. Jiang, W. Zhang, et al. Monolithic wide band gap perovskite/perovskite tandem solar cells with organic recombination layers. *J. Phys. Chem. C*, 121(49):27256–27262, 2017.

[229] C. Liu, C. Zhang, S. Pang, H. Dong, Z. Zhang, et al. Enhancing the performance of two-terminal all-perovskite tandem solar cells by the optical coupling layer beyond the antireflection function. *IEEE Photonics J.*, 12(5):1–12, 2020.

[230] M. T. Hörantner, T. Leijtens, M. E. Ziffer, G. E. Eperon, M. G. Christoforo, et al. The potential of multijunction perovskite solar cells. *ACS Energy Lett.*, 2(10):2506–2513, 2017.

[231] J. J. Kwiatkowski, J. M. Frost, and J. Nelson. The effect of morphology on electron field-effect mobility in disordered C60 thin films. *Nano lett.*, 9(3):1085–1090, 2009.

[232] S. Kang, Y. Yi, C. Kim, S. Cho, M. Noh, et al. Energy level diagrams of C_{60}/pentacene/Au and pentacene/C_{60}/Au. *Synth. Met.*, 156(1):32–37, 2006.

[233] R. Motoyoshi, T. Oku, A. Suzuki, K. Kikuchi, S. Kikuchi, et al. Fabrication and characterization of copper system compound semiconductor solar cells. *Adv. Mater. Sci. Eng.*, 2010, 2010.

[234] A. Labrunie, J. Gorenflot, M. Babics, O. Aleveque, S. Dabos-Seignon, et al. Triphenylamine-based push–pull σ–C60 dyad as photoactive molecular material for single-component organic solar cells: Synthesis, characterizations, and photophysical properties. *Chem. Mater.*, 30(10):3474–3485, 2018.

[235] S. Joshi, M. Mudigere, L. Krishnamurthy, and G. Shekar. Growth and morphological studies of NiO/CuO/ZnO based nanostructured thin films for photovoltaic applications. *Chem. Pap.*, 68(11):1584–1592, 2014.

[236] P.-J. Liu, Z.-J. Yao, V. M. H. Ng, J.-T. Zhou, Z.-H. Yang, and L.-B. Kong. Enhanced microwave absorption properties of double-layer absorbers based on spherical NiO and $Co_{0.2}Ni_{0.4}Zn_{0.4}Fe_2O_4$ ferrite composites. *Acta Metall. Sin. (Engl. Lett.)*, 31(2):171–179, 2018.

[237] M. Ye, C. He, J. Iocozzia, X. Liu, X. Cui, et al. Recent advances in interfacial engineering of perovskite solar cells. *J. Phys. D: Appl. Phys.*, 50(37):373002, 2017.

[238] E. S. Muckley, C. B. Jacobs, K. Vidal, J. P. Mahalik, R. Kumar, et al. New insights on electro-optical response of poly (3, 4-ethylenedioxythiophene): poly (styrenesulfonate) film to humidity. *ACS Appl. Mater. Interfaces*, 9(18):15880–15886, 2017.

[239] T. Leijtens, R. Prasanna, K. A. Bush, G. E. Eperon, J. A. Raiford, et al. Tin–lead halide perovskites with improved thermal and air stability for efficient all-perovskite tandem solar cells. *Sustain. Energy Fuels*, 2(11):2450–2459, 2018.

[240] C. Zhao, B. Chen, X. Qiao, L. Luan, K. Lu, and B. Hu. Revealing underlying processes involved in light soaking effects and hysteresis phenomena in perovskite solar cells. *Adv. Energy Mater.*, 5(14):1500279, 2015.

[241] J. Kim, S.-H. Lee, J. H. Lee, and K.-H. Hong. The role of intrinsic defects in methylammonium lead iodide perovskite. *J. Phys. Chem. Lett.*, 5(8):1312–1317, 2014.

[242] O. G. Reid, M. Yang, N. Kopidakis, K. Zhu, and G. Rumbles. Grain-size-limited mobility in methylammonium lead iodide perovskite thin films. *ACS Energy Lett.*, 1(3):561–565, 2016.

[243] M.-J. Zhang, N. Wang, S.-P. Pang, Q. Lv, C.-S. Huang, et al. Carrier transport improvement of $CH_3NH_3PbI_3$ film by methylamine gas treatment. *ACS Appl. Mater. Interfaces*, 8(45):31413–31418, 2016.

[244] W. Yan, Y. Li, S. Ye, Y. Li, H. Rao, et al. Increasing open circuit voltage by adjusting work function of hole-transporting materials in perovskite solar cells. *Nano Res.*, 9(6):1600–1608, 2016.

[245] E. J. Juarez-Perez, M. Wuβler, F. Fabregat-Santiago, K. Lakus-Wollny, E. Mankel, et al. Role of the selective contacts in the performance of lead halide perovskite solar cells. *J. Phys. Chem. Lett.*, 5(4):680–685, 2014.

[246] G. Zuo, H. Abdalla, and M. Kemerink. Impact of doping on the density of states and the mobility in organic semiconductors. *Phys. Rev. B*, 93(23):235203, 2016.

[247] C. Momblona, L. Gil-Escrig, E. Bandiello, E. M. Hutter, M. Sessolo, et al. Efficient vacuum deposited p-i-n and n-i-p perovskite solar cells employing doped charge transport layers. *Energy Environ. Sci*, 9(11):3456–3463, 2016.

[248] B. Shi, L. Duan, Y. Zhao, J. Luo, and X. Zhang. Semitransparent perovskite solar cells: from materials and devices to applications. *Adv. Mater.*, 32(3):1806474, 2020.

[249] Y. Liang, Y. Wang, C. Mu, S. Wang, X. Wang, et al. Achieving high open-circuit voltages up to 1.57 v in hole-transport-material-free $MAPbBr_3$ solar cells with carbon electrodes. *Adv. Energy Mater.*, 8(4):1701159, 2018.

[250] S. Ryu, J. H. Noh, N. J. Jeon, Y. C. Kim, W. S. Yang, et al. Voltage output of efficient perovskite solar cells with high open-circuit voltage and fill factor. *Energy Environ. Sci.*, 7(8):2614–2618, 2014.

[251] W. S. Subhani, K. Wang, M. Du, X. Wang, N. Yuan, et al. Anti-solvent engineering for efficient semitransparent $CH_3NH_3PbBr_3$ perovskite solar cells for greenhouse applications. *J. Energy Chem.*, 34:12–19, 2019.

[252] Q. Wang, L. Tao, X. Jiang, M. Wang, and Y. Shen. Graphene oxide wrapped $CH_3NH_3PbBr_3$ perovskite quantum dots hybrid for photoelectrochemical CO_2 reduction in organic solvents. *Appl. Surf. Sci.*, 465:607–613, 2019.

[253] J. H. Heo and S. H. Im. $CH_3NH_3PbBr_3$–$CH_3NH_3PbI_3$ perovskite–perovskite tandem solar cells with exceeding 2.2 v open circuit voltage. *Adv. Mater.*, 28(25):5121–5125, 2016.

[254] R. Sheng, A. W. Ho-Baillie, S. Huang, M. Keevers, X. Hao, et al. Four-terminal tandem solar cells using $CH_3NH_3PbBr_3$ by spectrum splitting. *J. Phys. Chem. Lett.*, 6(19):3931–3934, 2015.

[255] H. Ji, Z. Shi, X. Sun, Y. Li, S. Li, et al. Vapor-assisted solution approach for high-quality perovskite $CH_3NH_3PbBr_3$ thin films for high-performance green light-emitting diode applications. *ACS Appl. Mater. Interfaces*, 9(49):42893–42904, 2017.

[256] Q. Van Le, H. W. Jang, and S. Y. Kim. Recent advances toward high-efficiency halide perovskite light-emitting diodes: review and perspective. *Small Methods*, 2(10):1700419, 2018.

[257] P. Liu, X. He, J. Ren, Q. Liao, J. Yao, and H. Fu. Organic–inorganic hybrid perovskite nanowire laser arrays. *ACS nano*, 11(6):5766–5773, 2017.

[258] Q. Liao, K. Hu, H. Zhang, X. Wang, J. Yao, and H. Fu. Perovskite microdisk microlasers self-assembled from solution. *Adv. mater.*, 27(22):3405–3410, 2015.

[259] J. H. Heo, D. H. Song, and S. H. Im. Planar $CH_3NH_3PbBr_3$ hybrid solar cells with 10.4% power conversion efficiency, fabricated by controlled crystallization in the spin-coating process. *Adv. Mater.*, 26(48):8179–8183, 2014.

[260] H. Mehdi, A. Mhamdi, R. Hannachi, and A. Bouazizi. $MAPbBr_3$ perovskite solar cells via a two-step deposition process. *RSC advances*, 9(23):12906–12912, 2019.

[261] Y. Ding, J. Chen, H. Chen, et al. Atmosphere dependent gas-solid reaction for high-quality $MAPbBr_3$ perovskite solar cells. *Appl. Surf. Sci.*, 510:145356, 2020.

[262] S. M. Jain, Z. Qiu, L. Häggman, M. Mirmohades, M. B. Johansson, et al. Frustrated lewis pair-mediated recrystallization of $CH_3NH_3PbI_3$ for improved optoelectronic quality and high voltage planar perovskite solar cells. *Energy Environ. Sci.*, 9(12):3770–3782, 2016.

[263] C. Cui, D. Xie, P. Lin, H. Hu, S. Che, et al. Thioacetamide additive assisted crystallization of solution-processed perovskite films for high performance planar heterojunction solar cells. *Sol. Energy Mater. Sol. Cells*, 208:110435, 2020.

[264] C.-J. Yu, Y.-H. Kye, U.-G. Jong, K.-C. Ri, S.-H. Choe, et al. Interface engineering in hybrid iodide $CH_3NH_3PbI_3$ perovskites using lewis base and graphene toward high-performance solar cells. *ACS Appl. Mater. Interfaces*, 12(1):1858–1866, 2019.

[265] J. Qin, J. Zhang, Y. Bai, S. Ma, M. Wang, et al. Enabling self-passivation by attaching small grains on surfaces of large grains toward high-performance perovskite LEDs. *iScience*, 19:378–387, 2019.

[266] Y. Cao, N. Wang, H. Tian, J. Guo, Y. Wei, et al. Perovskite light-emitting diodes based on spontaneously formed submicrometre-scale structures. *Nature*, 562(7726):249–253, 2018.

[267] Z. Liu, F. Cao, M. Wang, M. Wang, and L. Li. Observing defect passivation of the grain boundary with 2-aminoterephthalic acid for efficient and stable perovskite solar cells. *Angew. Chem.*, 132(10):4190–4196, 2020.

[268] Z. Zhou, Z. Wang, Y. Zhou, S. Pang, D. Wang, et al. Methylamine-gas-induced defect-healing behavior of $CH_3NH_3PbI_3$ thin films for perovskite solar cells. *Angew. Chem.*, 127(33):9841–9845, 2015.

[269] Y. Jiang, E. J. Juarez-Perez, Q. Ge, S. Wang, M. R. Leyden, et al. Post-annealing of $MAPbI_3$ perovskite films with methylamine for efficient perovskite solar cells. *Mater. Horiz.*, 3(6):548–555, 2016.

[270] Y. Jiang, L. Tu, H. Li, S. Li, S.-E. Yang, and Y. Chen. A feasible and effective post-treatment method for high-quality $CH_3NH_3PbI_3$ films and high-efficiency perovskite solar cells. *Crystals*, 8(1):44, 2018.

[271] J.-a. Yang, T. Qin, L. Xie, K. Liao, T. Li, and F. Hao. Methylamine-induced defect-healing and cationic substitution: a new method for low-defect perovskite thin films and solar cells. *J. Mater. Chem. C*, 7(35):10724–10742, 2019.

[272] A. Singh, A. S. Chouhan, and S. Avasthi. Effect of methylamine vapor exposure and ambient ageing on $Cs_xMA_{1-x}PbI_{3-x}Br_x$ perovskites for improved carrier collection. *Mater. Res. Express*, 6(8):085519, 2019.

[273] T. Zhang, N. Guo, G. Li, X. Qian, L. Li, and Y. Zhao. A general non-CH_3NH_3X(X= I, Br) one-step deposition of $CH_3NH_3PbX_3$ perovskite for high performance solar cells. *J. Mater. Chem. A*, 4(9):3245–3248, 2016.

[274] Z. Liu, L. Qiu, E. J. Juarez-Perez, Z. Hawash, T. Kim, et al. Gas-solid reaction based over one-micrometer thick stable perovskite films for efficient solar cells and modules. *Nat. commun.*, 9(1):1–11, 2018.

[275] T. Zhang, G. Li, F. Xu, Y. Wang, N. Guo, et al. In situ gas/solid reaction for the formation of luminescent quantum confined $CH_3NH_3PbBr_3$ perovskite planar film. *Chem. Commun.*, 52(74):11080–11083, 2016.

[276] Y.-K. Chih, J.-C. Wang, R.-T. Yang, C.-C. Liu, Y.-C. Chang, et al. NiO_x electrode interlayer and $CH_3NH_2/CH_3NH_3PbBr_3$ interface treatment to markedly advance hybrid perovskite-based light-emitting diodes. *Adv. Mater.*, 28(39):8687–8694, 2016.

[277] A. Singh, F. Matteocci, H. Zhu, D. Rossi, S. Mejaouri, et al. Methylamine gas treatment affords improving semitransparency, efficiency, and stability of $CH_3NH_3PbBr_3$-based perovskite solar cells. *Solar RRL*, 5(9):2100277, 2021. doi:https://doi.org/10.1002/solr.202100277.

[278] K. Xiao, C. Cui, P. Wang, P. Lin, Y. Qiang, et al. Amine treatment induced perovskite nanowire network in perovskite solar cells: Efficient surface passivation and carrier transport. *Nanotechnology*, 29(6):065401, 2018.

[279] Y. H. Lee, J. Luo, M.-K. Son, P. Gao, K. T. Cho, et al. Enhanced charge collection with passivation layers in perovskite solar cells. *Adv. Mater.*, 28(20):3966–3972, 2016.

[280] B. Krogmeier, F. Staub, D. Grabowski, U. Rau, and T. Kirchartz. Quantitative analysis of the transient photoluminescence of $CH_3NH_3PbI_3/PC_{61}BM$ heterojunctions by numerical simulations. *Sustain. Energy Fuels*, 2(5):1027–1034, 2018.

[281] M. V. Khenkin, E. A. Katz, A. Abate, G. Bardizza, J. J. Berry, et al. Consensus statement for stability assessment and reporting for perovskite photovoltaics based on ISOS procedures. *Nat. Energy*, 5(1):35–49, 2020.

[282] C.-G. Wu, C.-H. Chiang, and S. H. Chang. A perovskite cell with a record-high-v_{oc} of 1.61 v based on solvent annealed $CH_3NH_3PbBr_3$/ICBA active layer. *Nanoscale*, 8(7):4077–4085, 2016.

[283] B. O'regan and M. Grätzel. A low-cost, high-efficiency solar cell based on dye-sensitized colloidal TiO_2 films. *Nature*, 353(6346):737, 1991.

[284] A. Hagfeldt, G. Boschloo, L. Sun, L. Kloo, and H. Pettersson. Dye-sensitized solar cells. *Chem. Rev.*, 110(11):6595–6663, 2010.

[285] U. Bach, D. Lupo, P. Comte, J. Moser, F. Weissörtel, et al. Solid-state dye-sensitized mesoporous TiO_2 solar cells with high photon-to-electron conversion efficiencies. *Nature*, 395(6702):583, 1998.

[286] Y. Cao, Y. Liu, S. M. Zakeeruddin, A. Hagfeldt, and M. Grätzel. Direct contact of selective charge extraction layers enables high-efficiency molecular photovoltaics. *Joule*, 2(6):1108 – 1117, 2018.

[287] B. Li, L. Wang, B. Kang, P. Wang, and Y. Qiu. Review of recent progress in solid-state dye-sensitized solar cells. *Sol. Energy Mater. Sol. Cells*, 90(5):549–573, 2006.

[288] J. Gong, K. Sumathy, Q. Qiao, and Z. Zhou. Review on dye-sensitized solar cells (DSSCs): Advanced techniques and research trends. *Renew. Sustain. Energy Rev.*, 68:234–246, 2017.

[289] M. Grätzel. Photoelectrochemical cells. *Nature*, 414(6861):338, 2001.

[290] W. Kubo, K. Murakoshi, T. Kitamura, S. Yoshida, M. Haruki, et al. Quasi-solid-state dye-sensitized TiO_2 solar cells: Effective charge transport in mesoporous space filled with gel electrolytes containing iodide and iodine. *J. Phys. Chem. B*, 105(51):12809–12815, 2001.

[291] O. Bettucci, V. S. Becerril, T. Bandara, M. Furlani, M. Abrahamsson, et al. Organic dye-sensitized solar cells containing alkaline iodide-based gel polymer electrolytes: influence of cation size. *Phys. Chem. Chem. Phys.*, 20(2):1276–1285, 2018.

[292] H. He, J. Zhu, N. Wang, F. Luo, and K. Yang. Composite gel polymer electrolytes containing layered Mg-Al hydrotalcite for quasi-solid dye-sensitized solar cells. *J. Electrochem. Soc.*, 161(1):H17–H20, 2014.

[293] B. Lee, J. He, R. P. Chang, and M. G. Kanatzidis. All-solid-state dye-sensitized solar cells with high efficiency. *Nature*, 485(7399):486, 2012.

[294] Y. Cao, Y. Saygili, A. Ummadisingu, J. Teuscher, J. Luo, et al. 11% efficiency solid-state dye-sensitized solar cells with copper(II/I) hole transport materials. *Nat. Commun.*, 8:15390, 2017.

[295] Y. Saygili, M. Söderberg, N. Pellet, F. Giordano, Y. Cao, et al. Copper bipyridyl redox mediators for dye-sensitized solar cells with high photovoltage. *J. Am. Chem. Soc.*, 138(45):15087–15096, 2016.

[296] M. Grundmann, F.-L. Schein, M. Lorenz, T. Böntgen, J. Lenzner, and H. von Wenckstern. Cuprous iodide–a p-type transparent semiconductor: history and novel applications. *Phys. Status Solidi (a)*, 210(9):1671–1703, 2013.

[297] X. Xin, M. He, W. Han, J. Jung, and Z. Lin. Low-cost copper zinc tin sulfide counter electrodes for high-efficiency dye-sensitized solar cells. *Angew. Chem. Int. Ed.*, 50(49):11739–11742, 2011.

[298] D. Xiong, Z. Xu, X. Zeng, W. Zhang, W. Chen, et al. Hydrothermal synthesis of ultrasmall $CuCrO_2$ nanocrystal alternatives to NiO nanoparticles in efficient p-type dye-sensitized solar cells. *J. Mater. Chem.*, 22(47):24760–24768, 2012.

[299] I.-K. Ding, N. Tétreault, J. Brillet, B. E. Hardin, and E. H. Smith. Pore-filling of Spiro-OMeTAD in solid-state dye sensitized solar cells: Quantification, mechanism, and consequences for device performance. *Adv. Funct. Mater.*, 19(15):2431–2436, 2009.

[300] U. B. Cappel, E. A. Gibson, A. Hagfeldt, and G. Boschloo. Dye regeneration by Spiro-MeOTAD in solid state dye-sensitized solar cells studied by photoinduced absorption spectroscopy and spectroelectrochemistry. *J. Phys. Chem. C*, 113(15):6275–6281, 2009.

[301] L. Schmidt-Mende and M. Grätzel. TiO_2 pore-filling and its effect on the efficiency of solid-state dye-sensitized solar cells. *Thin Solid Films*, 500(1-2):296–301, 2006.

[302] B. Mahrov, G. Boschloo, A. Hagfeldt, L. Dloczik, and T. Dittrich. Photovoltage study of charge injection from dye molecules into transparent hole and electron conductors. *Appl. Phys. Lett.*, 84(26):5455–5457, 2004.

[303] S. Tanaka. Performance simulation for dye-sensitized solar cells: Toward high efficiency and solid state. *Jpn. J. Appl. Phys.*, 40(1R):97, 2001.

[304] U. Bach, Y. Tachibana, J.-E. Moser, S. A. Haque, J. R. Durrant, et al. Charge separation in solid-state dye-sensitized heterojunction solar cells. *J. Am. Chem. Soc.*, 121(32):7445–7446, 1999.

[305] S. A. Haque, Y. Tachibana, D. R. Klug, and J. R. Durrant. Charge recombination kinetics in dye-sensitized nanocrystalline titanium dioxide films under externally applied bias. *J. Phys. Chem. B*, 102(10):1745–1749, 1998.

[306] S. A. Haque, T. Park, A. B. Holmes, and J. R. Durrant. Transient optical studies of interfacial energetic disorder at nanostructured dye-sensitised inorganic/organic semiconductor heterojunctions. *ChemPhysChem*, 4(1):89–93, 2003.

[307] B. C. O'Regan and F. Lenzmann. Charge transport and recombination in a nanoscale interpenetrating network of n-type and p-type semiconductors: Transient photocurrent and photovoltage studies of TiO_2/Dye/CuSCN photovoltaic cells. *J. Phys. Chem. B*, 108(14):4342–4350, 2004.

[308] H. J. Snaith and M. Grätzel. Enhanced charge mobility in a molecular hole transporter via addition of redox inactive ionic dopant: Implication to dye-sensitized solar cells. *Appl. Phys. Lett.*, 89(26):262114, 2006.

[309] U. B. Cappel, T. Daeneke, and U. Bach. Oxygen-induced doping of Spiro-MeOTAD in solid-state dye-sensitized solar cells and its impact on device performance. *Nano Lett.*, 12(9):4925–4931, 2012.

[310] D.-Y. Chen, W.-H. Tseng, S.-P. Liang, C.-I. Wu, C.-W. Hsu, et al. Application of F4TCNQ doped Spiro-MeOTAD in high performance solid state dye sensitized solar cells. *Phys. Chem. Chem. Phys.*, 14(33):11689–11694, 2012.

[311] A. J. Frank, N. Kopidakis, and J. van de Lagemaat. Electrons in nanostructured TiO_2 solar cells: Transport, recombination and photovoltaic properties. *Coord. Chem. Rev.*, 248(13-14):1165–1179, 2004.

[312] A. N. El-Shazly, A. E. Shalan, M. M. Rashad, E. A. Abdel-Aal, I. A. Ibrahim, and M. F. El-Shahat. Solid-state dye-sensitized solar cells based on $Zn_{1-x}Sn_xO$ nanocomposite photoanodes. *RSC Adv.*, 8(42):24059–24067, 2018.

[313] S. K. Balasingam, M. Lee, M. G. Kang, and Y. Jun. Improvement of dye-sensitized solar cells toward the broader light harvesting of the solar spectrum. *Chem. Commun.*, 49(15):1471–1487, 2013.

[314] Y. Hua, B. Xu, P. Liu, H. Chen, H. Tian, et al. High conductivity Ag-based metal organic complexes as dopant-free hole-transport materials for perovskite solar cells with high fill factors. *Chem. Sci.*, 7(4):2633–2638, 2016.

[315] L. Xu, L.-L. Deng, J. Cao, X. Wang, W.-Y. Chen, and Z. Jiang. Solution-processed Cu(In, Ga)(S, $Se)_2$ nanocrystal as inorganic hole-transporting material for efficient and stable perovskite solar cells. *Nanoscale Res. Lett.*, 12(1):159, 2017.

[316] P. Chen, J. H. Yum, F. D. Angelis, E. Mosconi, S. Fantacci, et al. High open-circuit voltage solid-state dye-sensitized solar cells with organic dye. *Nano Lett.*, 9(6):2487–2492, 2009.

[317] M. Cossi, V. Barone, R. Cammi, and J. Tomasi. Ab initio study of solvated molecules: a new implementation of the polarizable continuum model. *Chem. Phys. Lett.*, 255(4-6):327–335, 1996.

[318] M. Pastore, E. Mosconi, F. De Angelis, and M. Grätzel. A computational investigation of organic dyes for dye-sensitized solar cells: benchmark, strategies, and open issues. *J. Phys. Chem. C*, 114(15):7205–7212, 2010.

[319] M. J. Frisch, G. W. Trucks, H. B. Schlegel, G. E. Scuseria, M. A. R. J. R. Cheeseman, et al. Gaussian 09. *Gaussian, Inc., Wallingford CT*, 2009.

[320] T. Moehl, H. N. Tsao, K.-L. Wu, H.-C. Hsu, Y. Chi, et al. High open-circuit voltages: Evidence for a sensitizer-induced TiO_2 conduction band shift in Ru(II)-dye sensitized solar cells. *Chem. Mater.*, 25(22):4497–4502, 2013.

A Appendix

Calculation of Average visible transmittance (AVT):

$$AVT = \frac{\int T(\lambda) P(\lambda) S(\lambda) d\lambda}{\int P(\lambda) S(\lambda) d\lambda} \tag{A.1}$$

where T is the transmission, P is the photopic response, and S is the solar spectrum (AM1.5G) at the wavelength.

Tauc relation to calculate bandgap from the absorption coefficient calculation:

$$(\alpha h\nu)^{1/r} = \beta(\alpha h\nu - E_g) \tag{A.2}$$

Where $r = 1/2$ for direct and 2 for indirect band gap transitions. β^{-1} is bandedge parameter. Using Beer-Lambert-Bouguer Law,

$$\alpha = 2.303A/l \tag{A.3}$$

Where A is absorbance measured from UV-vis spectroscopy and l is the film thickness.

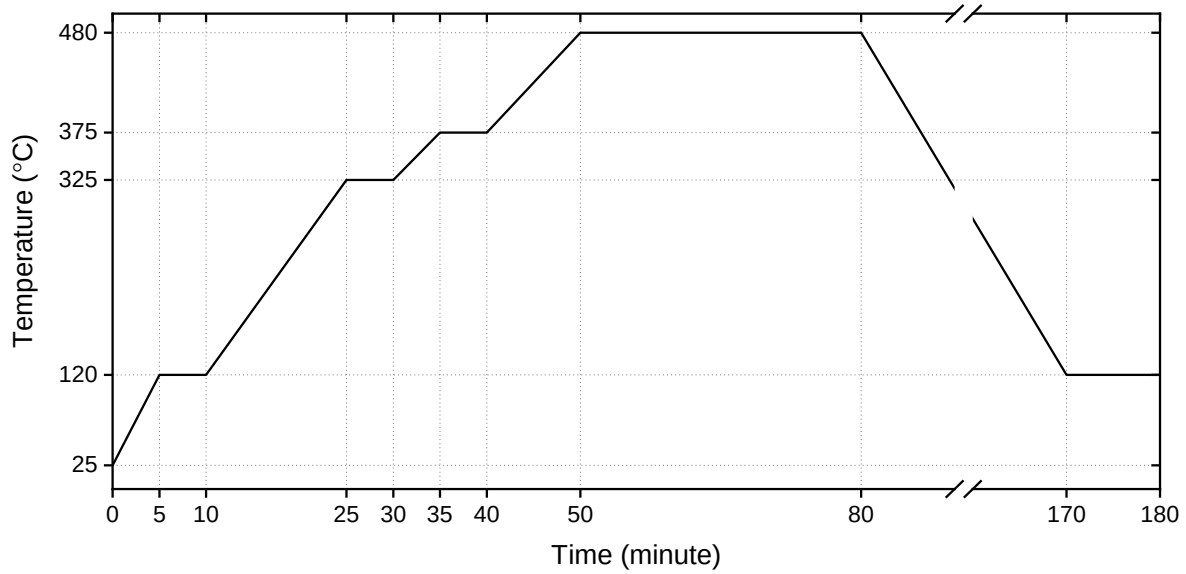

Figure A.1: Temperature ramp function for the post-annealing (sintering) of spin-coated TiO_2 solution to obtain mp$-TiO_2$ scaffold.

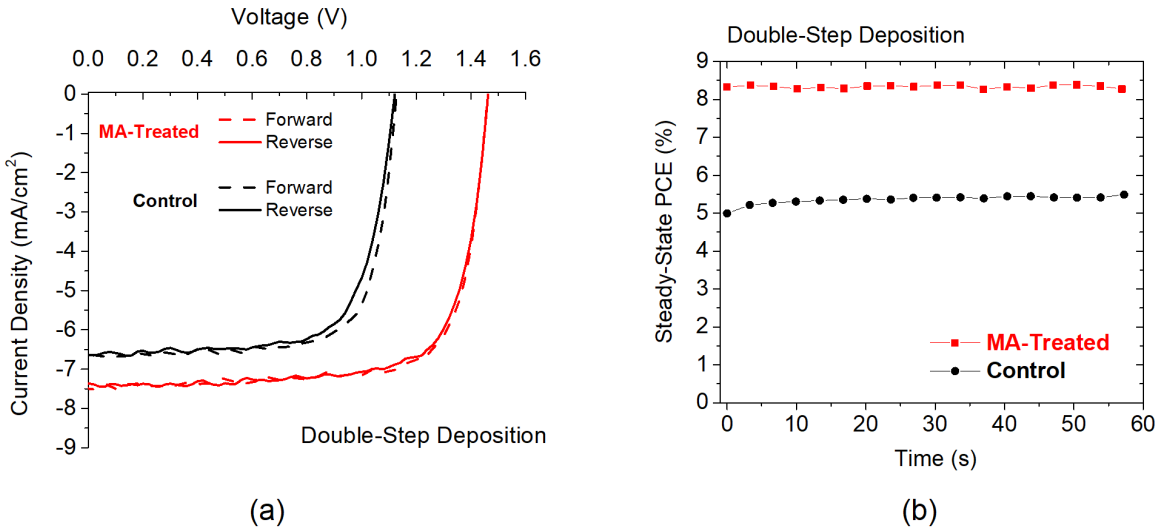

Figure A.2: Measured JV (a) and MPPT (b) for Glass/FTO/c−TiO_2/mp−TiO_2/$MAPbBr_3$/PTAA/gold solar cells obtained by using double-step deposition outside the glovebox. The figure has been reproduced with the permission from ref. [277], © 2021 Wiley-VCH GmbH.

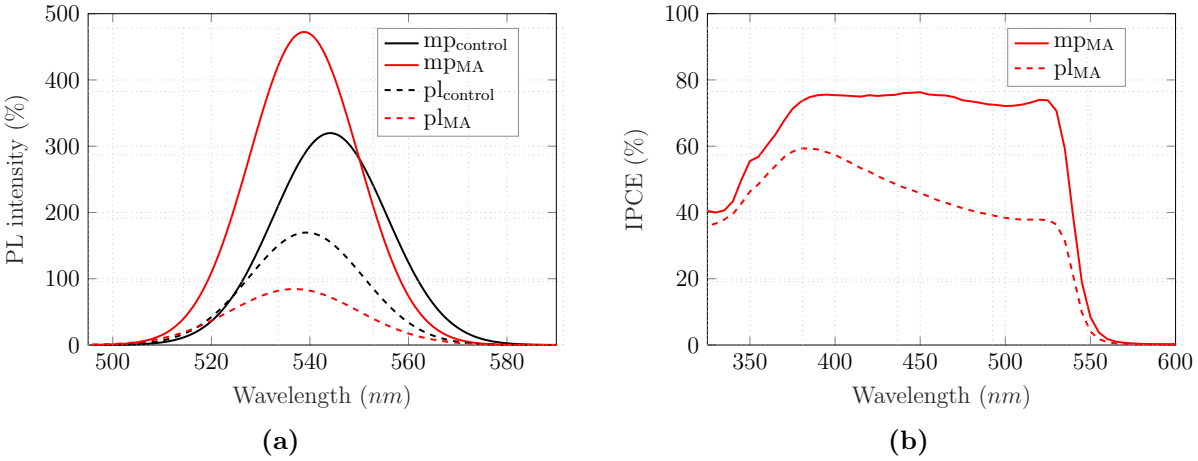

Figure A.3: (a) Steady-state PL measurement for without MA treated (control) and MA treated (MA) $MAPbBr_3$ films on FTO/c−TiO_2/mp−TiO_2 mesoporous (mp) and FTO/c−TiO_2 (pl) stacks. The device stacks are also known as mesoporous (mp), and planar (pl) architectures. (b) Measured IPCE for the mesoporous and planar architecture cells with gold contacts.

B Appendix: Interface electrostatics of solid-State dye-sensitized solar sells: A Joint drift-diffusion and density functional theory study

Note: This appendix's work has been published and reproduced with permission from ref. [100]. Copyright © 2019, American Chemical Society.

B.1 Background

Dye-sensitized solar cells (DSCs) are another organic/inorganic hybrid class of thin-film solar cells that offer low-cost fabrication, flexibility, transparency and high conversion efficiency [283, 284, 285]. The fundamental structure of a DSC consists of a mesoporous semiconducting layer (usually TiO_2) covered by a monolayer of dye molecules. A redox electrolyte contacts with the dye monolayer. Figure B.1a a represent a typical DSC structure. An iodide/triiodide (I^-/I_3^-) redox electrolyte is used in conventional DSCs for the dye regeneration. The dye monolayer absorbs the sunlight and generates electron-hole pairs. The electron-hole pairs dissociate in free electrons and holes because of low binding energy ($\sim k_BT$). The photogenerated electrons are injected into the mesoporous TiO_2. The redox electrolyte then regenerates the dye. Electrolyte based DSCs have shown up to 13% power conversion efficiency [286].

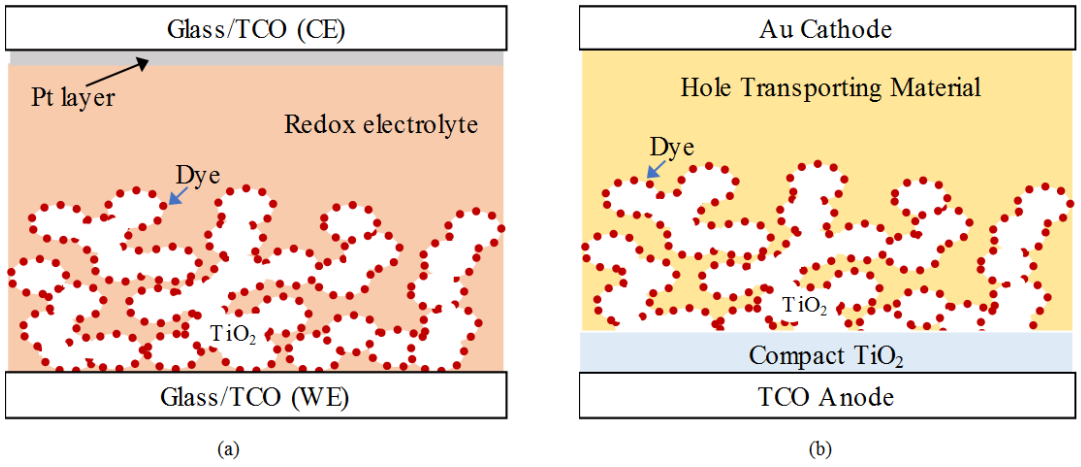

Figure B.1: Schematic representation of a conventional dye-sensitized solar cell (a), and a solid-state dye-sensitized solar cell (b). Reproduced with permission from ref. [100]. Copyright © 2019, American Chemical Society.

Liquid electrolyte based DSCs show good power conversion efficiency even during poor sunlight, but they endure low stability, electrolyte leakage and possibly electrode corrosion [287, 288]. To solve these problems, researchers have tried to replace the liquid electrolyte with solid-state hole conductors [289, 288], quasi solid-state [290], polymer electrolyte [291, 292], wide gap p-type semiconductors and with perovskite semiconductors [293, 35]. In a solid-state dye solar cell, the electrolyte is replaced with a solid hole transporting material as shown in Figure B.1b. Solid-state DSCs are mechanically and chemically stable and offer easy film formation and a high degree of freedom in terms of molecular design [289, 287, 288]. Current state of art solid-state DSCs employ copper complexes as hole transport layer (HTL). Copper complexes offer more positive and tunaable oxidation potential coupled to rapid hole transport in solid $Cu^{(II/I)}$ state [294]. Copper complexes such as $Cu^{(II/I)}$(6,6'-dimethyl-2,2'-bipyridine)$_2$TFSI$_{2/1}$, $Cu^{(II/I)}$(4,4',6,6'- tetramethyl-2,2'-bipyridine)$_2$TFSI$_{2/1}$ [295], [Cu(4,4',6,6'- tetramethyl-2,2'-bipyridine)$_2$](TFSI)$_2$, [Cu(4,4',6,6'- tetramethyl-2,2'-bipyridine)$_2$](TFSI) [294], CuI [296], CuSCN, CZTS (copper zinc tin sulfide) [297] and $CuCrO_2$ [298] are some of the copper complexes employed in solid-state DSCs. Cu(II) complex based solid-state DSCs have shown up to 11% of PCE [294]. Spiro-OMeTAD (2,2',7,7'-tetrakis-(N,N-dipmethoxyphenylamine)9,9'-spirobifluorene) is another attractive solid-state HTL material mainly because of its pore-filling capability in mesoporous TiO_2 [293, 299, 300, 301]. But, Cu(II) complex outperform Spiro-OMeTAD as HTL in solid-state DSCs mainly in terms of output efficiency. This chapter investigates the reasons for under-performing of Spiro-OMeTAD based solid-state DSCs.

In a DSC, the functional element (the dye) responsible for the charge carrier generatio is a separate material from the charge transport layers. The use of additional charge transport material (electrolyte/HTL and TiO_2) leads to additional interfaces within the system. Hence, the charge transfer reaction at the TiO_2/dye/HTL(or electrolyte) interface becomes a key factor in determining the PCE of a cell. In liquid electrolyte based DSCs, photoexcited dye injects electrons into the TiO_2. The electrons are then collected by an external circuit, and the dye regeneration is done by the electrolyte. When an electrolyte is replaced with a solid-state HTL material, wetting and pore filling of HTL into mesoporous TiO_2 becomes crucial [301, 299]. Charge transport from the dye into the HTL experiences a different energetic landscape. Mahrov *et al.* reported that the dye molecules retain the negative charge and inject the positive charge into the hole conductor [302]. Tanaka *et al.* [303] found that the detachment of the HTL from TiO_2 decrease shunt resistance, and limits the PCE of of the cell. Therefore, this is very important to investigate in detail the electrostatics and charge dynamics at the TiO_2/dye/HTL interfaces.

Several studies have suggested that the dye regeneration by solid-state organic HTL takes place on the picosecond time scale [304, 302, 305], and the process is an order of magnitude faster than in the case of liquid electrolytes. Haque *et al.* [306] reported that the hole transfer from the dye into an organic p-type semiconductor is controlled by the thermodynamics (and not by the kinetics) of the TiO_2/dye/HTL interface. They reported a free energy ($\Delta G_{(\text{dye-HTM})}$ E_m(HTM*/HTM)-E_m(Dye*/Dye)) associated to regeneration of the oxidized dye, which is determined by the electrostatic of the interface. Here, HTM stands for hole transport material (same as HTL). Furthermore, they observed that a higher value of $\Delta G_{(\text{dye-HTM})}$ corresponds to a higher hole-transfer yield. O Regan *et al.* [307] studied the the charge carrier recombination processes in solid-state

TiO_2/Dye/CuSCN solar cell. They found that, as compared to (I^-/I_3) electrolyte based DSCs, the recombination in their cell was 100 times faster in short-circuit condition, and 10 times faster in open circuit condition. The faster recombination results in a poor charge collection and hence a low PCE. From the aforementioned studies, this can be inferred that the TiO_2/dye/HTL interface electrostatics determines the hole injection, interfacial recombination, and overall performance of a solid-state DSC. However, a better understanding of the interface electrostatics' role on the hole injection is needed to draw a clear picture of the charge transfer.

Similar to a perovskite solar cell, doping of HTL of solid-state DSCs affects the cell performance [308, 309, 310]. In an organic HTL, the doping can change the charge carrier mobility along with the Fermi-level shift [246]. The Change in the Fermi-level change affects the interface energetics and interface electrostatics, and consequently the charge carrier injection from the dye into the HTL.

Several processes affecting the charge injection, especially at the dye/TiO_2, dye/HTL and TiO_2/dye/HTL interfaces, are not very well understood. Drift-diffusion (DD) is a widely accepted model to describe the charge transport in solar cells and other semiconductor devices. Work in this appendix presents a three-dimensional (3D) drift-diffusion model to study interface electrostatics of a solid-state DSC based on Spiro-OMeTAD HTL. The model accounts for the effect of doping, trap state, charge carrier transport, and generation/recombination process. The DD model calculates electric field components at the TiO_2/Spiro-OMeTAD interface for various trap densities in TiO_2. Furthermore, the role of HTL doping is studied. Thereafter, Density Functional Theory (DFT) calculations are adopted to study the interface electric field's effect on the dye monolayer. Photochemical and photophysical properties of the dye are studied in detail under different interface electrostatics conditions. Ultimately the study investigates the impact of the traps, doping, and the interface electrostatics on the charge injection in sold-state DSCs.

B.2 Simulation method

A finite element 3-dimensional drift-diffusion (DD) model is implemented within TiberCAD. A simulation box with mesoporous TiO_2 interfacing Spiro-OMeTAD hole transport layer is considered. Figure B.2b represents the simulation box, and Figure B.2a shows the corresponding band diagram. The DSCs belong to the thin-film solar cell family with a cell thickness of $\sim \mu$m. Here, a much smaller box of mesoporous TiO_2 and HTL is considered, because the main objective is to study the surface phenomenon, not the output efficiency and bulk phenomena. This is assumed that the repetition of this block represents a full device. The block (Figure B.2b) properly includes photogeneration, charge transport, and surface phenomenon. The model solves 3-dimensional drift-diffusion and Poisson equations simultaneously for charge carriers and traps.

Initially, the effect of dye monolayer is ignored assuming that the electrostatics is dominated by the charge transport layers, and the charge and trap densities at the interface. The thin dye layer is treated just as a source of photogenerated electron-holes after absorbing the sunlight. The the DD model is solved considering TiO_2/HTL interface only. Later, the effect the dye layer is calculated by using DFT calculations. Photogenerated electrons (holes) in the dye are transferred to TiO_2 (Spiro-OMeTAD). The charge trans-

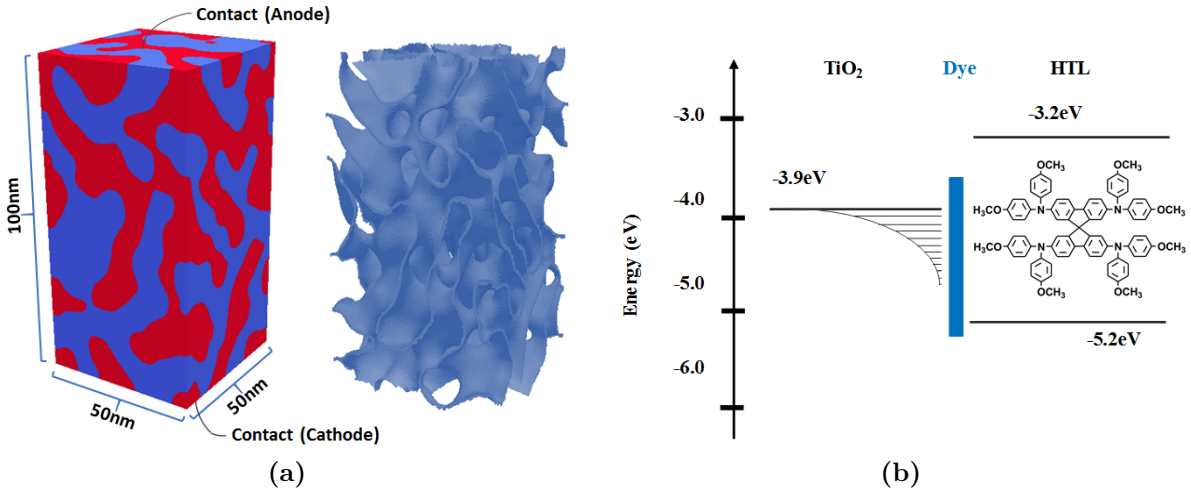

Figure B.2: (a) The drift-diffusion simulation block (left) and the extracted interface (right). (b) Energy band diagram at the HTL(Spiro-OMeTAD)/TiO_2 interface. TiO_2 conduction band has exponential tail for the electron traps. The dye is treated as a source of electron-hole pairs. Reproduced with permission from ref. [100]. Copyright © 2019, American Chemical Society.

port is governed by equation 2.1. The only difference is that, in this study, the set of equations is solved for a three dimensionsal domain. Following the experimental study by Frank *et al.* [311], electron trap states are defined below the conduction band edge of TiO_2, given by:

$$n_t^- = N_t e^{-\alpha(q\Phi_n - E_{CB})/kT} \tag{B.1}$$

where n_t- represents the trapped electron density. N_t and E_{CB} represent the effective density of localized states, and the TiO_2 conduction band, respectively. α defines the depth of the exponential trap tail, and considered to be 0.31 [311] (see Figure B.2a). No hole traps are considered in this study. Direct recombination at the TiO_2/HTL interface is governed by equation 2.3. The drift-diffusion parameters used in the simulations are summarized in table B.1.

As a result, the simulation gives the electron and hole densities, hole and electron current, and the electric field components at the interface. The effect of the trap states and the HTL doping is explained in the next section.

B.3 Results and discussions

Orthogonal electric field component ($E_\perp$) and charge carrier density are calculated at the TiO_2/HTL interface, in short-circuit condition. FigureB.3a represents the ($E_\perp$) distribution at the TiO_2/HTL interface towards the HTL side. At a given electron trap density, 255 bins are chosen to represent the ($E_\perp$) histogram.

The histogram shows that almost 50% of the points on the HTL surface have $E_\perp \simeq 1 \times 10^5\,\mathrm{V\,cm^{-1}}$ for an electron trap (interface) density of $1 \times 10^{12}\,\mathrm{cm^{-2}}$. The $E_\perp$ value increases to $2.5 \times 10^6\,\mathrm{V\,cm^{-1}}$, and $1.25 \times 10^7\,\mathrm{V\,cm^{-1}}$ for the trap densities $1 \times 10^{14}\,\mathrm{cm^{-2}}$, and $1 \times 10^{14}\,\mathrm{cm^{-2}}$, respectively. Also, the absolute value $E_\perp$ increases with increasing the interface trap density.

Table B.1: Drift-diffusion simulation parameters. Asterisk * represents approximated values based on the provided references). Reproduced with permission from ref. [100]. Copyright © 2019, American Chemical Society.

Parameter	Value	Units	Ref.
Electron and hole mobility in Spiro-OMeTAD	0.001	$cm^2\,V^{-1}\,s^{-1}$	[152]
Electron and hole mobility in TiO_2	0.5*	$cm^2\,V^{-1}\,s^{-1}$	[148]
Top metal contact fermi level	-4.3	eV	[312]
Bottom metal contact fermi level	-5.1	eV	[313]
Conduction band minimum of TiO_2	-4	eV	[314]
TiO_2 bandgap	3.3	eV	[314]
TiO_2 dielectric constant	85*	—	[149]
Spiro-OMeTAD bandgap	3	eV	[315]
Spiro-OMeTAD HOMO level	-5.2	eV	[315]
Spiro-OMeTAD dielectric constant	3*	—	[151]
Bimoleular recombination rate	1e-17	$cm^{-2}\,s^{-1}$	fit.
Optical generation rate	7e15	$cm^{-2}\,s^{-1}$	fit.

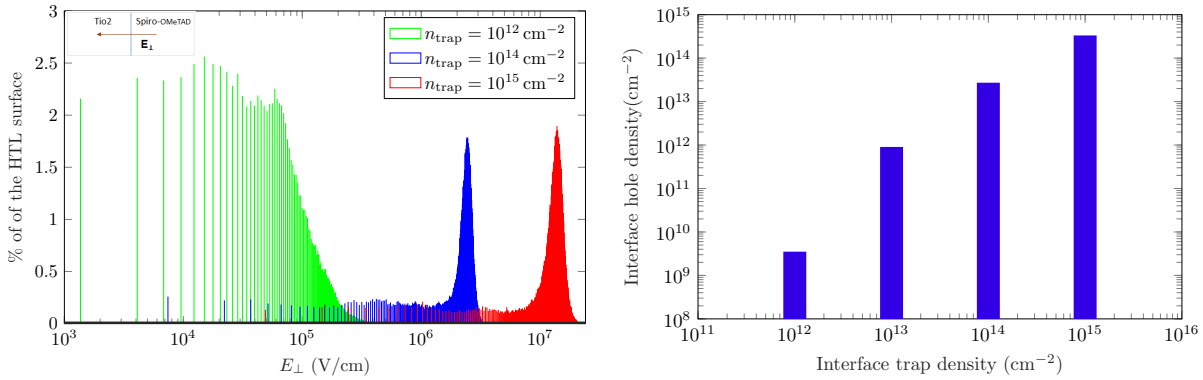

(a) **(b)**

Figure B.3: (a) Orthogonal Electric field ($E_\perp$) distribution at the Spiro-OMeTAD/TiO_2 interface for undoped Spiro-OMeTAD. (b) Hole density at the Spiro-OMeTAD/TiO_2 interface at fixed HTL doping density $1 \times 10^{16}\,cm^{-3}$. Reproduced with permission from ref. [100]. Copyright © 2019, American Chemical Society.

Electrons are trapped by the traps in the bandedge tail of TiO_2 near the TiO_2/HTL interface. The trapping leads to an increased surface electron density. Due to electrostatic attraction, the trapped electrons attract holes from the HTL surface. This results in the accumulation of holes at interface, on the HTL side. Figure B.3b shows interface hole density (on HTL side) at different electron trap densities (in the TiO_2 trap tails). This is clear that, at the interface, increasing the electron traps in TiO_2 tails results in an increased interface hole density on the HTL side. The log-log plot shows almost a linear relationship between the electron traps and the hole accumulation. The whole process of hole accumulation is explained in Figure B.4.

The dye absorbs the sunlight and generates electron-hole pairs, which dissociate into free electrons and holes. Following the energy alignment, the electrons and holes are transferred to TiO_2 and Spiro-OMeTAD HTL, respectively. The transfer of electrons and holes is represented by step ① in Figure B.4. The electrons travel towards the electron

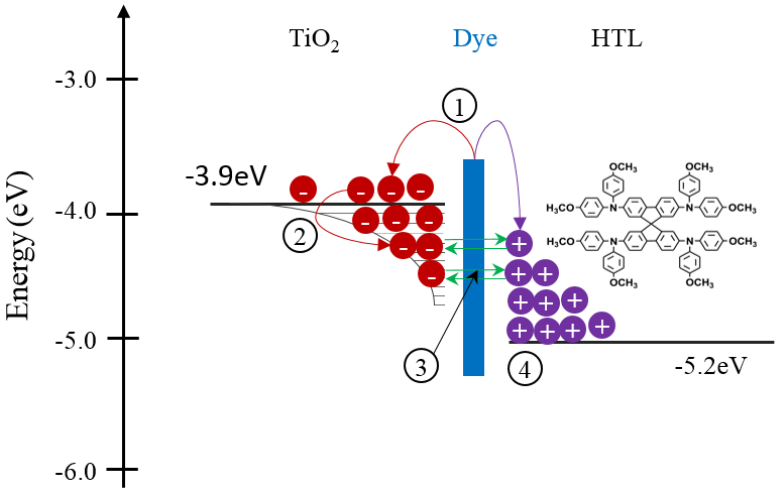

Figure B.4: Interface hole accumulation process: ① Electron-hole separation and transfer to TiO_2 and HTL, ② Trapping of electrons in the TiO_2 at the interface, ③ Coulombic attraction of electrons and holes, and ④ accumulation of holes at the interface on the HTL side. Reproduced with permission from ref. [100]. Copyright © 2019, American Chemical Society.

collecting contact via the bulk TiO_2. Some of the electrons are trapped in the TiO_2 trap tails, as shown by step ②. The Coulombic attraction between electrons and the holes is shown in step ③. This attraction leads to the hole accumulation at the interface on the HTL side, as shown by ④. The trapped electrons and the accumulated holes develop an electric field ($E_\perp$) pointing Spiro-OMeTAD $\rightarrow$ TiO_2.

To investigate the effect of doping, $E_\perp$ is calculated for various doping density in the Spiro-OMeTAD HTL. The electron trap density is fixed at $1 \times 10^{13}\,\mathrm{cm}^{-2}$. The histogram in Figure B.5a shows the distribution of $E_\perp$ at the interface. 250 bins are used to represent the $E_\perp$ for each value of the doping density. It is observed that the $E_\perp$ has a weak dependence on the HTL doping (as compared to traps as shown in Figure B.3a). Here, the amplitude of $E_\perp$ remains in the orders of 10^5 $\mathrm{V\,cm}^{-1}$ for all the doping densities.

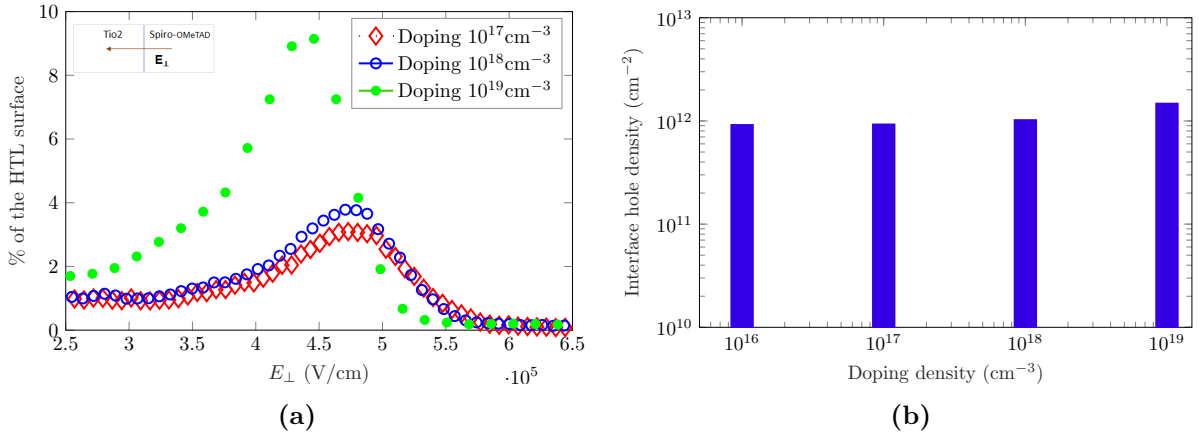

Figure B.5: (a) Orthogonal Electric field ($E_\perp$) distribution at the interface for a fixed interface trap density of $1 \times 10^{13}\,\mathrm{cm}^{-2}$. (b) Surface hole density at the interface at fixed trap density $1 \times 10^{13}\,\mathrm{cm}^{-2}$. Reproduced with permission from ref. [100]. Copyright © 2019, American Chemical Society.

For HTL doping of up to $1 \times 10^{18}\,\mathrm{cm}^{-3}$, because of the electron-screening, the $E_\perp$ distribution remains almost unchanged. For doping density of $1 \times 10^{18}\,\mathrm{cm}^{-3}$, the $E_\perp$ becomes almost twice. This jump in $E_\perp$ can be explained by the distribution of the holes on the HTL side. Figure B.5b shows accumulated hole density at the interface for different HTL doping. For the HTL doping of up to $1 \times 10^{18}\,\mathrm{cm}^{-3}$, the hole density is fixed at $\simeq 1 \times 10^{12}\,\mathrm{cm}^{-2}$. This means that, for a given electron trap density, the $E_\perp$ distribution is governed by number of available holes near the interface. For low doping densities, the hole accumulation is controlled by the photogenerated hole density. For hole doping exceeding the photogenerated hole density (i.e., beyond $10^{18}\mathrm{cm}^{-3}$ in this case), the HTL doping controls the hole accumulation. Therefore, for $1 \times 10^{19}\,\mathrm{cm}^{-3}$ of HTL doping, an increased hole density and consequently increased $E_\perp$ are observed.

Similar to the undoped case, at a given doping of HTL, the $E_\perp$ increases with increasing the interface electron traps, as shown in Figure B.6. The $E_\perp$ maximum value is found to be $1 \times 10^5\,\mathrm{V\,cm}^{-1}$ and $5 \times 10^6\,\mathrm{V\,cm}^{-1}$ for electron trap densities of $1 \times 10^{13}\,\mathrm{cm}^{-2}$ and $1 \times 10^{13}\,\mathrm{cm}^{-2}$, respectively. Furthermore, calculated $E_\perp$ on the TiO_2 side was found to be about two orders of magnitude smaller compared to the HTL side. This could be due the electron screening in TiO_2, because of its high dielectric constant. High dielectric constant of TiO_2 helps maintaining electric displacement field ($\vec{D} = \epsilon \vec{E}$) even with the low electron densities. On the HTL side, low dielectric constant of Spiro-OMeTAD demands holes accumulation at the interface in order to maintain $\vec{D}$.

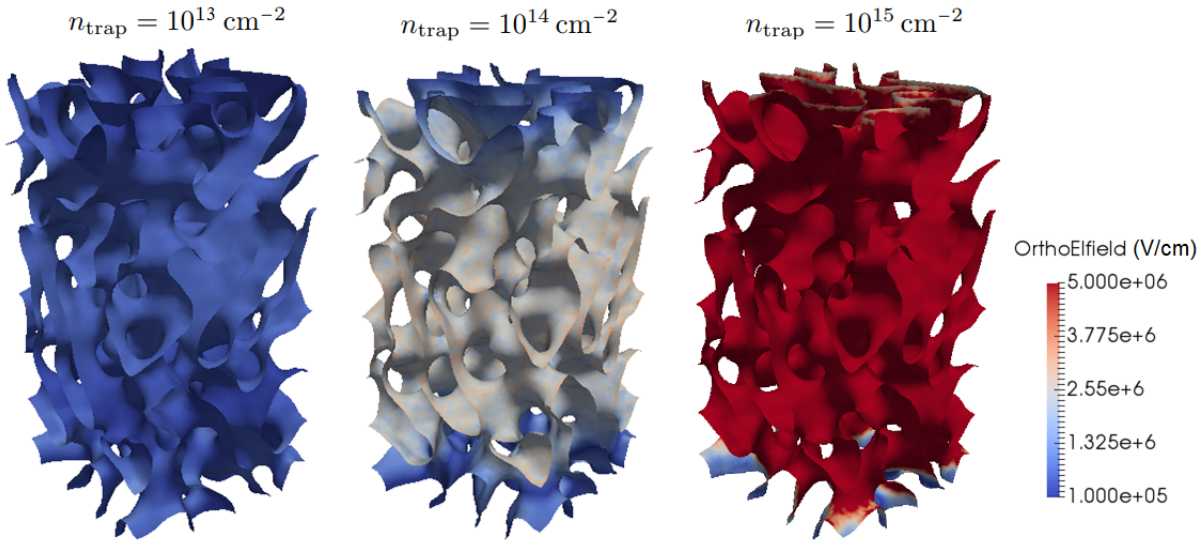

Figure B.6: Orthogonal electric field ($E_\perp$) distribution at the TiO_2/HTL interface (on the HTL side) at a fixed doping density of $1 \times 10^{16}\,\mathrm{cm}^{-3}$. Reproduced with permission from ref. [100]. Copyright © 2019, American Chemical Society.

Atomistic calculations

To study the effect of $E_\perp$ on the dye monolayer, First-principles simulations were done following Chen *et al.* [316], considering a typical organic-dyes (JK2) sensitized on TiO_2 surface. The ground state electronic structure and lowest electronic excitations are calculated by using DFT/TDDFT calculations. The CAM-B3LYP exchange-correlation functional is adopted for the calculations both in vacuo and in acetonitrile solution (a

typically used solvent for DSCs electrolyte). The acetonitrile solution model is described through a polarizable continuum model [317]. The approach ensures a fairly accurate description of charge excitations within the dye, and the charge transfer at the dye/TiO_2 interface [318]. The Gaussian 09 program package is used to carry out the calculations [319].

The effect of $E_\perp$ is calculated on the ground state and excited states of dye/TiO_2 system. Based on the drift-diffusion simulations, the minimum and maximum electric field (orthogonal to the surface) values are taken to be $E_{min} = 2 \times 10^4\,V\,cm^{-1}$ = 4x10^{-6} (a.u) and $E_{max} = 2 \times 10^7\,V\,cm^{-1}$ = 4x10^{-3} (a.u), respectively. The calculation is done for the E_{field} values of 0(no field) and, $\pm$ 10^{-3} a.u. and $\pm$ 10^{-2} a.u., ($\pm$ 5.1 x10^6, $\pm$ 5.1 x10^7 V/cm). Figure B.7 summarizes the ground state electronic structure as a function of the electric field strength. A negative electric field points from the TiO_2 to the dye to surface, and vice-versa.

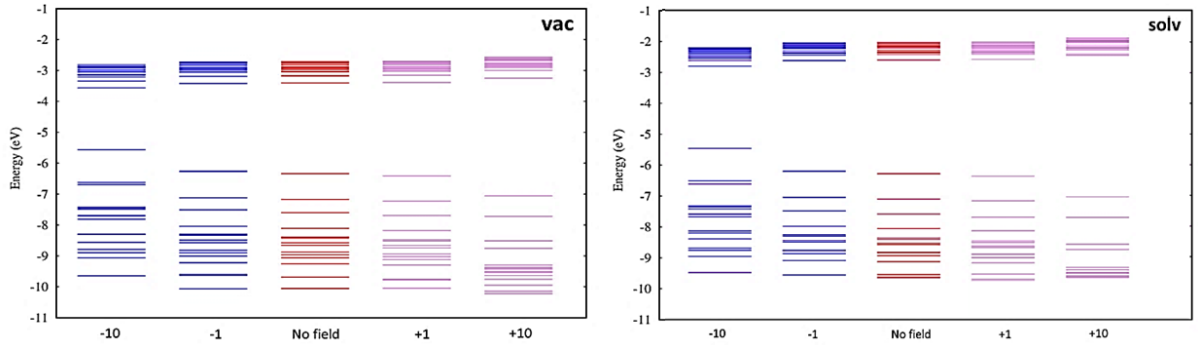

Figure B.7: Molecular orbital diagram of the JK2/TiO_2 system with varying electric field in vacuo (vac) and acetonitrile (solv), see text for definitions. Reproduced with permission from ref. [100]. Copyright © 2019, American Chemical Society.

The JK2@TiO_2 electronic structure represents a typical dye-sensitized interface, with the system's HOMO being localized on the dye. Also, the manifold of TiO_2 unoccupied states represents the set of LUMOs, as shown by the "no field" case in Figure B.8. When the E_{field} value shifts from the negative to positive values, the HOMO density slightly shifts from the dye donor to the dye acceptor group. The dye LUMO lies within the manifold of TiO_2 unoccupied states in the absence of orthogonal electric field.

In an electric field, similar electronic structure variations are observed both in vacuo and in solution. A positive field stabilizes the dye orbitals and destabilizes the TiO_2 orbitals asymmetrically, leading to a dye-TiO_2 gap opening. The negative field exerts an opposite effect. For a positive electric field of 10^{-3} a.u., LUMO is destabilized by 0.04 eV and the HOMO is stabilized by 0.2 eV. The overall behavior is consistent with what previously reported, whereby positive dipolar fields raised the TiO_2 conduction band and led to the observation of higher V_{oc} in DSCs [320]. Due to the asymmetric stabilization/destabilization effect, at high electric field, the LUMO of the combined dye/TiO_2 system becomes the dye LUMO, since TiO_2 states are pushed at higher energies. The stabilization/destabilization processes is represented by an isodensity plot in Figure B.8.

In "non-zero" electric field, the variation in the ground state electronic structure leads to a change in the excited state properties for the JK2@TiO_2 system. Table B.2 summa-

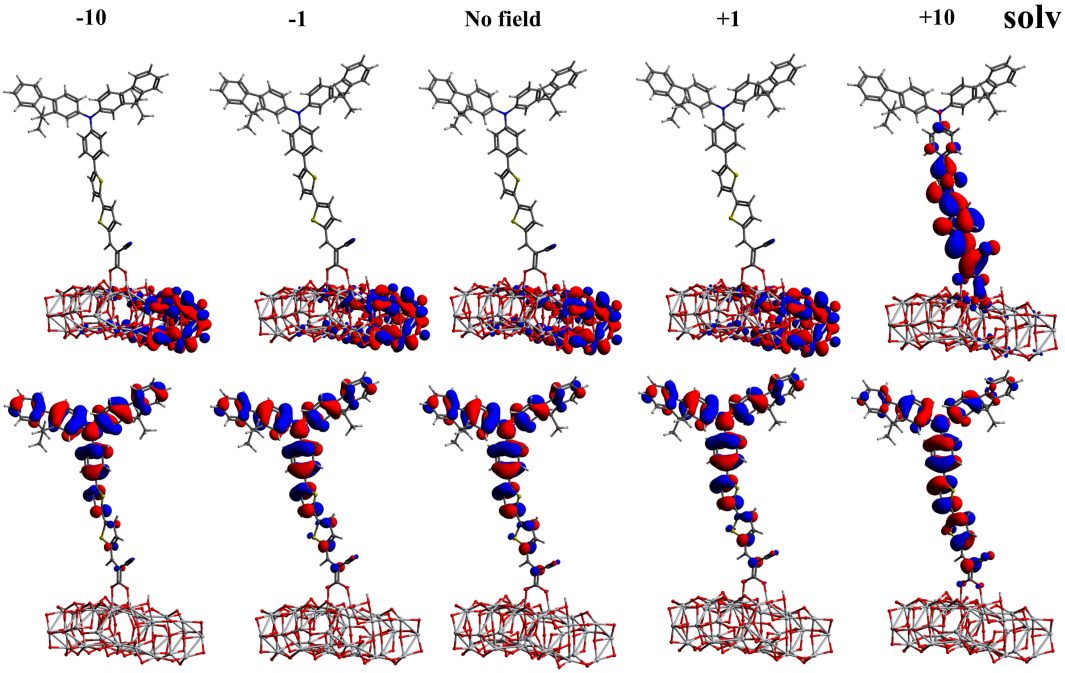

Figure B.8: Isodensity plot of the HOMOs (lower panel) and LUMOs (upper panel) for the JK2/TiO_2 interface in solution as a function of the applied field. Reproduced with permission from ref. [100]. Copyright © 2019, American Chemical Society.

rizes the 5 lowest electronic transitions computed in vacuo. Similar behavior is observed for the JK2@TiO_2 electronic structures calculated in vacuo.

Table B.2: TDDFT calculated lowest 5 excitation energies and oscillator strengths for the JK2/TiO_2 system in vacuo. Reproduced with permission from ref. [100]. Copyright © 2019, American Chemical Society.

-10		-1		No Field		+1		+10	
E	f	E	f	E	f	E	f	E	f
1.587	0.0001	2.398	0.0011	2.485	0.0027	2.570	0.0143	2.745	2.2911
1.806	0.0000	2.582	1.9934	2.602	2.1064	2.620	2.1110	3.287	0.0001
1.914	0.0002	2.631	0.0029	2.718	0.0010	2.804	0.0008	3.458	0.0016
1.948	0.0004	2.670	0.0143	2.750	0.0055	2.830	0.0028	3.480	0.0032
1.994	0.0006	2.747	0.0601	2.822	0.0393	2.895	0.0263	3.522	0.0004

In the absence of electric field, the lowest excitation energy (2.485 eV) corresponds to the direct dye $\rightarrow$ TiO_2 excitation. Due to a small overlap of the dye HOMO and TiO_2 LUMO levels, this transition shows negligible oscillator strength. Moving to positive electric fields, the downshift of dye LUMOs introduces a significant dye character into the lowest transition. At a positive field of 10^{-2} a.u., the TiO_2 excited states reside at higher energy, and the lowest transition shows mainly of dye HOMO $\rightarrow$ dye LUMO character.

For negative electric field values, the energy and the oscillator strength of the lowest excited states decrease upon increasing the electric field. For $E_{field} = -10^{-2}$ a.u., the lowest excitation is dominated by TiO_2 unoccupied states. These states are stabilized compared to dye LUMOs, and the oscillator strength becomes very low. The charge in the energetics

at the dye/TiO_2 interface has important consequences for the operation of a DSC. The positive field exerted by the TiO_2-injected electrons on the positively charged dye alters the interface energetics. This energetics change leads to reduced electron injection from the dye excited state to the unoccupied TiO_2 states.

B.4 Conclusion

This work presents a detailed analysis of the interface electrostatics of a solid-state DSCs. The drift-diffusion simulations show that during the cell operation, a built-in electric field ($E_\perp$) is developed at the TiO_2/Spiro-OMeTAD interface. The $E_\perp$ points from Spiro-OMeTAD toward the TiO_2. This $E_\perp$ is developed by means of the trapped electrons in the conduction bandedge of TiO_2 and the accumulated holes (on the Spiro-OMeTAD side). The hole accumulation and the $E_\perp$ increase steeply with increasing the electron-trap density. However, $E_\perp$ shows a poor dependence on the doping of the HTL. When the HTL doping density exceeds the photogenerated charge carrier density by a factor of 10, the $E_\perp$ increases only by a factor of $\simeq 2$. Furthermore, the First-principle (DFT) analysis suggests that the developed $E_\perp$ (pointing toward TiO_2) destabilizes TiO_2 orbitals, while stabilizes the dye orbitals. This asymmetric stabilization/destabilization leads to a dye/TiO_2 gap opening. This gap increases with increasing $E_\perp$. This change in the energy alignment at the interface leads to lower electron injection from the excited dye into TiO_2. Ultimately, the electron trap-led $E_\perp$ deteriorates the DSCs performance. Reducing electron traps in TiO_2 conduction bandedge and using high mobility HTL materials can help to improve the charge injection and charge transport in solid-state DSCs.

Acknowledgment

First and foremost I would like to thank the almighty God for giving me the opportunity, strength, patience and knowledge to write this thesis.

My unalloyed appreciation goes to my supervisor Prof. Dr. rer. nat. Alessio Gagliardi for giving me the opportunity to work in his research group. I am really thankful for your ideas and, useful discussions throughout my doctoral training. I thank you for all the freedom to express myself, and the motivation to undertake the challenges presented to me over the past few years. I have grown and learned a lot during the past years working under your guidance.

I specially thank the German Academic Exchange Service (Deutscher Akademischer Austauschdienst, DAAD) and International Graduate School of Science and Engineering (IGSSE, TUM) for funding my research. My sincere thanks to all the former and current SNE group members, with special thanks to Waldemar Kaiser, Kashif Hussain, Michael Rinderle and Barbara Asam for their help at various stages.

Further, I want to thank other members of my examining committee, and mentor Prof. Dr.-Ing. Christian Jirauschek. Special thanks to Dr. Fabio Matteocci and Prof. Aldo Di Carlo for providing me an opportunity to work at the Centre for Hybrid and Organic Solar Energy (CHOSE), University of Rome Tor Vergata. Thanks Apoorva Rao, Daimiota Takhellambam and other CHOSE team members for helping me with the experiments. I thank our collaborators Salim Mejaouri and Stefania Cacovich (Institut Photovoltaïque d'lle-de-France (IPVF)), and Frédéric Sauvage (Laboratoire de Réactivité et Chimie des Solides, Université de Picardie Jules Verne, Hub de l'énergie, France). I would also like to thank Prof. Filippo De Angelis' research groups at University of Perugia and CNR-SCITEC Perugia, and Laura Canil and Dr. Antonio Abate from Helmholtz-Zentrum Berlin.

I would like to thank my Guru Prof. G. Vijaya Prakash, for all your support in my academic and personal life. I dedicate this thesis to you. I also thank Sourav Chandra and Samarth Vadia for all their help at countless occasions.

Last but not the least, nothing can outweigh the unconditional support my girlfriend Trinetra Mukherjee and my parents have given to me. Without you, I would have never achieved what I have achieved so far. Thank you for everything.